MASARYKOVA UNIVERZITA
PŘÍRODOVĚDECKÁ FAKULTA
ÚSTAV TEORETICKÉ FYZIKY A ASTROFYZIKY

Diplomová práce

BRNO 2024 MARIANNA DAFČÍKOVÁ

MASARYKOVA
UNIVERZITA
PŘÍRODOVĚDECKÁ FAKULTA
ÚSTAV TEORETICKÉ FYZIKY A ASTROFYZIKY

Hledání a charakterizace astrofyzikálních krátkodobých zdrojů v oboru gama pozorovaných nanodružicemi GRBAlpha a VZLUSAT-2

Diplomová práce

Marianna Dafčíková

Vedoucí práce: RNDr. Jakub Řípa, Ph.D. **Brno 2024**

Bibliografický záznam

Autor:	Marianna Dafčíková Přírodovědecká fakulta, Masarykova univerzita Ústav teoretické fyziky a astrofyziky

Název práce:	Hledání a charakterizace astrofyzikálních krátkodobých zdrojů v oboru gama pozorovaných nanodružicemi GRBAlpha a VZLUSAT-2
Studijní program:	Fyzika
Studijní obor:	Astrofyzika
Vedoucí práce:	RNDr. Jakub Řípa, Ph.D.
Akademický rok:	2023/2024
Počet stran:	x + 98
Klíčová slova:	GRBAlpha; VZLUSAT-2; astrofyzikální transienty; záblesky gama záření; záblesky měkkého gama záření; sluneční erupce; detektory gama záření

Bibliographic Entry

Author:	Marianna Dafčíková Faculty of Science, Masaryk University Department of Theoretical Physics and Astrophysics
Title of Thesis:	Searching and Characterization of Astrophysical Gamma-Ray Transients Observed by GRBAlpha and VZLUSAT-2 CubeSats
Degree Programme:	Physics
Field of Study:	Astrophysics
Supervisor:	RNDr. Jakub Řípa, Ph.D.
Academic Year:	2023/2024
Number of Pages:	x + 98
Keywords:	GRBAlpha; VZLUSAT-2; astrophysical transients; gamma-ray burst; soft gamma repeater; solar flare; gamma-ray detectors

Abstrakt

Představujeme první katalog krátkodobých zdrojů v oboru gama pozorovaných za 3 roky provozu družice GRBAlpha a 2 roky provozu družice VZLUSAT-2. Obě družice jsou technologickou demonstrací nově vyvinutého detektoru gama záření, CsI(Tl) scintilátoru vyčítaného křemíkovými fotonásobiči, který je vhodný pro rutinní pozorování záblesků záření gama (GRB) družicemi typu CubeSat. Průměrná četnost detekcí jedné družice při nepřetržitých měřeních je dva tranzienty za týden, z nichž jeden je GRB. Nejslabší GRB detekovaný jako 5σ detekce patří k nejslabším 15% GRB pozorovaných družicí Fermi/GBM. Z toho vyplývá schopnost detekovat 85% GBM GRB pomocí detektoru na palubě družice, kterou lze držet v jedné ruce. Navíc se zjistilo, že citlivost je vyšší pro tranzienty s tvrdším spektrem, jako jsou krátké GRB, což představuje velkou výhodu při hledání elektromagnetických protějšků gravitačních vln.

Abstract

We present the first catalogue of gamma-ray transients observed in 3 years of GRBAlpha and 2 years of VZLUSAT-2 operations. Both satellites are technological demonstrations of a newly developed gamma-ray detector, a CsI(Tl) scintillator read-out by silicon photomultipliers, convenient for routine observation of gamma-ray bursts (GRB) by CubeSats. Average detection rate of one satellite during non-stop measurements is two transients per week, one of which is a GRB. The faintest GRB detected as a 5σ detection belongs to the faintest 15% of GRBs observed by Fermi/GBM. This implies the ability of detecting 85% of GBM GRBs by a detector on-board a satellite which can be hold in one hand. Moreover, the sensitivity is found to be higher for transients with harder spectra, such as short GRBs, what presents a great advantage in the search for electromagnetic counterparts to gravitational waves.

MUNI
SCI

MASARYKOVA UNIVERZITA
PŘÍRODOVĚDECKÁ FAKULTA
KOTLÁŘSKÁ 2, 611 37 BRNO
IČ: 00216224
DIČ: CZ00216224

ZADÁNÍ
DIPLOMOVÉ PRÁCE

Akademický rok: 2022/2023

Ústav:	Ústav teoretické fyziky a astrofyziky
Studentka:	Bc. Marianna Dafčíková
Program:	Fyzika
Specializace:	Astrofyzika

Ředitel *ústavu* PřF MU Vám ve smyslu Studijního a zkušebního řádu MU určuje diplomovou práci s názvem:

Název práce:	Hledání a charakterizace astrofyzikálních krátkodobých zdrojů v oboru gama pozorovaných nanodružicemi GRBAlpha a VZLUSAT-2
Název práce anglicky:	Searching and Characterization of Astrophysical Gamma-Ray Transients Observed by GRBAlpha and VZLUSAT-2 CubeSat
Jazyk závěrečné práce:	angličtina

Oficiální zadání:
The GRBAlpha nanosatellite (1U CubeSat) is a technological pathfinder to a future constellation of nanosatellites monitoring gamma-ray bursts (GRBs). It was launched in March 2021 and operates on a 550 km altitude sun-synchronous orbit. It carries on board a gamma-ray detector capable of detecting gamma-ray transient events. The detector consists of 75 mm x 75 mm x 5 mm CsI(Tl) scintillator, read out by a dual-channel multi-pixel photon counter (MPPC) setup. The same detector system, but double in size, was launched in January 2022 on VZLUSAT-2 (3U CubeSat) to a similar orbit.
These CubeSats are detecting short and long GRBs originating from mergers of compact objects (neutron stars, black holes) and from collapses of massive starts at the end of their lifetime, respectively. They have also observed activity of the soft-gamma repeater SGR 1935+2154 related to a magnetar (a neutron star with an extremely powerful magnetic field) and detected several solar flares.
The goal of this project is to search for gamma-ray transients detected by these nanostallites characterize them. This includes operations of GRBAlpha satellite, collection of measured data, search for coincident detections by other missions and reporting these detections to the international scientific community via GCN Circulars. For example, the difference in the intensity, duration and spectral hardness of these bursts originating from different sources can be studied. Fluxes detected by GRBAlpha and VZLUSAT-2 can be compared with observations by other missions to characterize the sensitivity of the detectors on board of these CubeSats. Both of the nanosatellites are performing very well and plenty of new measurements and observations of new bursts which can be studied within this project is anticipated.

Vedoucí práce:	RNDr. Jakub Řípa, Ph.D.
Datum zadání práce:	7. 11. 2022
V Brně dne:	31. 5. 2023

Zadání bylo schváleno prostřednictvím IS MU.

Bc. Marianna Dafčíková, 7. 11. 2022
RNDr. Jakub Řípa, Ph.D., 30. 11. 2022
Mgr. Dušan Hemzal, Ph.D., 5. 12. 2022

Acknowledgement

My deepest gratitude belongs to my supervisor Jakub Řípa for his guidance in the past two years and for being patient, especially in the past week. Together with Norbert Werner and Filip Münz, they gave me many, many opportunities to learn from and contribute to ongoing projects, to participate in international meetings, or to see how a new space mission is born. I want to sincerely thank them for all this.

This work would not exist without Andras Pal and his endless efforts to improve the missions. I thank him for sharing his knowledge with me, for constantly upgrading the software for GRBAlpha, and even building a new uplink station by himself.

I cannot forget to mention my fellow GRBAlpha operators, namely Martin, Lea, Miška and Nika. Thank you for being curious and enthusiastic, and for allowing me to take some time off from time to time.

I wouldn't be here without the support of my family and will always be grateful for them. A very special thanks goes to Olívia. Without you I would have never started this journey.

Prohlášení

Prohlašuji, že jsem svoji diplomovou práci vypracoval(-a) samostatně pod vedením vedoucího práce s využitím informačních zdrojů, které jsou v práci citovány.

Brno 6. května 2024 .....

Marianna Dafčíková

Contents

List of acronyms

ADC	analog-to-digital converter
AGILE	Astro-Rivelatore Gamma a Immagini Leggero
AOCS	attitude and orbit control system
BOAT	brightest-of-all-time
CALET	CALorimetric Electron Telescope
CAMELOT	CubeSats Applied for MEasuring and LOcalising Transients
CCDF	complementary cumulative distribution function
CGBM	CALET Gamma-ray Burst Monitor
CME	coronal mass ejection
CPL	cutoff power-law
cps	counts per second
CsI(Tl)	thallium activated cesium-iodide
DAC	digital-to-analog converter
DRM	detector response matrix
FPGA	field-programmable gate array
GBM	Gamma-ray Burst Monitor
GLAST	Gamma-ray Large Area Space Telescope
GNSS	Global Navigation Satellite System
GOES	Geostationary Operational Environmental Satellite
GRB	gamma-ray burst
GW	gravitational wave
ISS	International Space Station
JAXA	Japan Aerospace Exploration Agency
LEO	low Earth orbit
lGRB	long gamma-ray burst
MAXI	Monitor of All-sky X-ray Image
MCU	microcontroller unit
MPPC	Multi-Pixel Photon Counter
OBC	on-board computer

PCB	printed circuit board
PHA	pulse height amplitude
RX	X-ray binary
SAA	South Atlantic Anomaly
SatNOGS	Satellite Networked Open Ground Station
SF	solar flare
SGR	soft gamma repeater
sGRB	short gamma-ray burst
SiPM	silicon photomultiplier
SN	supernova
SNR	signal-to-noise ratio
SS	Sun-synchronous
SSO	Sun-synchronous orbit
UV	ultraviolet
UHF	ultra high frequency
VHF	very high frequency
VZLÚ	Výzkumný a zkušební letecký ústav (Czech Aerospace Research Centre)

Introduction

Discovered by Klebesadel et al. (1973) in the archival data from the military Vela satellites, gamma-ray bursts (GRBs) were for a long time the most mysterious astrophysical events. The very first light curves showed a large variety in their structure and duration which was not typical for astronomical objects. Hundreds of theories were developed in order to explain their origin, however, because no counterparts were found, it was impossible to draw any firm conclusions. It wasn't until 1997 that their extragalactic origin was confirmed thanks to the discovery of the first X-ray (Costa et al., 1997b) and optical (van Paradijs et al., 1997; Sahu et al., 1997) afterglow of the GRB 970228 (Costa et al., 1997a) at z = 0.695 (Bloom et al., 2001). The origin of the short lasting events has been only recently confirmed by the joint detection of a gravitational wave GW 170817 and GRB 170817A (Abbott et al., 2017). Today, many mysteries about these events remain unsolved. Moreover, recent observations of kilonovae accompanying long GRBs (Troja et al., 2022; Levan et al., 2023) indicate that there are still many surprises ahead of us.

Current satellite missions reach their limits and newer technologies need to be implemented in order to provide deeper understanding of the physical properties producing such tremendous amounts of energy as GRBs. For this, it is necessary to observe GRB afterglows as early as possible after the prompt emission. Numerous efforts have been made to provide quick follow-up observations such as the Swift satellite (Gehrels et al., 2004) which is able to slew to the calculated GRB location in just a few minutes. The disadvantage of these missions is that they have limited field of view mainly because large part of the sky is occulted by the Earth.

To achieve better sky coverage, an idea of a constellation of small satellites around the Earth arose. If there is enough of them, this fleet of satellites would enable an all-sky coverage and quick localization of GRBs via the triangulation method (Burgess et al., 2021). Additional advantage of such a constellation is the lower cost and faster development. One of the proposed missions is the CAMELOT constellation (Werner et al., 2018) with a newly developed gamma-ray detector composed of a CsI(Tl) scintillator coupled with silicon photomultipliers (SiPMs). The prototype of this detector is already employed in two space missions, GRBAlpha (Pál et al., 2023) and VZLUSAT-2 (Dániel et al., 2020). In this work, we present the first catalogue of the detected gamma-ray transients and study the sensitivity of the detector.

The thesis is structured as follows. Chapter 1 provides a brief overview of astrophysical gamma-ray transients and their observational properties, focusing on the gamma part of the spectrum. Chapter 2 introduces the GRBAlpha and VZLUSAT-2 space missions. Chapter 3 describes the methods used for the analysis. Finally, the results and presented and discussed in chapter 4.

Chapter 1

Astrophysical gamma-ray transients

1.1 Gamma-ray bursts

1.1.1 Observational properties

Gamma-ray bursts (GRBs) are among the shortest yet most energetic explosions in the universe. In only a few seconds they generate $\sim 10^{51}$ erg (Frail et al., 2001), comparable to a supernova explosion. Majority of the energy is emitted in soft gamma rays with the peak being around 150 keV (e.g. Poolakkil et al. (2021)).

GRB duration is characterized by the quantity named T_{90} duration (Kouveliotou et al., 1993), defined as the time during which the total recorded signal increases from 5% to 95%, hence encompassing 90% of the total observed fluence. The duration as well as the shape of the light curve varies greatly from one event to another. The variability of GRB light curves observed by the GRBAlpha and VZLUSAT-2 nanosatellites can be seen in the Appendix A of this work. The shortest GRBs ever observed have T_{90} durations in order of tens of miliseconds, e.g. GRB 050509B (Barthelmy et al., 2005a) lasting ~ 30 ms. On the other hand, a special population of ultra-long GRBs exists with durations above 10^4 s (Levan, 2015).

The duration distribution of GRBs has been observed to have a bimodal character. The separation into two categories intensifies when taking spectral properties into account; shorter bursts are on average harder compared to the long-duration events (Fig. 1.1). This suggests that it is not an observation bias but the division has a physical origin.

1.1.2 Fireball model

According to the broadly accepted fireball model (Fig. 1.2, Cavallo and Rees (1978); Piran (1999)), the prompt gamma-ray emission is produced by dissipation of kinetic energy of ultra-relativistic matter ejected from a hidden central engine in collisions between faster and slower moving clumps. This internal shock scenario is able to explain the high variability of observed light curves on millisecond scales. The remaining energy is dissipated further away from the source where the matter interacts with the surrounding medium. These external shocks produce long-lasting afterglow emission across all wavelengths.

The central engine of GRBs is invisible to us and it is still unclear what mechanisms are

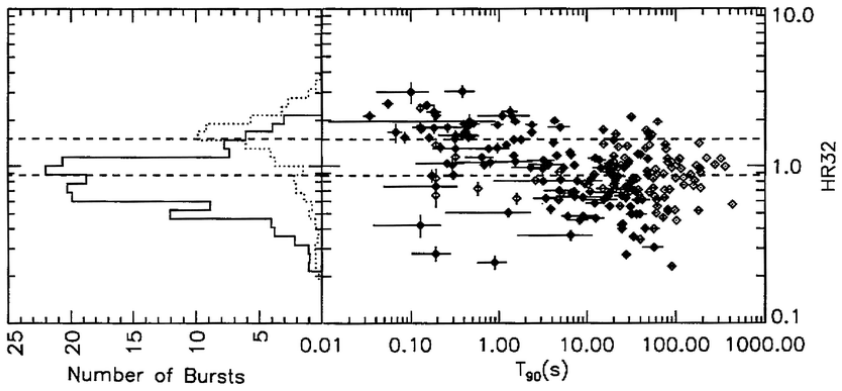

Figure 1.1: The distribution of the T_{90} duration and hardness ratio of GRBs from the first BATSE catalogue (Kouveliotou et al., 1993). The distribution reveals two GRB classes; the shorter and harder bursts, and longer softer events.

responsible for such tremendous energies. A general pattern of many models is a production of relativistically expanding electron-positron pairs by annihilation of neutrinos with antineutrinos. The neutrinos and antineutrinos are thought to be produced in two situations; either during the collapse of a massive stellar core into a black hole, or in mergers of two neutron stars or a neutron star with a black hole (Piran, 2004; Mészáros, 2006). These two models for a GRB progenitor are related to the two observed classes of GRBs apparent in the $T_{90} - HR$ plane (Fig. 1.1). Long GRBs typically occur in star-forming galaxies and many of them have been associated with supernovae (SNe). The first explicit evidence for a long GRB–SN connection was found by Stanek et al. (2003) in case of GRB 030329 and SN 2003dh. The origin of short GRBs was confirmed much more recently. To date, only one short GRB has been unambiguously associated to a binary neutron star merger by joint observation of GRB 170817A and a gravitational wave GW 170817 (Abbott et al., 2017; Goldstein et al., 2017).

However, the two observed classes of GRBs may not be so strictly separated. Recently, two exceptionally bright GRBs, GRB 211211A (Troja et al., 2022; Zhu et al., 2022; Gompertz et al., 2023) and GRB 230307A (Levan et al., 2023; Bulla et al., 2023; Dai et al., 2024), were observed with an associated thermal emission, or kilonova, which comes from the decay of heavy elements produced in compact mergers. These results reveal that some long GRBs can also originate in mergers of compact objects.

The extraordinary energetics of GRBs can be explained by a non-isotropic outflow of matter which is instead concentrated into a jet. This beaming has been confirmed by observations of brakes in the afterglow light curves which occur once the ejected matter slows down enough for the edge of the jet to become visible. Typical jet opening angles are $\sim 5 - 20$ degrees (Mészáros, 2006). More narrow jets have been observed, for instance in case of the brightest-of-all-time GRB 221009A whose extraordinary brightness is thought to be essentially a result of an extremely narrow opening angle (An et al., 2023; Gill and Granot, 2023; Derishev and Piran, 2024; Zhang et al., 2024).

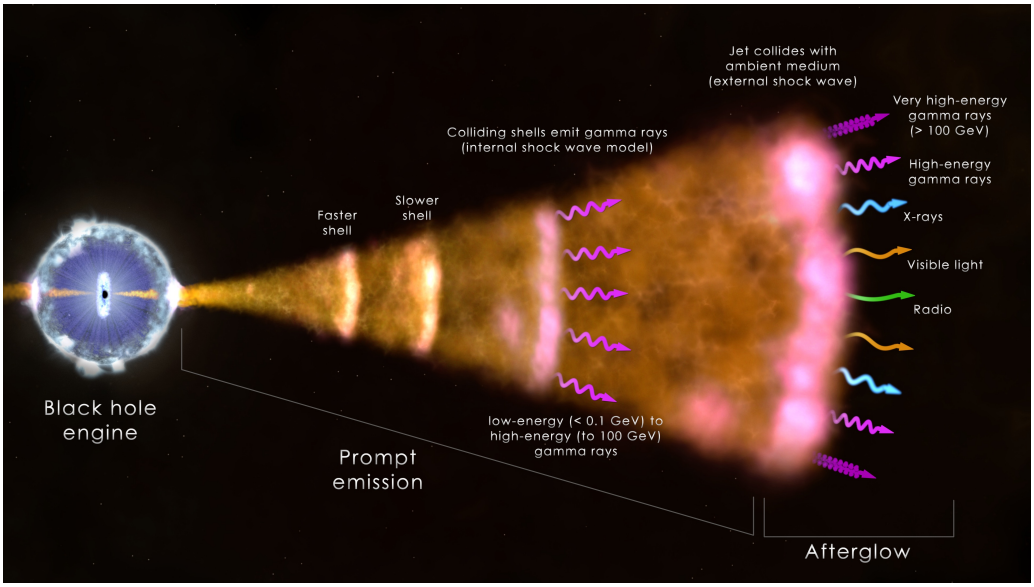

Figure 1.2: An illustration of the fireball model of emission mechanism of gamma-ray bursts. The prompt emission is produced by internal shocks within the jet while the afterglow emission comes from the interaction with the surrounding medium. Credit: NASA.

1.2 Solar flares

Solar flares are the brightest explosions in our solar system. They are initiated by the build-up of magnetic energy due to various plasma instabilities it the solar corona. The stored energy is later released in the process of magnetic reconnection, illustrated in Fig. 1.3, when particles from the solar corona are accelerated in two opposite directions; some escape to the interplanetary medium, the rest falls back and collides with plasma in lower parts of the solar atmosphere. The total amount of released energy reaches 10^{32} erg (Fletcher et al., 2011). Although it is much lower than the energy released in GRBs, solar flares are particularly interesting because of their proximity to the Earth. They can be accompanied by coronal mass ejections, or can accelerate protons in the solar corona to relativistic speeds. If either of the two is directed towards the Earth, they can not only damage satellites in space, but also cause blackouts and damage transformers on the ground Pulkkinen (2007).

From an observational point of view, solar flares typically last between few minutes to several hours. The energy is released across all wavelengths with the peak being at soft X-rays. The classification of these events is thus determined from their peak X-ray flux in the $0.1 - 0.8$ nm band observed by the GOES satellites (Tab. 1.1). Gamma-ray emission from solar flares is regularly detected by missions such as Fermi/GBM[1], Konus/Wind[2] or AGILE (Ursi et al., 2023).

[1] https://heasarc.gsfc.nasa.gov/w3browse/all/fermigsol.html
[2] https://www.ioffe.ru/LEA/Solar/index.html

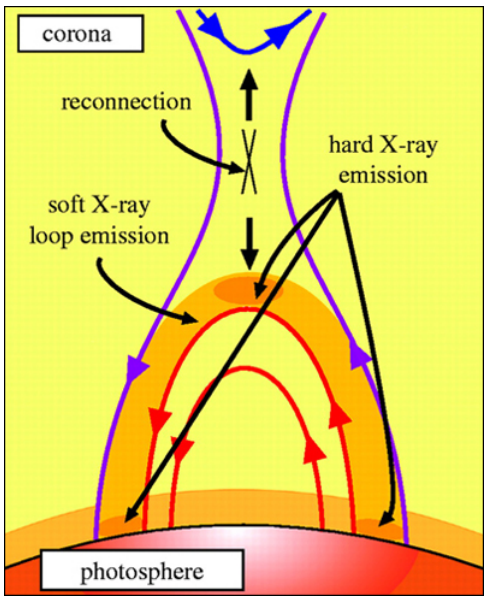

Figure 1.3: An illustration of a magnetic reconnection process in the solar atmosphere. The purple curves are the approaching magnetic field lines shortly before the reconnection. The red curves represent matter falling back to the photosphere while the blue curve illustrates outflow to the interplanetary medium. The emission regions of soft and hard X-rays are marked by black arrows. Adapted from: http://www.solarsystemcentral.com/sun_in_depth_page.html.

Table 1.1: Classification of solar flares based on their peak flux in soft X-rays measured by the GOES satellite.

SF class	GOES X-ray flux [W m^{-2}]
A	$10^{-8} - 10^{-7}$
B	$10^{-7} - 10^{-6}$
C	$10^{-6} - 10^{-5}$
M	$10^{-5} - 10^{-4}$
X	$10^{-4} - 10^{-3}$

1.3 Soft gamma repeaters

Initial observations of soft gamma repeaters were not very different from GRBs. Although they appeared shorter and softer, they were considered to be yet another sub-group of GRBs. First stronger indications that they might form a separate group of transients appeared when repeated detections came from the same locations on the sky. Kouveliotou et al. (1998) found the first evidence that these flares originate in neutron stars with extremely strong magnetic field, named magnetars, by measuring the spindown rate from the persistent X-ray flux of one of the sources. This supported earlier hypothesis that the observed flares in gamma rays are produced by magnetic stresses similar to solar flares but on much larger scales (Mereghetti, 2008).

Typical duration of a SGR is $\sim$ 100 ms. They often produce many such brief pulses in an extended period of a few days and then go silent for months or even years. Compared

to GRBs, the maximum of their emission lies in lower energies, i.e. their spectra are softer (Hurley, 2011). To date, only a handful of SGRs is known. Majority of them comes from our Galaxy. A comprehensive list can be found for instance in The McGill Magnetar Catalog by Olausen and Kaspi (2014).

1.4 X-ray binaries

Binaries which exhibit strong X-ray outbursts (Negueruela, 1998; Reig, 2011) belong to the close binary star systems. Typically, one of the components is still an active star with chemical elements burning in its core while the other one is either a neutron star, black hole, or white dwarf. The X-ray emission comes from mass transfer from the photosphere of the active star to the compact object which consequently forms an accretion disk (Fig. 1.4). The most abundant type of X-ray binaries is the Be/X-ray type which consists of a Be star, a star of the spectral type B with prominent emission lines, and a neutron star. Compared to other types of astrophysical gamma-ray transient, outbursts from X-ray binaries appear more sporadically.

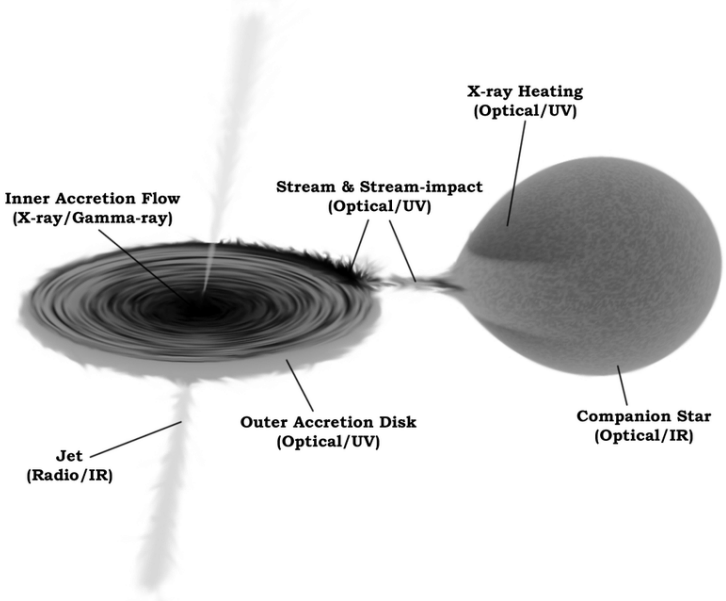

Figure 1.4: An illustration of an accretion in an X-ray binary. Adapted from Hynes (2010).

Chapter 2

GRBAlpha & VZLUSAT-2

GRBAlpha (Pál et al. (2023), Fig. 2.1, 2.3), a 1U CubeSat, is a technological experiment with the aim to test the concept and study the degradation of a newly developed gamma-ray detector for future CAMELOT mission (Werner et al., 2018). It was launched on 22 March 2021 to a Sun-synchronous orbit (SSO) with an inclination of 97.5 degrees and altitude of approximately 550 km. One of the mission objectives is to monitor the background at SS low Earth orbit (LEO) in order to place constraints on the duty cycle for future satellite constellations at SS LEO.

VZLUSAT-2 (Fig. 2.2) is a Czech 3U CubeSat launched on 13 January 2022 to an SSO with an inclination identical to that of GRBAlpha, and slightly lower altitude of about 535 km. Its primary instrument is a camera dedicated to Earth observations. Two of the gamma-ray detectors developed for CAMELOT are among the secondary payload.

2.1 Detector

Primary components of the detector (Ohno et al., 2018; Pál et al., 2020, 2023) are a CsI(Tl) scintillator with eight silicon photomultipliers (SiPMs) glued to its side. The crystal has a size of $75 \times 75 \times 5$ mm. It is wrapped in a reflective foil to prevent the escape of scintillation optical photons, and the whole configuration is further put in a black tedlar and an aluminium case to prevent the entry of visible light from outside. Moreover, the side with SiPMs is also covered by a lead alloy to decrease radiation damage. The SiPMs, also named multi-pixel photon counters (MPPCs), are arrays of thousands of avalanche photodiodes connected in parallel. They are separated into two channels of four, each with its own analogue and digital electronics.

When a high-energy photon or charged particle interacts with the crystal atoms, it forces an electron to jump from the valence band to the conduction band. As the electron moves through the crystal, it loses its energy by exciting thallium atoms. These decay after characteristic times of 0.68 and 3.3 μs while emitting light with a maximum at ~ 560 nm (Valentine et al., 1993; Knoll, 2000). The optical photons are then detected by individual photodiodes which consequently become conductive. The total measured charge in four MPPCs is integrated during 15 μs with a sampling time of 1.5 μs, and converted to voltage by a preamplifier. Finally, a shaping amplifier is used to reduce instrumental noise in order to determine the pulse height amplitude (PHA) more precisely. The measured signal is

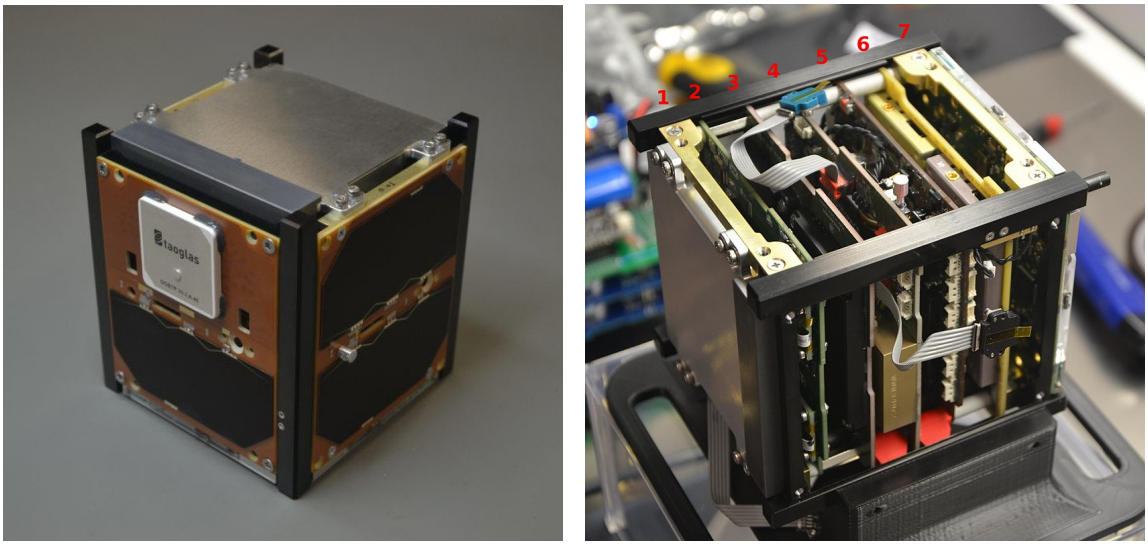

Figure 2.1: External (*left*) and internal (*right*) view of the GRBAlpha CubeSat (Pál et al., 2020). 1 – the gamma-ray detector; 2 – PCB with payload electronics; 3 – OBC and GNSS board; 4 – attitude sensors, sun-sensors and X-ray dosimeter; 5 – power supply; 6 – UHF and VHF radio transceivers; 7 – antenna deployer.

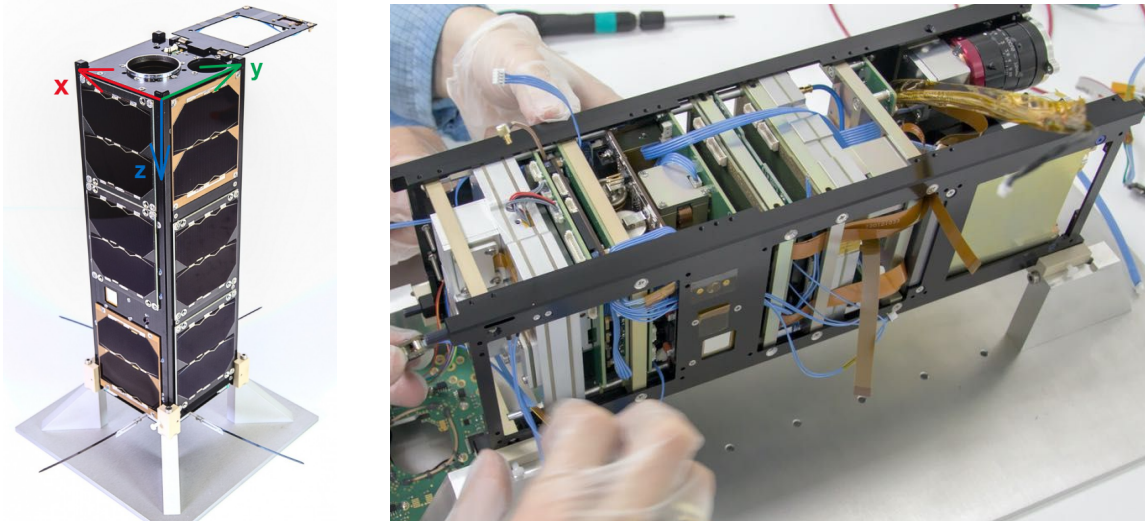

Figure 2.2: External (*left*) and internal (*right*) view of the VZLUSAT-2 CubeSat. GRB unit 0 is located at +x; unit 1 at -y. The detectors are located next to the camera with the MPPCs oriented inwards. Thanks to this detector orientation and larger scale of VZLUSAT-2, the MPPCs are more shielded and degrade slower compared to GRBAlpha. Credit: VZLÚ.

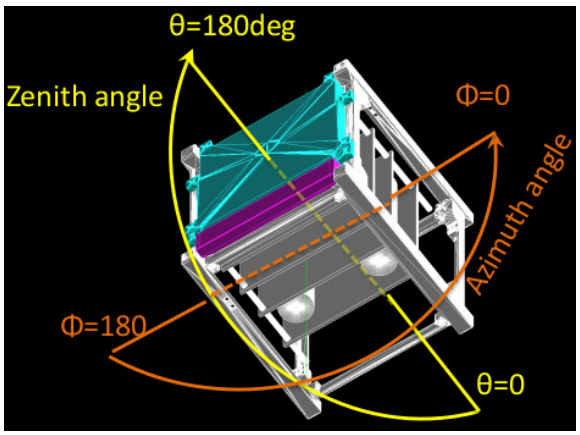

Figure 2.3: Mass model of GRBAlpha. The detector location is show in cyan color with the lead-alloy shielding of MPPCs highlighted in magenta.

proportional to the energy of incident gamma-rays or charged particles and the exact value of the deposited energy is determined from the PHA by an 8-bit ADC.

The digital part of the payload electronics consists of a field-programmable gate array (FPGA) and a microcontroller unit (MCU). The FPGA is directly connected to the ADC and saves the signal measured during the pulse processing time $\tau = 15$ μs as one count with an energy determined by the ADC. The stored data can be transmitted to a ground station either directly from the MCU or via the main on-board computer (OBC).

If the incoming flux is low, each detected incident particle is recorded as one count with an energy proportional to the number of scintillation photons. However, if the incoming flux is too high, the signal received during the pulse processing time is recorded as one count, no matter how many high-energy particles contributed to it. Moreover, the higher number of incident particles at one time increases the number of scintillation photons and thus also the probability that a photodiode will be hit by more than one optical photon. Consequently, the measured count rate is lower and the recorded energy higher. This is called pulse pile-up. For GRBAlpha, it starts at approximately 2500 cnt/s (Řípa et al., 2023) and is therefore usually negligible. However, in exceptional cases, such as the detection of the brightest-of-all-time GRB 221009A, it had to be taken into account.

2.1.1 Energy conversion

As stated in the previous section, the energy of the detected particles is measured by the PHA. In order to draw any meaningful conclusions from the acquired data, we need to know the relation between the PHA, i.e. ADC channel, and the energy in physical units. For this, a series of calibration measurements was done before the launch of GRBAlpha in laboratories of the Technical University of Košice, Slovakia. Total of seven spectral lines were used for the calibration, specifically the 31 keV and 81 keV lines of ^{133}Ba, 22 keV and 88 keV lines of ^{109}Cd, 25 keV and 59.5 keV lines of ^{241}Am, and the 511 keV line of ^{22}Na (Ohno, 2022).

The conversion relation is linear and follows

$$\text{E [keV]} = \text{gain factor} \times \text{ADC channel no.} - \text{offset}. \tag{2.1}$$

In the pre-flight calibrations, the gain factor and offset values for channel 0 were measured to be 4.08 keV/ch and 154.0 keV, respectively. Due to the degradation of MPPCs, the gain decreases with time. As a result, the recorded PHA of a specific input energy is lower and thus the gain factor needs to be modified to correspond to the true value in keV. The revision was done with two activation lines which are visible in the spectra after a passage through the South Atlantic Anomaly (SAA). Its current value is 4.31 keV/ch and is used since August 2022. As described in the next section, the MPPCs on-board VZLUSAT-2 degrade slower and therefore in the analysis of VZLUSAT-2 data we still use the original values.

2.1.2 Comparison of readout channels

Although measurements are usually done only by the readout channel 0, in order to increase our temporal resolution we have tried doubling the memory space by alternating between the two channels. These tests revealed differences in count rates measured by the two channels. Fig. 2.4 shows that the count rate observed by channel 1 is systematically higher than that observed by channel 0. This is likely due to the fact that different energy conversion relation applies to each channel and so the individual energy bands correspond to slightly different energies for each channel. However, because of a poor energy resolution of the detector ($\sim 30\%$, Torigoe et al. (2019)) we use the same relation for both channels.

Another difference between the two readout channels is in the observed spectrum (Fig. 2.5). The initial peak, which corresponds to the instrumental noise, is observed to be wider in data from channel 1. Due to this, the low energy cutoff used for regular observations by channel 1 is larger. The difference in the cutoff value is approximately 10 keV.

We note that for the detectors on-board VZLUSAT-2 the noise peak is narrower and the cutoff lower by approximately 40 keV. Consequently, VZLUSAT-2 is more sensitive for transients with softer spectra. This is related to the degradation of MPPCs which is slower for VZLUSAT-2 detectors for numerous reasons. It was launched one year after GRBAlpha when the Sun was closer to its maximum and thus the flux of trapped protons at LEO lower; the altitude of VZLUSAT-2 is slightly lower and therefore it is exposed to lower fluxes of geomagnetically trapped protons inside SAA; the detectors on-board VZLUSAT-2 are more shielded and the temperature of their MPPCs is a bit lower. The effect of each contributor is at the moment being investigated.

2.1.3 Detector response matrix

The energy recorded by the detector is not the true energy of an incident particle but only the amount which was deposited in the scintillator. Gamma-ray photons and high-energy charged particles can interact with the crystal via various processes (Knoll, 2000). As a result, the particle is either fully absorbed, it passes through the crystal without any energy loss, or loses only part of its energy which is detected by our instrument.

A photon with energy higher than the binding energy of the material can transfer its entire energy to an electron in an atom via a photoelectric effect. If the electron was

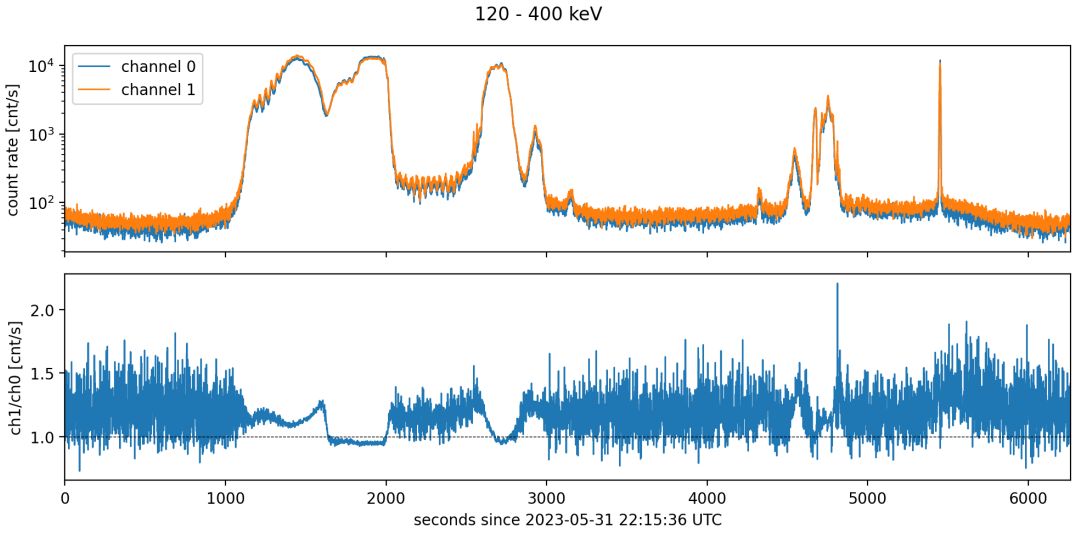

Figure 2.4: Comparison of the detected background count rate from the two readout channels on GRBAlpha. Channel 1 measures systematically higher values. This behaviour is not fully understood but is likely related to the dark current or different gain calibration for each channel. Only data in one energy band is shown but this behaviour is observed in all energies.

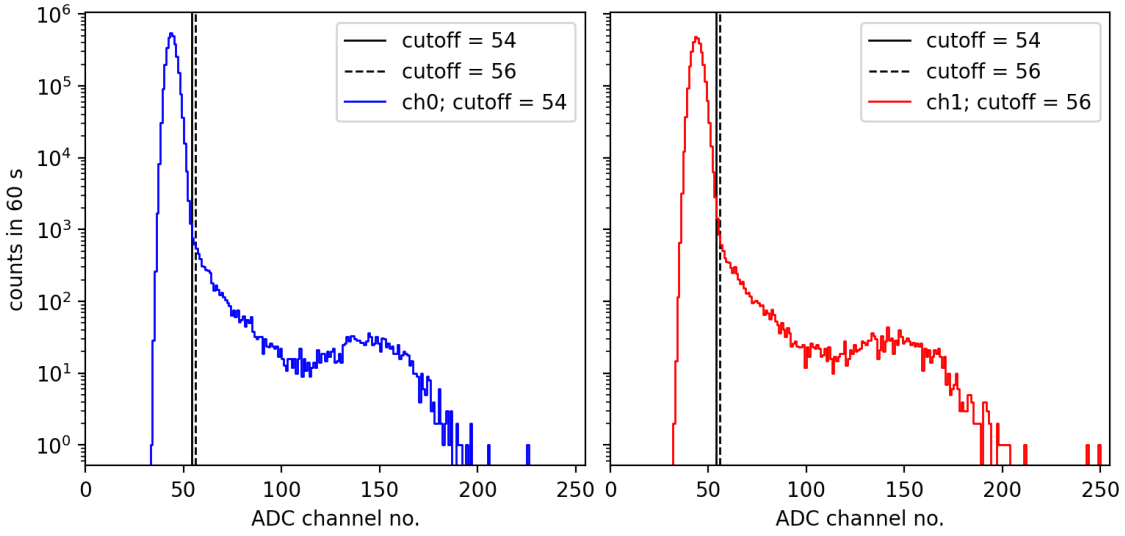

Figure 2.5: A comparison of a spectral background measurement taken by readout channel 0 (*left*) and channel 1 (*right*) of the GRBAlpha CubeSat. The measurements were done one orbit apart in low background region; both under the operational voltage of MPPCs of 178 DAC ($\sim$ 55 V). The vertical solid lines mark the ADC channel no. 54 which is used as a cutoff for channel 0. The vertical dashed lines mark the ADC channel no. 56 which is used as a cutoff for channel 1. The initial high noise peak is the thermal noise produced by the MPPCs and is wider for channel 1. This is likely due to the fact that the same operation voltage is used for both channels although the pre-flight calibrations were only done for channel 0 and channel 1 can have slightly different characteristics.

ionized from an inner shell, another electron from a higher shell will deexcite to occupy the vacant space while emitting a low-energy photon.

Often, the incident photon loses only part of its energy mainly via Compton scattering. Some of the photon energy is transferred to an electron and due to the energy loss, the photon's trajectory gets deflected. The resulting photon can further interact with the material, however, in case of small detectors such as ours it is more probable that it will escape. Low-energy photons can also scatter coherently. This means that they are scattered under an angle while the scattered photons have the same energy as the incident ones (Rayleigh scattering).

Photons with energy higher than double the rest energy of an electron (2×511 keV) interacting with the electric field of atomic nuclei can produce an electron–positron pair. In this case, the photon is fully absorbed and the abundant energy is transferred to the rest mass of the pair and their kinetic energies. In time, the positron annihilates with a nearby electron producing two photons with an energy of 511 keV if the positron is already at rest, or higher if it still carries some kinetic energy at the time of annihilation. Due to the detector size, these photons will usually escape the crystal.

The secondary electrons from the processes described above as well as charged particles from the ambient environment lose their energy continuously as they slow down when traveling through matter. Primarily, they ionize or excite atoms. When they move close to the atomic nucleus, they can be deflected and emit bremsstrahlung radiation.

As a result of all of these processes, the observed spectrum does not correspond to the real spectrum of incident particles but is softer. The amount of deposited energy depends on the incident energy, electron density of the material, and also on the direction of the incoming particle. To extract meaningful physical quantities from the data, we need to correct our measurements for these effects. This is done by the detector response matrix (DRM), a complex relation between the incident and detected energies, which needs to be simulated assuming the entire detector design and all of the possible interactions. Fig. 2.6 shows the on-axis DRM for GRBAlpha. The mean effective area for different directions is shown in Fig. 2.7. At the moment, the DRM for VZLUSAT-2 is not yet available.

2.2 GRBAlpha operations and measurements

GRBAlpha is currently operated interactively (Fig. 2.8) during passes over ground stations by students of the Masaryk University. The uplink communication is done via transmitters in Košice, Slovakia and at Konkoly observatory in Budapest, Hungary, and downlink is recorded by two receivers; one in Piszkéstető Observatory, Hungary and the other in Jablonec, Slovakia. GRBAlpha passes over these locations typically three times in the morning and three times in the evening, however, often the communication is efficient only during the highest pass. Daily interaction with the satellite is necessary due to an on-board watchdog counter which is set to 25 hours for safety reasons. If it is not reset in time, the system undergoes a power cycle, the payload enters a bootloader mode, and all of the scheduled measurements and downloads are lost. After such an occasion, the detector needs to be manually turned back on.

Routine operations consist of scheduling and downloading measurements. There are eight possibilities for spectral resolution. The entire energy range can be equally divided

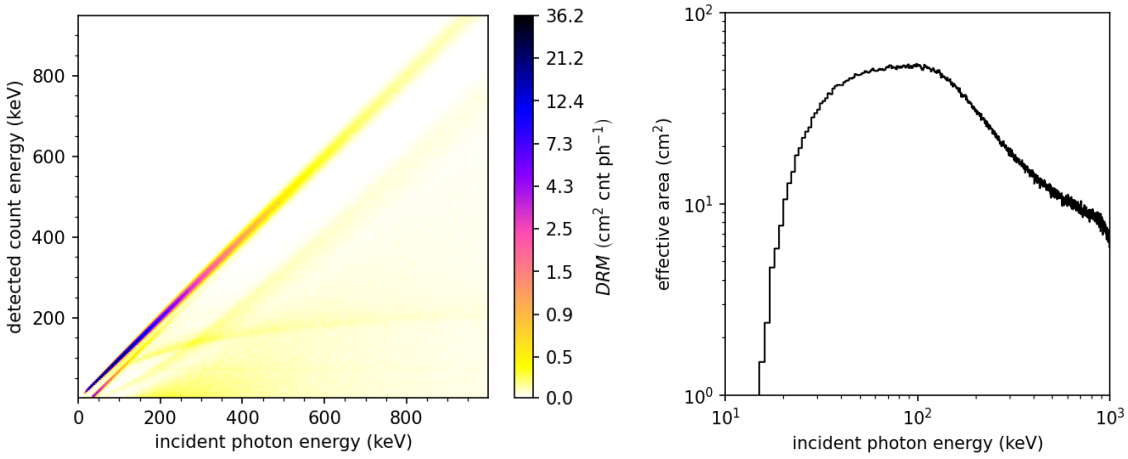

Figure 2.6: *Left*: Simulated on-axis detector response matrix for GRBAlpha. The strong diagonal line is the photopeak corresponding to the full absorption of the incident particle. The non-diagonal features are mostly due to various results of Compton scattering during which the incident particle is partially absorbed but the secondary particles escape from the crystal lattice and therefore the detected energy is lower than the incident energy. *Right:* Effective area vs. incident photon energy from the simulated detector response matrix. The maximum effective area $A_{\text{eff}} = 54$ cm^2 corresponds to the incident photon energy of ~ 100 keV.

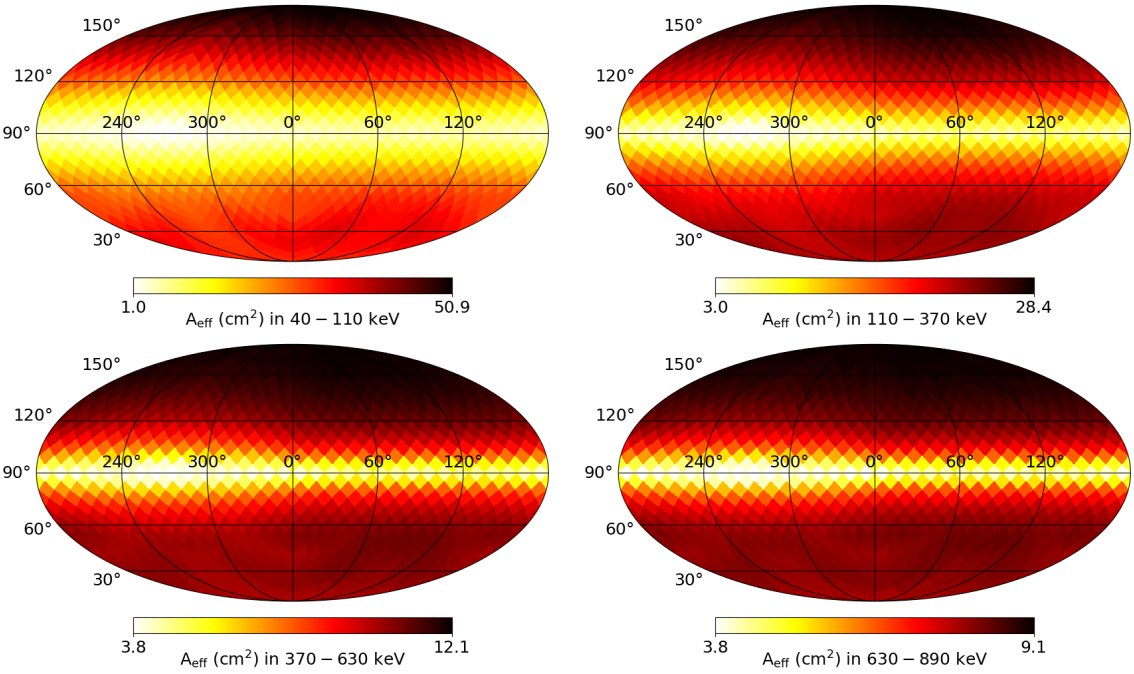

Figure 2.7: Mean effective area A_{eff} simulated for different energies shown in satellite coordinates θ (vertical) and ϕ (horizontal). The face of the detector corresponds to $\theta = 180$ degrees. At higher energies, the satellite is nearly transparent while at lower energies it absorbs around 40 % of the incoming radiation. The region with higher absorptivity around $\phi = 240 - 300$ degrees near edge-on point of view ($\theta = 90$ degrees) is due to the lead shielding of the MPPCs (see also Fig. 2.3).

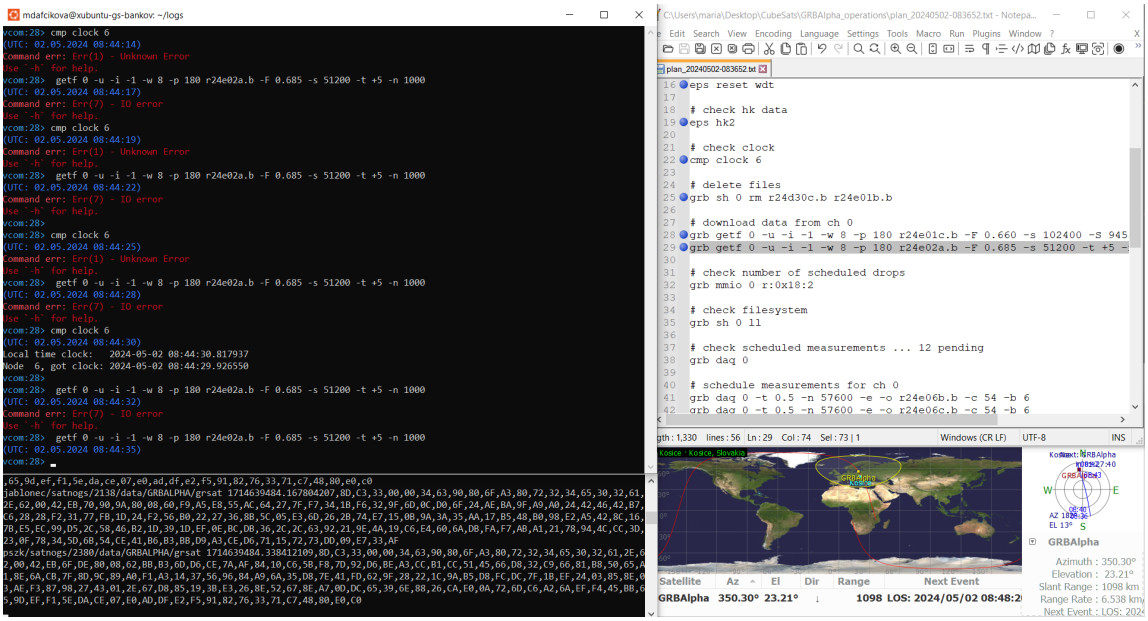

Figure 2.8: A screenshot of the author's screen during an operation of GRBAlpha. The top left panel is the main communication window, prepared commands to be executed are in the top right panel, the downlink stream is monitored in the bottom left panel and satellite's position with respect to the ground station is displayed in the bottom right window.

into 2^M spectral bins, where $M = \{1,..,8\}$ is the bit resolution of the ADC. Since launch, different combinations of exposure times and spectral resolution have been used. At the moment, the nominal measurements are done in four energy bands with 0.5 second exposure time. Apart from these, long 60 second measurements with full spectral resolution are done regularly to monitor the degradation of the MPPCs. If the conditions are favourable, the satellite is capable of nonstop observations.

To increase the downlink rate, we make use of the Satellite Networked Open Ground Station (SatNOGS[1]) network of amateur radio stations. During an operation we schedule data download for future passes above different stations shown in Fig. 2.9. However, the downlink rate is still not high enough to download the entire measurements. Therefore, we only download intervals when other missions were triggered, or when an interesting event, e.g. a strong geomagnetic storm, happened. We monitor triggers from following missions and observatories:

Fermi Gamma-Ray Space Telescope (formerly GLAST) is a NASA mission launched in 2008 to a near-equatorial LEO. Its primary instrument is the Large Area Telescope (LAT, Atwood et al. (2009)), a pair-conversion detector sensitive in the range of 20 MeV to 300 GeV, and a field of view of nearly 20 % of the sky. LAT is complemented by the Gamma-Ray Burst Monitor (GBM, Meegan et al. (2009)) which consists of 12 NaI(Tl) scintillators observing the lower energies from 8 keV to 1 MeV, and two bismuth germanate scintillation detectors (BGO) providing the measurements in 200 keV to 40 MeV used for cross-calibration of the low-energy

[1] https://network.satnogs.org/

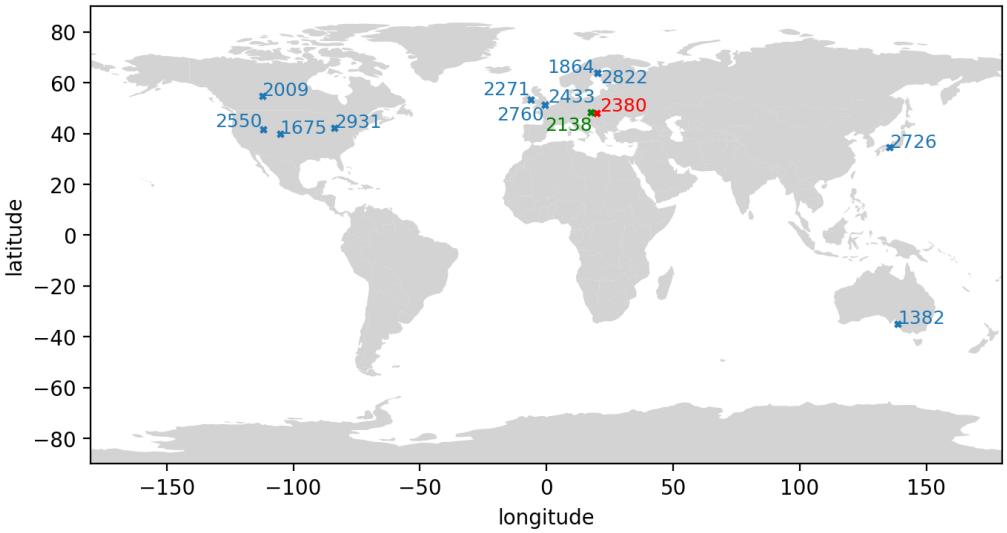

Figure 2.9: Locations of different SatNOGS stations used for downloading data from GRBAlpha. The Piszkéstető and Jablonec stations used for downlink during the interactive communication are highlighted in red and green, respectively.

detectors with the LAT. The NaI(Tl) detectors are arranged around the spacecraft in a specific way which enables to localize the high-energy source from the relative count rates detected by different units. The GBM's field of view is the entire sky except for the part which is occulted by the Earth, therefore, it detects the majority of GRBs.

Neil Gehrels Swift Observatory is a NASA mission launched in 2004 to LEO. It comprises three instruments designed to detect GRBs and begin multi-wavelength observations within a few minutes since trigger in X-ray and optical spectrum. The Burst Alert Telescope (BAT, Barthelmy et al. (2005b)), a gamma-ray detector with a field of view of 1.4 sr covers the energy range of 15 to 150 keV. It uses the coded-aperture mask to provide an initial position of the source with an accuracy of a few arcminutes and automatically initiates the repointing of the narrow field of view instruments to this position within a few seconds. The X-Ray Telescope (XRT, Burrows et al. (2005)) is a Wolter-type telescope with a CCD detector sensitive in the 0.2 to 10 keV energy band. It monitors the GRB afterglows for days to weeks after the burst. Finally, the Ultraviolet/Optical Telescope (UVOT, Roming et al. (2005)) is a 30 cm Ritchey-Chrétien reflector designed to observe the afterglows in the band from 170 to 600 nm. UVOT is capable of improving the localization below one arcsecond. Besides direct triggers from Swift/BAT, we also monitor the requests for the GUANO pipeline (Tohuvavohu et al., 2020) which include triggers of GRBs, gravitational waves, fast radio bursts, neutrino events and other very high-energy detections.

INTErnational Gamma-Ray Astrophysics Laboratory (INTEGRAL) is an ESA mission with the primary objective to provide fine spectroscopy and imaging of GRBs (Winkler et al., 2003). It carries four instruments; the high-resolution spectrometer

SPI sensitive in 20 keV–8 MeV, the high-angular resolution imager IBIS sensitive in 15 keV–10 MeV with a coded mask used to localize GRBs, and two complementary monitors in the X-ray (JEM-X) and optical Johnson V-band (OMC). INTEGRAL was launched in 2002 to a highly eccentric orbit in order to avoid the particle environment of the van Allen radiation belts.

Konus is a gamma-ray spectroscopic instrument on-board the NASA Wind spacecraft (Aptekar et al., 1995). It consists of two identical units of a NaI(Tl) scintillator read-out by photomultiplier tubes. The detector covers the energies from 10 keV to 10 MeV and is capable of short exposure time of 2 ms. The Wind satellite was launched in 1994 and is currently orbiting the Lagrange point 1 (L1) of the Sun-Earth system.

Astro-Rivelatore Gamma a Immagini Leggero (AGILE, Tavani et al. (2009)) is an Italian space mission which was launched in 2007 to LEO and de-orbited after 17 years of operations in February 2024 (Tavani et al., 2024). It carried three instruments observing from hard X-rays of $\sim$ 18 keV up to 50 GeV, with an anticoincidence system to suppress the background from charged particles.

AstroSat (Singh et al., 2014) is an Indian mission dedicated to multi-wavelength observations of various astrophysical sources from optical to hard X-ray band. The primary GRB-observing instrument is the Cadmium-Zinc-Telluride Imager (CZTI) with a coded aperture mask sensitive in 20–200 keV (Bhalerao et al., 2017). It is orbiting at a 650 km near-equatorial orbit since 2015.

GW high-energy Electromagnetic Counterpart All-sky Monitor (GECAM) is a Chinese constellation of two small satellites launched at the end of 2020. Both are orbiting at LEO but on the other sides of the Earth so they can provide an all-sky coverage. The payload is the same on each satellite unit and consists of the charged particle detector (CPD), a plastic scintillator coupled with SiPMs, and 25 gamma-ray detectors (GRD) made of $LaBr_3$:Ce scintillators read-out by SiPMs covering energies from 5 keV to 5 MeV (Li et al., 2020).

CALorimetric Electron Telescope (CALET, Torii et al. (2019)) is a telescope developed by the Japan Aerospace Exploration Agency (JAXA) flying aboard the ISS. It comprises of two scientific instruments; the calorimeter (CAL) sensitive to very high-energy electrons (1 GeV to 20 TeV), gamma-rays (10 GeV to 10 TeV), protons and heavy ions (10 GeV to 1 PeV), and the CALET Gamma-ray Burst Monitor (CGBM, Yamaoka et al. (2013)) composed of two LaBr3(Ce) scintillators and one BGO read-out by photomultipliers.

Monitor of All-sky X-ray Image (MAXI, Matsuoka et al. (2009)) is another instrument developed by JAXA and installed on the ISS. It is an X-ray telescope consisting of two slit cameras, two gas proportional counter detectors and X-ray CCDs, altogether sensitive in 2–30 keV. Due to its lower energy coverage, it does not detect many GRBs but more softer transients.

LIGO/Virgo/KAGRA is a collaboration of American LIGO (Abramovici et al., 1992), European VIRGO (Acernese et al., 2015) and Japanese KAGRA (Aso et al., 2013) gravitational wave detectors. We monitor the triggers from this network in order to contribute to the search for electromagnetic counterparts to gravitational waves.

2.3 VZLUSAT-2 measurements

VZLUSAT-2 is operated by the team of the Czech Aerospace Research Centre (VZLÚ). Both uplink and downlink communication is done via the ground station in Pilsen, Czech republic. Although measurements are often running continuously for several days, because there are more scientific instruments on-board, sometimes there is a longer period without any observations.

The nominal measurements with VZLUSAT-2 are currently done in four spectral bands with 1 second exposure time. The long 60 second spectral measurements are also done regularly. To select what to download, we use the same trigger monitoring as for GRBAlpha. However, the downlink rate is lower than that of GRBAlpha and therefore we only download few minutes of measurements around the trigger time (while for GRBAlpha it is usually an hour). Consequently, the amount of data from VZLUSAT-2 is much lower, yet, the detection rate is comparable (Fig. 4.2) because the downlink criteria are the same for both CubeSats.

Chapter 3

Methodology

3.1 Description of energy bands

In Ch. 4, we often express the energy bands in units of an ADC channel. Here we briefly describe the reasons for this choice.

Firstly, the dark current is very prominent at low energies as can be seen in the typical background spectra measured by the CubeSats in Fig. 2.5. To avoid this noise peak, we set a low-energy cutoff for nominal measurements. However, as mentioned in Sec. 2.1.2, the exact value differs not only for the two CubeSats but also for the two readout channels onboard GRBAlpha. Moreover, as the MPPCs degrade in time, the dark noise increases and progresses to higher energies. Therefore, the cutoff value needs to be regularly adjusted. The lowest energy band thus varies for individual detections. The exact cutoff value used during each detection of a transient is specified in Tab. 4.2 to 4.7.

Secondly, as stated in Sec. 2.1.1, the detector gain decreases in time. Because the energies are sampled equally by the PHA, the gain decrease shifts these energy bands towards higher energies in keV. At the time of writing, this shift is observed only in measurements done by GRBAlpha. In the analysis, we use the original energy conversion relation for detections until August 2022. Since then, we use the new relation. In case of VZLUSAT-2, we use the original relation for all detections.

Thirdly, the energy conversion relation depends on the operational voltage HV of the detector. The values stated in Sec. 2.1.1 are for the nominal value of 178 DAC. However, several measurements were done under a lower operational voltage of 168 DAC which decreases the detector sensitivity at low energies while increases the maximum detectable energy. The revised conversion relation for $HV = 168$ DAC follows

$$\mathrm{E}\ [\mathrm{keV}] = 5.61 \times \text{ADC channel no.} - 201. \tag{3.1}$$

This relation is used for analysis of transients detected by GRBAlpha in August and September 2022 when the lower operational voltage was used. The most often used values of ADC channel along with their corresponding energies in keV calculated for all three situations are summarized in Tab. 3.1.

Table 3.1: A list of most used values of ADC channel in the analysis and their approximate value in keV according to the original and revised conversion relation, and revised relation for lower operational voltage.

ADC ch.	$E_{\text{orig, HV=178}}$ (keV)	$E_{\text{rev, HV=178}}$ (keV)	$E_{\text{rev, HV=168}}$ (keV)
45	30	40	50
48	40	50	70
54	70	80	100
56	75	90	110
64	110	120	160
127	370	400	510
255	890	950	1230

3.2 Observational characteristics of transients

Prior to any analysis, the raw data is normalized to count rate CR:

$$CR = \frac{C}{t_{\text{exp}}}, \tag{3.2}$$

where C is the number of counts detected during the exposure t_{exp} which is the temporal resolution of a given light curve. Each detection of a photon is an independent event, therefore, the detected number of counts at a specific time is subject to a Poisson uncertainty equal to a square root of the value itself. The 1σ uncertainty of the count rate is then

$$\sigma_{CR} = \frac{\sqrt{C}}{t_{\text{exp}}} = \sqrt{\frac{CR}{t_{\text{exp}}}}. \tag{3.3}$$

3.2.1 Background fitting

In order to properly analyse each burst, we need to estimate the amount of noise in the detected signal. At LEO, the contributors to the background level in the energy range of $10-1000$ keV are mostly cosmic X-rays, galactic gamma-rays, trapped electrons and protons, and albedo gamma-rays and neutrons (Galgóczi et al., 2021). The background level also depends on the satellite location because at SS LEO it frequently encounters the SAA and radiation belts (Fig. 3.1). Another background fluctuations are due to the satellite rotation, and temporary changes are also present at times of increased solar activity. It is therefore a non-trivial task to precisely determine an absolute value of the background level at a given time. Taking all this into account, we do not analyse the background in general but rather we look at its current state.

For each burst, we manually determine its start $T_{100,\text{s}}$ and end time $T_{100,\text{e}}$, and background intervals (Fig. 3.2a). The background is then fitted by a linear function and a second-order polynomial. The best fit is selected by the lowest reduced χ^2 (Fig. 3.2b):

$$\chi^2_\nu = \frac{\chi^2}{\nu}, \tag{3.4}$$

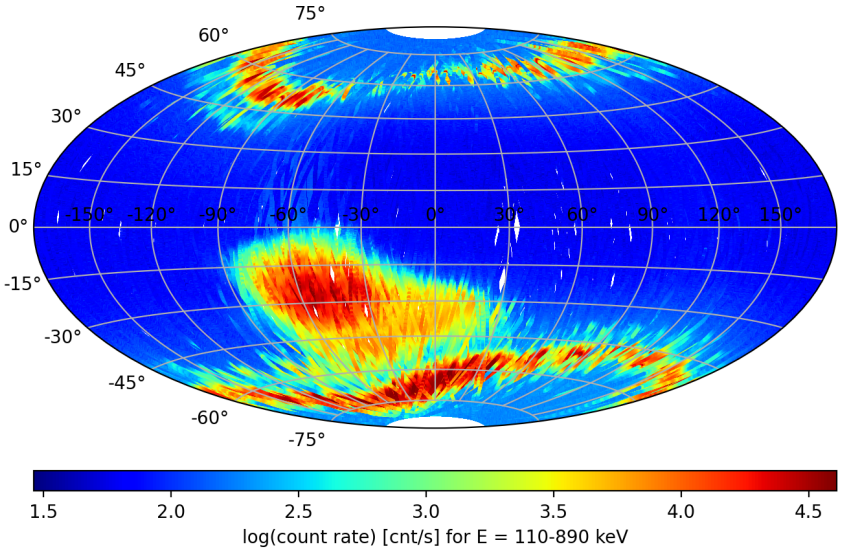

Figure 3.1: A map of the particle background measured by GRBAlpha presented in geographic coordinates. The variable high background regions correspond to the van Allen radiation belts and the SAA.

where ν is the number of degrees of freedom calculated as the total amount of temporal bins in the background regions minus the number of fitted parameters, and χ^2 is given by

$$\chi^2 = \sum_i \frac{(C_i - C_{i,\mathrm{fit}})^2}{C_{i,\mathrm{fit}}}, \tag{3.5}$$

where C_i is the number of detected counts in i-th background bin and $C_{i,\mathrm{fit}}$ is the expected value based on the best polynomial fit. The fit is done on count rate data and in the χ^2 calculation it is multiplied by the exposure time. The background fit is then subtracted from all data points and background-subtracted light curve is produced (Fig. 3.2c). In further analysis, we work with these reduced light curves.

3.2.2 T_{90} duration

A GRB duration is generally described by the T_{90} duration which is the period during which the middle 90 % of the signal is detected, i.e. the cumulative distribution function (CDF) increases from 0.05 to 0.95 (Fig. 3.2d). In this work, we use this quantity to describe the duration of all types of transients. Because most transients are only observed in the two lowest energy bands, we calculate the T_{90} in 0–127 ADC band.

The observed duration of short events is restricted by the temporal resolution of the measurement while the duration uncertainty of longer bursts is given predominantly by statistical fluctuations. The uncertainty $\sigma_{T_{90}}$ is therefore calculated as a superposition of the two:

$$\sigma_{T_{90}} = \sqrt{\sigma_{stat}^2 + t_{exp}^2}. \tag{3.6}$$

The statistical uncertainty σ_{stat} of each event was estimated via a Monte Carlo (MC) simulation. We reproduced 10 000 light curves with added Poisson noise to each temporal

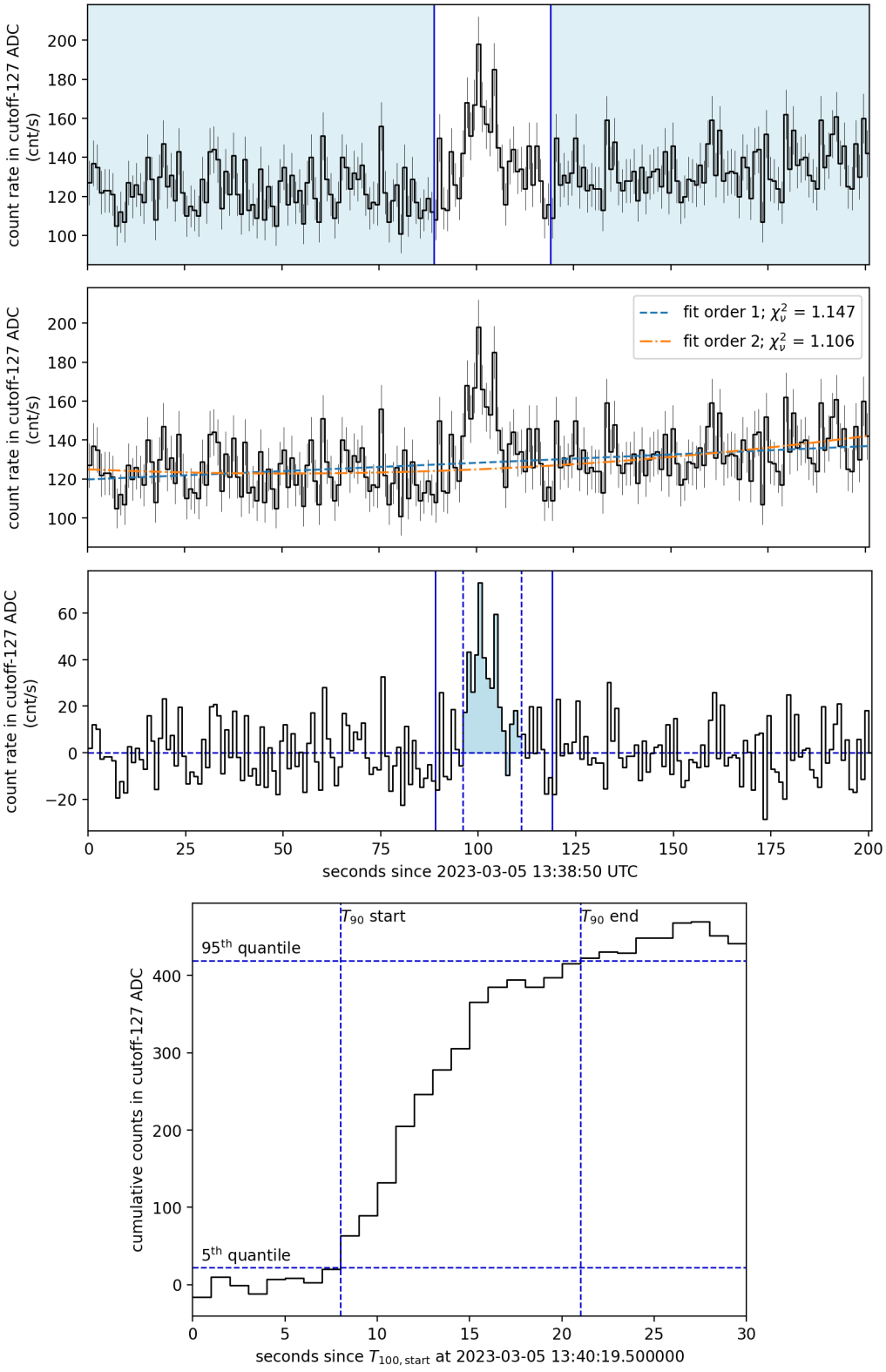

Figure 3.2: An example of the event analysis for GRB 230305A. *From top to bottom*: raw light curve of the event with user-selected background regions shown in blue and T_{100} limits of the event delimited by the vertical solid lines; background fits by a linear function and a second-order polynomial; background-subtracted light curve using fit with lower reduced χ^2, vertical dashed lines represent the T_{90} duration and fluence is shown in blue; cumulative counts during the event duration and the T_{90} determination.

bin, and calculated the T_{90} for each simulation while the background intervals and the T_{100} of an event remained the same in each simulation. The median of the distribution was then taken as the final T_{90} and the lower and upper 1σ uncertainties are computed as the 0.159-th and 0.841-th quantiles, respectively (Fig. 3.3).

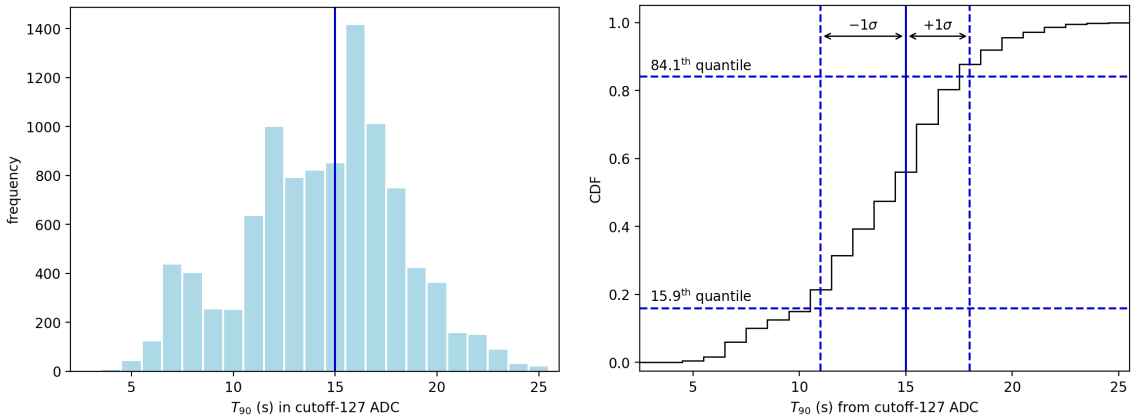

Figure 3.3: An example of the determination of the T_{90} duration and its uncertainties for GRB 230305A. *Left*: Histogram of T_{90} durations from 10 000 MC simulations. *Right*: Cumulative distribution function of the T_{90} durations from MC simulations. The vertical solid line marks the median of the distribution and the dashed lines show the 1σ statistical uncertainties.

3.2.3 Peak flux

We define the peak flux P of a burst as the number of detected counts per second at a peak time determined from the entire energy range 0–255 ADC. The exact value and its uncertainty are calculated according to Eq. 3.2 and 3.3.

3.2.4 Fluence

The fluence S is defined as a time-integrated flux, i.e the sum of all counts detected between the start t_s and the end t_e of the T_{90} duration (Fig. 3.2c):

$$S = \sum_{i=t_s}^{t_e} (CR_i - CR_{i,\mathrm{fit}}) t_{\mathrm{exp}}. \tag{3.7}$$

Similarly to the uncertainty of the T_{90}, the fluence error also has two components. Firstly, the fluence highly depends on the T_{90} itself and its uncertainty. Therefore, in each of the MC simulations described in Sec 3.2.2 we also computed the fluence. Its lower and upper 1σ uncertainties are then computed from the distribution as the 0.159-th and 0.841-th quantiles, analogically to the uncertainties of the T_{90}. Secondly, a standard Poisson uncertainty of the observed counts during T_{90} is calculated according to the error propagation theory:

$$\sigma_{\mathrm{obs}} = \sqrt{\sum_i \sigma_i^2} = \sqrt{\sum_i CR_i \; t_{\mathrm{exp}}}. \tag{3.8}$$

The final σ_S is again computed as a superposition of the two aforementioned uncertainties:

$$\sigma_S = \sqrt{\sigma_{\mathrm{MC}}^2 + \sigma_{\mathrm{obs}}^2}. \tag{3.9}$$

3.2.5 Hardness ratio

The hardness ratio HR is defined as the ratio of fluence in harder and softer energy band. Because most of the transients were detected only in the two lowest energy bands, we only include the HR between these two bands, i.e.

$$HR = \frac{S_1}{S_0} = \frac{S(64-127\ \mathrm{ADC})}{S(0-63\ \mathrm{ADC})}. \tag{3.10}$$

Its uncertainty is then computed according to the error propagation theory as

$$\sigma_{HR} = HR\sqrt{\left(\frac{\sigma_{S_1}}{S_1}\right)^2 + \left(\frac{\sigma_{S_0}}{S_0}\right)^2}. \tag{3.11}$$

3.2.6 Signal-to-noise ratio

The significance of a detection is characterized by the signal-to-noise ratio (SNR). We calculate the SNR within the entire T_{90} duration of a burst as the absolute value of the fluence divided by the uncertainty related to the measurement (Eq. 3.8):

$$SNR = \frac{S}{\sigma_{\mathrm{obs}}}. \tag{3.12}$$

We define detections with $SNR \geq 5\sigma$ as *significant* detections and those with $3\sigma \leq SNR \leq 5\sigma$ as *sub-threshold* detections. In case of sub-threshold detections, we always cross-check our light curve with light curves observed by other missions such as Fermi/GBM, Swift/BAT, or INTEGRAL/SPI-ACS (Sec. 2.2).

3.3 Theoretical sensitivity of the detector

To characterize the sensitivity of our detector, we calculate the expected GRB threshold fluence S_{thr} of a 5σ detection assuming a face-on direction of the incident photons. The threshold SNR is calculated according to Eq. 3.12:

$$SNR_{\mathrm{thr}} = \frac{C^{\mathrm{GRB}}}{\sqrt{C^{\mathrm{GRB}} + C^{\mathrm{BGD}}}} = 5, \tag{3.13}$$

where C^{BGD} is the number of background counts during the T_{90} duration of a GRB, estimated from the lowest count rate measured near the equator ($C^{\mathrm{BGD}} \approx T_{90} \times 120$ cnt/s), and C^{GRB} is the number of GRB photons detected during the T_{90}. The latter is computed as an integral of a typical GRB spectrum N_E multiplied by the DRM over the energies of the incident photons E^{ph}, the energies of the detected counts E^{cnt} and time. Assuming

that the GRB intensity is constant in time, the integration over time is equal to the T_{90} duration. The DRM was simulated in discrete steps, specifically, the incident photon energies were simulated in range $E^{\mathrm{ph}} = 1 - 1000$ keV with a step of $\Delta E^{\mathrm{ph}} = 1$ keV, and the detected count energies were simulated in the range $E^{\mathrm{cnt}} = 0 - 255$ ADC ch. with a step of $\Delta E^{\mathrm{cnt}} = 1$ ADC ch. Therefore, instead of integration we use summation:

$$C^{\mathrm{GRB}} = T_{90} \sum_j N_E(E_j^{\mathrm{ph}}) \Delta E^{\mathrm{ph}} \sum_i DRM_{ij}(E_i^{\mathrm{cnt}}, E_j^{\mathrm{ph}}) \Delta E^{\mathrm{cnt}}. \tag{3.14}$$

In Sec. 4.2, we compare the calculated S_{thr} with GRBs observed by Fermi/GBM. Therefore, we compute the expected GRB fluence in the same energy ranges as Fermi/GBM provides, i.e. we use $j = 10 - 1000$ keV and $j = 50 - 300$ keV in Eq. 3.14. Similarly, because our CubeSats use different low-energy cutoffs, we compute the S_{thr} individually for both. We use $i = 54 - 255$ ADC ch. for GRBAlpha and $i = 48 - 255$ ADC ch. for VZLUSAT-2.

A typical differential photon spectrum of a GRB can be described by a power law model with an exponential cutoff (CPL, most commonly used in the Fermi/GBM catalogue):

$$N_E = \frac{\mathrm{d}N}{\mathrm{d}E} = A \left(\frac{E}{100\ \mathrm{keV}} \right)^{\alpha} \exp\left(-\frac{(\alpha+2)E}{E_{\mathrm{peak}}} \right), \tag{3.15}$$

where A is a normalization factor, α is a power law index and E_{peak} is the peak energy of the GRB spectrum. In order to find the threshold fluence, we set α and E_{peak} to their typical values (Tab. 4.8), and adjust the normalization factor so that $SNR = 5$. Finally, to get the threshold fluence we multiply the integrated differential photon spectrum by the typical T_{90} duration:

$$S_{\mathrm{thr}} = T_{90} \int N_E(A_{\mathrm{thr}}, \alpha, E_{\mathrm{peak}}) \mathrm{d}E. \tag{3.16}$$

Chapter 4

Results and discussion

4.1 Catalogue of detected transients

The catalogue contains 198 gamma-ray transients detected by the detectors on-board the GRBAlpha[1] and VZLUSAT-2[2] CubeSats. Fifteen of these events were observed jointly by both CubeSats. All of the detections were confirmed by correlation with light curves measured by other missions mentioned in Sec. 2.2. If the transient was localized, we also verified that it was not occulted by the Earth. The spatial distribution of all localized GRBs is displayed in Fig. 4.1. The blank regions are likely only a result of the small sample size.

Majority of the observed events are gamma-ray bursts and solar flares. Few flashes from two different magnetars were detected and one outburst from an X-ray binary, too. The number of detections of each transient type for both satellites is summarized in Tab. 4.1. Observed characteristics of individual events are presented in Tab. 4.2 to 4.7. We include the T_{90} duration, peak flux P in two energy bands, fluence S in four energy bands, the ratio HR of the fluence in the two lowest energy bands, and the SNR at the peak time and during the T_{90}. The light curves of all detected transients are presented in Appendix A.

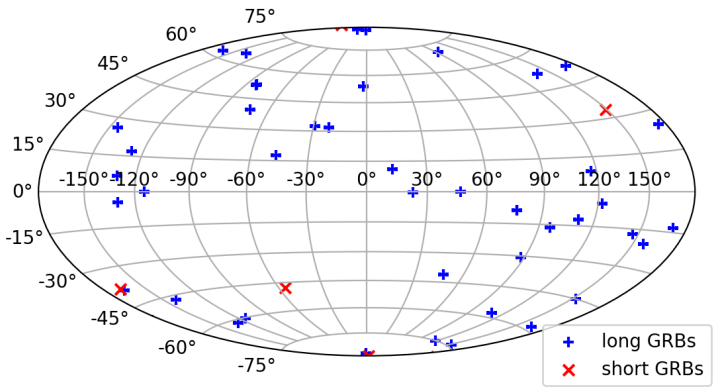

Figure 4.1: All GRBs detected by GRBAlpha and VZLUSAT-2 which were also detected and localized by Fermi/GBM or Swift shown in equatorial coordinates.

[1] GRBAlpha detections are regularly reported at https://monoceros.physics.muni.cz/hea/GRBAlpha/.
[2] VZLUSAT-2 detections are regularly reported at https://monoceros.physics.muni.cz/hea/VZLUSAT-2/.

Table 4.1: Summary of detected transients by both GRBAlpha and VZLUSAT-2 by 30 April 2024. The number of independent events is shown in brackets, i.e. if an event was detected by more satellites or channels, it is only included once. Note that GRBAlpha carries only one detector unit so both channels measure counts from the same scintillator, while the two channels for VZLUSAT-2 correspond to different detector units which are placed perpendicularly to each other.

	GRBAlpha		VZLUSAT-2		
	ch0	ch1	ch0	ch2	
gamma-ray burst	76	4	19	42	141 (112)
short	13	1	–	3	17 (17)
long	63	3	19	39	124 (95)
soft gamma repeater	2	–	1	5	8 (6)
solar flare	43	5	15	30	93 (79)
X-ray binary	1	–	–	–	1 (1)
	122	9	35	77	
	131 (131)		112 (83)		243 (198)

4.1.1 Detection rate

GRBAlpha has detected 131 events in its first 37 months of operation. 126 of these were observed in the past 21 months which yields one detection every five days. The top part of Fig. 4.2 shows the number of detected transients per month since launch. The increased number of detections since August 2022 is a result of a software upgrade which allowed us to perform nearly continuous measurements, except for periods with ground station issues. Considering only periods when GRBAlpha measured non-stop for at least one week, it detected on average 2 transients per week out of which one was a GRB. Due to the polar orbit, GRBAlpha spends around 40 % of the time in high background regions of the Earth's radiation belts. The field of view from a 550 km LEO is approximately 8.8 sr. Correcting for these two effects, we get $\sim$ 250 transients, or $\sim$ 125 GRBs per year which would be detected by a constellation of satellites which would provide an all-sky coverage from low background regions at all times.

The detection rate is, however, not uniform in time. Especially, the frequency of observed solar flares increases as the solar maximum is approaching. On the other hand, detections of soft gamma repeaters and flashes from X-ray binaries are sporadic. The most successful month for GRBAlpha was February 2024 when it detected seven GRBs and eight solar flares, i.e. one event every two days. The busiest day was February 2, 2024 when GRBAlpha observed one GRB and three solar flares. The minimum time between two subsequent detections was 42 minutes between GRB 230709B and GRB 230709C.

VZLUSAT-2 has detected 83 transients in the first 26 months of operation. This corresponds to one detection in 10 days. However, the GRB detectors on-board VZLUSAT-2 are not constantly turned on. The observations are regulated based on needs of other instruments and the gamma-ray detectors can be turned off if more power is needed for different

tasks. The bottom part of Fig. 4.2 shows the monthly detection rate for VZLUSAT-2 since its launch. Since solar flares are among the softer sources, as demonstrated in Fig. 4.3 and discussed in Sec. 4.1.2, the higher number of solar flares observed in the first half of 2023 by VZLUSAT-2 can be related to lower low-energy threshold used for VZLUSAT-2 measurements at that time. In September 2023, the threshold had to be increased which reduced the number of solar flares observed by VZLUSAT-2 and diminished the difference in their detection rate between the two CubeSats.

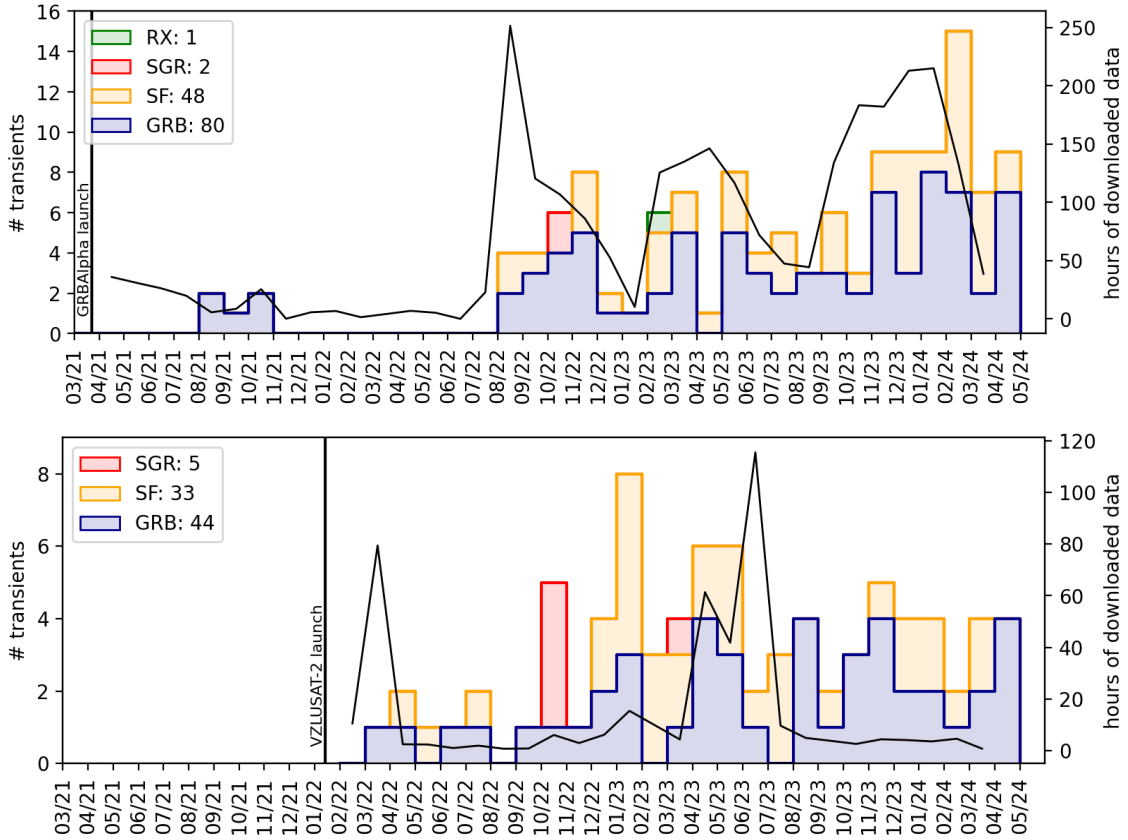

Figure 4.2: Detection rate of all transients detected by GRBAlpha (top) and by VZLUSAT-2 (bottom), and the amount of data downloaded from each CubeSat (black curves). In case of GRBAlpha, we observe regular detections since August 2022. This time corresponds to a satellite firmware upgrade which allowed us to dramatically increase the duty cycle and run observations nearly non-stop. The dips in amount of data at the turn of $2022 - 2023$ and in summer 2023 are related to problems with ground station. After the launch of VZLUSAT-2, there was about three-month-long period before the satellite became fully functional and commissioned. Therefore, during this early stage the number of detections was very reduced. From VZLUSAT-2 we only download few minutes around a specific trigger time, therefore, on average we have much less data downloaded than from GRBAlpha. The peak in amount of data shortly after the launch is due to mapping of the LEO background. In spring of 2023, there were joint observations of different payloads on VZLUSAT-2 and VZLUSAT-1.

Table 4.2: GRBs detected by GRBAlpha. Columns are: GRB name, GRBAlpha read-out channel which acquired the data, low-energy cutoff, exposure time t_{exp}, peak time of the detection, T_{90} duration, peak flux P in two different energy bands, fluence S in four different energy bands, hardness ratio HR between the two lowest energy bands, SNR at the peak time and during the T_{90} in the 0–127 ADC band, and the GCN Circular number in which the detection was announced. Explanation of the energy bands can be found in Sec. 3.1. GCN Circulars which are marked with an asterix were prepared by the author of this work. The very first GRB detected, GRB 210807A, was already ongoing when measurements were initiated. Therefore, for this detection we only provide lower limits of the T_{90} and fluence.

name	channel	cutoff	t_{exp}	peak time	T_{90}	P in 0–255 ADC	P in 0–127 ADC	S in 0–63 ADC	S in 64-127 ADC	S in 0–127 ADC	S in 0–255 ADC	HR	SNR_p	$SNR_{T_{90}}$	GCN no.
		ADC ch.	s	UTC	s	cnt/s	cnt/s	cnt	cnt	cnt	cnt	–	–	–	
GRB 210807A	0	54	4.0	2021-08-07 10:06:00.0	>64	44.17 ± 7.55	16.73 ± 4.62	>246.18	>895.14	>1141.32	>822.45	–	7.0	>11	30624
GRB 210822A	0	54	4.0	2021-08-22 09:18:26.0	$12.0^{+5.66}_{-5.66}$	419.15 ± 14.53	418.62 ± 13.53	$1284.22^{+61.49}_{-650.26}$	$2155.04^{+62.82}_{-1028.72}$	$3439.26^{+90.97}_{-1676.63}$	$3522.92^{+92.87}_{-1679.18}$	$1.68^{+0.09}_{-1.17}$	30.9	40.6	30697
GRB 210909A	0	54	4.0	2021-09-09 10:43:19.0	$4.0^{+4.0}_{-4.0}$	50.33 ± 7.4	50.16 ± 6.75	$65.44^{+8.09}_{-8.09}$	$133.2^{+11.54}_{-11.54}$	$200.64^{+14.16}_{-14.16}$	$201.32^{+14.19}_{-14.19}$	$2.04^{+0.31}_{-0.31}$	7.4	14.2	30840
GRB 211018A	0	54	4.0	2021-10-18 22:29:34.0	$124.0^{+4.0}_{-12.65}$	256.26 ± 9.87	249.19 ± 9.54	$5311.44^{+113.97}_{-204.2}$	$8952.85^{+125.68}_{-264.55}$	$14508.57^{+169.66}_{-466.71}$	$14920.25^{+177.86}_{-491.47}$	$1.69^{+0.04}_{-0.08}$	26.1	85.5	30945
GRB 211019A	0	54	4.0	2021-10-19 05:59:34.0	$36.0^{+5.66}_{-8.94}$	228.54 ± 10.19	194.08 ± 9.05	$720.11^{+59.12}_{-60.41}$	$2146.16^{+79.64}_{-85.71}$	$2876.02^{+108.14}_{-117.7}$	$3282.92^{+148.58}_{-140.29}$	$2.98^{+0.27}_{-0.28}$	21.5	32.8	30946
GRB 220826B	0	54	3.0	2022-08-26 10:21:20.4	$6.0^{+6.71}_{-3.0}$	37.44 ± 9.13	33.54 ± 7.02	$126.72^{+22.81}_{-59.9}$	$60.6^{+20.2}_{-30.86}$	$187.32^{+29.59}_{-89.82}$	$188.3^{+38.25}_{-85.07}$	$0.48^{+0.18}_{-0.33}$	4.8	6.3	32696*
GRB 220829A	0	54	3.0	2022-08-29 14:37:50.4	$12.0^{+4.24}_{-4.24}$	123.11 ± 10.51	110.75 ± 9.21	$452.45^{+66.32}_{-74.25}$	$397.05^{+37.22}_{-99.27}$	$862.22^{+53.48}_{-127.1}$	$888.47^{+58.43}_{-126.71}$	$0.88^{+0.15}_{-0.26}$	12.0	16.9	32697*
GRB 220915A	0	54	4.0	2022-09-15 05:13:42.8	$8.0^{+5.66}_{-5.66}$	47.45 ± 7.2	44.32 ± 6.17	$192.18^{+48.27}_{-88.79}$	$138.52^{+29.0}_{-76.84}$	$339.92^{+71.09}_{-166.31}$	$354.87^{+77.63}_{-169.93}$	$0.72^{+0.24}_{-0.52}$	7.2	9.8	32629*
GRB 220926B	0	54	4.0	2022-09-26 10:38:21.2	$4.0^{+16.49}_{-5.66}$	20.45 ± 6.93	26.53 ± 6.13	$32.93^{+16.55}_{-36.85}$	$73.18^{+46.03}_{-75.38}$	$106.11^{+34.11}_{-108.91}$	$81.82^{+27.73}_{-86.39}$	$2.22^{+1.79}_{-3.38}$	4.3	4.3	32781*
GRB 220927A	0	54	4.0	2022-09-27 05:36:25.2	$8.0^{+8.94}_{-5.66}$	95.11 ± 7.27	97.11 ± 6.98	$382.02^{+32.6}_{-219.33}$	$264.37^{+28.72}_{-171.88}$	$648.11^{+49.65}_{-390.28}$	$643.11^{+55.69}_{-382.49}$	$0.69^{+0.1}_{-0.6}$	13.9	17.1	32622
GRB 221009A	0	54	4.0	2022-10-09 13:20:51.4	$48.0^{+4.0}_{-4.0}$	21263.46 ± 74.14	15999.68 ± 64.46	$148110.68^{+404.04}_{-404.04}$	$367586.62^{+618.94}_{-618.94}$	$515697.3^{+739.14}_{-739.14}$	$606814.61^{+801.57}_{-801.57}$	$2.48^{+0.01}_{-0.01}$	248.2	697.7	32685
GRB 221020A	0	54	4.0	2022-10-20 05:23:59.7	$16.0^{+5.66}_{-4.0}$	67.55 ± 7.28	63.61 ± 6.74	$380.44^{+104.59}_{-37.27}$	$363.06^{+108.11}_{-35.16}$	$736.27^{+204.47}_{-51.23}$	$746.71^{+209.51}_{-55.26}$	$0.95^{+0.39}_{-0.13}$	9.4	14.4	32815
GRB 221022B	0	54	4.0	2022-10-22 22:56:11.7	$28.0^{+5.66}_{-5.66}$	170.28 ± 9.92	165.08 ± 8.69	$716.08^{+74.54}_{-55.32}$	$1276.06^{+81.61}_{-56.75}$	$1992.14^{+136.31}_{-77.87}$	$2056.93^{+144.19}_{-91.22}$	$1.78^{+0.22}_{-0.16}$	19.0	26.1	32844*
GRB 221029A	0	54	4.0	2022-10-29 01:05:27.7	$32.0^{+8.94}_{-8.94}$	58.86 ± 6.96	52.76 ± 6.5	$225.25^{+48.39}_{-73.55}$	$431.61^{+48.21}_{-93.62}$	$656.86^{+71.85}_{-152.6}$	$706.75^{+74.27}_{-172.08}$	$1.92^{+0.46}_{-0.75}$	8.1	9.9	32890
GRB 221107A	0	54	1.0	2022-11-07 01:25:57.1	$263.0^{+3.16}_{-2.24}$	113.2 ± 15.36	112.48 ± 14.83	$3348.69^{+140.89}_{-141.54}$	$2981.88^{+132.44}_{-144.42}$	$6330.57^{+194.09}_{-211.04}$	$6722.99^{+205.66}_{-219.83}$	$0.89^{+0.05}_{-0.06}$	7.6	34.1	32917*
GRB 221112A	0	54	1.0	2022-11-12 06:18:04.1	$13.0^{+7.07}_{-11.05}$	38.47 ± 13.34	40.29 ± 12.65	$10.97^{+45.13}_{-31.02}$	$140.96^{+34.43}_{-122.29}$	$151.93^{+41.36}_{-128.32}$	$134.01^{+44.15}_{-115.38}$	$12.85^{+52.94}_{-38.0}$	3.2	3.7	32937*
GRB 221119A	0	54	1.0	2022-11-19 15:02:55.1	$53.0^{+3.16}_{-3.16}$	298.75 ± 20.69	287.82 ± 19.95	$1003.36^{+61.81}_{-69.81}$	$1203.99^{+72.38}_{-65.85}$	$2159.18^{+99.06}_{-98.18}$	$2199.73^{+104.68}_{-104.3}$	$1.2^{+0.1}_{-0.11}$	14.4	24.2	32953
GRB 221122A	0	54	1.0	2022-11-22 02:43:26.1	$3.0^{+2.24}_{-1.41}$	45.92 ± 13.42	46.27 ± 12.69	$12.68^{+14.27}_{-13.88}$	$29.65^{+34.21}_{-14.54}$	$42.89^{+40.6}_{-19.95}$	$57.83^{+40.87}_{-22.26}$	$2.34^{+3.77}_{-2.81}$	3.6	2.2	32977*
GRB 221127A	0	54	1.0	2022-11-27 08:27:10.1	$5.0^{+1.41}_{-1.41}$	40.06 ± 12.61	37.17 ± 11.87	$42.04^{+19.46}_{-19.25}$	$46.23^{+16.38}_{-25.96}$	$89.27^{+25.62}_{-31.41}$	$97.73^{+26.37}_{-38.03}$	$1.1^{+0.64}_{-0.8}$	3.1	3.6	32991*
GRB 221206B	0	54	1.0	2022-12-06 12:22:48.8	$8.0^{+1.41}_{-1.0}$	491.08 ± 26.57	493.28 ± 24.98	$1152.68^{+45.7}_{-40.87}$	$986.43^{+57.65}_{-38.86}$	$2133.61^{+84.08}_{-56.39}$	$2127.02^{+84.44}_{-62.03}$	$0.86^{+0.06}_{-0.05}$	19.7	37.8	33028*
GRB 230102A	0	54	1.0	2023-01-02 00:22:13.0	$1.0^{+1.0}_{-1.41}$	75.47 ± 14.04	70.24 ± 13.19	$24.12^{+8.89}_{-26.56}$	$46.14^{+9.75}_{-49.03}$	$70.24^{+13.19}_{-74.26}$	$75.47^{+14.04}_{-81.33}$	$1.91^{+0.81}_{-2.93}$	5.3	5.3	33143*
GRB 230204B	0	54	1.0	2023-02-04 21:47:02.8	$214.0^{+6.08}_{-5.1}$	145.19 ± 17.38	138.94 ± 16.0	$364.53^{+122.76}_{-126.34}$	$3825.64^{+144.94}_{-148.67}$	$4435.47^{+187.86}_{-202.46}$	$3389.19^{+206.96}_{-213.59}$	$10.49^{+3.56}_{-3.66}$	8.7	25.6	33273*
GRB 230207B	0	54	1.0	2023-02-07 04:40:47.8	$10.0^{+1.0}_{-1.41}$	317.77 ± 25.0	309.0 ± 23.49	$569.06^{+44.33}_{-51.19}$	$1156.5^{+46.31}_{-57.55}$	$1719.36^{+64.11}_{-87.13}$	$1739.15^{+68.99}_{-91.12}$	$2.03^{+0.18}_{-0.21}$	13.2	26.8	33303*
GRB 230304B	0	54	1.0	2023-03-04 14:35:48.8	$17.0^{+1.41}_{-2.24}$	431.83 ± 24.49	434.58 ± 23.9	$681.64^{+48.41}_{-55.98}$	$1200.19^{+49.35}_{-75.15}$	$1868.12^{+71.85}_{-111.96}$	$1880.12^{+74.28}_{-117.89}$	$1.76^{+0.14}_{-0.18}$	18.2	28.8	33398*
GRB 230305A	0	54	1.0	2023-03-05 13:40:30.8	$15.0^{+3.16}_{-4.12}$	73.73 ± 15.17	73.08 ± 14.07	$191.44^{+38.11}_{-57.05}$	$228.52^{+33.91}_{-48.37}$	$419.96^{+48.62}_{-88.78}$	$412.5^{+52.58}_{-83.09}$	$1.19^{+0.3}_{-0.44}$	5.2	8.8	33417*
GRB 230307A	0	54	1.0	2023-03-07 15:44:11.8	$25.0^{+1.0}_{-1.0}$	9200.87 ± 97.36	8474.5 ± 93.32	$28346.58^{+177.35}_{-177.35}$	$66030.16^{+265.59}_{-265.59}$	$94376.73^{+319.36}_{-319.36}$	$100593.89^{+330.66}_{-330.66}$	$2.33^{+0.02}_{-0.02}$	90.8	295.5	33418*
GRB 230320B	0	54	1.0	2023-03-20 21:12:26.8	$34.0^{+3.16}_{-3.16}$	243.68 ± 19.26	236.57 ± 18.33	$1064.67^{+58.69}_{-63.95}$	$652.45^{+48.63}_{-57.54}$	$1757.01^{+80.44}_{-107.34}$	$1740.28^{+89.89}_{-100.51}$	$0.61^{+0.06}_{-0.07}$	12.9	24.6	33503*
GRB 230328B	0	54	1.0	2023-03-28 14:54:48.8	$7.0^{+1.41}_{-1.41}$	215.29 ± 21.61	209.61 ± 19.54	$359.61^{+30.77}_{-40.46}$	$342.78^{+31.01}_{-44.76}$	$682.25^{+47.77}_{-71.66}$	$654.61^{+52.39}_{-73.36}$	$0.95^{+0.12}_{-0.16}$	10.7	15.6	33543*

Table 4.2 (*continued*): GRBs detected by GRBAlpha.

name	channel	cutoff	t_{exp}	peak time (UTC)	T_{90}	P in 0–255 ADC	P in 0–127 ADC	S in 0–63 ADC	S in 64-127 ADC	S in 0–127 ADC	S in 0–255 ADC	HR	SNR_{p}	$SNR_{\mathrm{T_{90}}}$	GCN no.
		ADC ch.	s	UTC	s	cnt/s	cnt/s	cnt	cnt	cnt	cnt	–	–	–	
GRB 230510A	0	54	1.0	2023-05-10 12:06:31.2	$29.0^{+1.41}_{-2.24}$	41.49±12.81	36.98±12.04	$69.35^{+43.37}_{-46.94}$	$173.57^{+46.63}_{-39.97}$	$242.92^{+62.36}_{-61.01}$	$289.52^{+66.82}_{-65.43}$	$2.5^{+1.7}_{-1.79}$	3.1	4.2	33794*
GRB 230510B	0	54	1.0	2023-05-10 21:21:50.2	$198.0^{+3.16}_{-3.16}$	115.98±32.19	96.15±20.32	$2255.49^{+162.26}_{-168.11}$	$1034.23^{+210.29}_{-216.68}$	$3289.71^{+269.33}_{-283.21}$	$3279.06^{+428.17}_{-443.99}$	$0.46^{+0.1}_{-0.1}$	4.7	12.9	33811*
GRB 230512A	0	54	1.0	2023-05-12 06:27:47.3	$5.0^{+1.41}_{-2.24}$	127.22±16.58	124.37±15.75	$64.18^{+22.42}_{-26.5}$	$254.97^{+23.59}_{-108.83}$	$318.75^{+32.87}_{-124.39}$	$357.35^{+35.28}_{-138.21}$	$3.97^{+1.44}_{-2.36}$	7.9	10.4	33795*
GRB 230522A	1	56	1.0	2023-05-22 03:34:45.2	$10.0^{+1.41}_{-1.0}$	587.93±26.8	569.48±26.08	$1123.92^{+58.95}_{-41.69}$	$1903.97^{+64.22}_{-50.24}$	$3043.78^{+106.28}_{-64.42}$	$3099.32^{+109.39}_{-66.34}$	$1.69^{+0.11}_{-0.08}$	21.8	47.2	33905*
GRB 230523B	0	54	1.0	2023-05-23 15:23:54.0	$1.0^{+1.0}_{-1.0}$	79.29±16.43	63.82±14.73	$22.24^{+4.72}_{-4.72}$	$41.43^{+6.44}_{-6.44}$	$63.82^{+7.99}_{-7.99}$	$79.29^{+8.9}_{-8.9}$	$1.86^{+0.49}_{-0.49}$	4.3	8.0	33875*
GRB 230604A	0	54	1.0	2023-06-04 05:53:47.6	$1.0^{+1.0}_{-1.41}$	100.48±15.23	94.96±14.42	$36.4^{+9.8}_{-37.7}$	$58.18^{+10.58}_{-59.13}$	$94.96^{+14.42}_{-96.05}$	$100.48^{+15.23}_{-101.63}$	$1.6^{+0.52}_{-2.32}$	6.6	6.6	33927*
GRB 230614C	1	56	1.0	2023-06-14 10:10:32.5	$6.0^{+1.0}_{-1.41}$	750.28±29.38	735.72±28.84	$890.04^{+34.0}_{-72.19}$	$1461.27^{+42.11}_{-76.63}$	$2351.31^{+54.12}_{-138.69}$	$2403.63^{+55.5}_{-139.72}$	$1.64^{+0.08}_{-0.16}$	25.5	43.4	33984*
GRB 230626A	0	54	1.0	2023-06-26 14:30:29.1	$14.0^{+2.24}_{-1.0}$	194.98±21.28	195.06±19.31	$482.64^{+52.13}_{-40.84}$	$772.62^{+58.54}_{-45.83}$	$1276.2^{+94.48}_{-61.38}$	$1292.67^{+90.83}_{-70.04}$	$1.6^{+0.21}_{-0.17}$	10.1	20.8	34099*
GRB 230709B	1	56	1.0	2023-07-09 16:56:15.2	$6.0^{+1.41}_{-1.0}$	87.82±16.03	79.09±14.39	$79.97^{+28.16}_{-19.22}$	$243.6^{+27.77}_{-34.77}$	$323.8^{+42.77}_{-41.55}$	$319.12^{+49.4}_{-41.32}$	$3.05^{+1.13}_{-0.85}$	5.5	9.8	34200*
GRB 230709C	1	56	1.0	2023-07-09 17:38:26.2	$1.0^{+1.0}_{-1.41}$	157.11±17.18	133.71±15.72	$22.02^{+8.6}_{-23.64}$	$112.08^{+13.15}_{-116.75}$	$133.71^{+15.72}_{-134.63}$	$157.11^{+17.18}_{-165.94}$	$5.09^{+2.08}_{-7.62}$	8.5	8.5	34201*
GRB 230826A	0	54	1.0	2023-08-26 19:32:44.5	$20.0^{+2.24}_{-4.12}$	46.16±14.11	42.66±13.23	$169.43^{+43.04}_{-39.8}$	$225.7^{+40.89}_{-49.63}$	$395.12^{+59.39}_{-59.33}$	$399.16^{+64.76}_{-62.87}$	$1.33^{+0.42}_{-0.43}$	3.2	7.2	34572*
GRB 230827A	0	54	1.0	2023-08-27 18:18:13.5	$75.0^{+7.07}_{-4.12}$	237.9±19.29	235.6±18.84	$1552.84^{+84.86}_{-86.83}$	$1746.08^{+100.75}_{-75.38}$	$3298.92^{+136.54}_{-114.84}$	$3504.33^{+141.54}_{-122.34}$	$1.12^{+0.09}_{-0.08}$	12.5	29.8	34583*
GRB 230828A	0	54	1.0	2023-08-28 16:29:52.5	$138.0^{+2.24}_{-4.12}$	105.37±15.52	103.37±14.93	$2105.05^{+116.66}_{-120.64}$	$1790.45^{+107.83}_{-92.19}$	$3681.67^{+169.98}_{-154.93}$	$3755.25^{+174.53}_{-161.17}$	$0.85^{+0.07}_{-0.07}$	6.9	25.9	34590*
GRB 230908A	0	54	1.0	2023-09-08 16:41:21.4	$7.0^{+1.41}_{-1.0}$	555.6±27.46	554.25±26.59	$965.58^{+59.91}_{-39.01}$	$1547.43^{+91.05}_{-45.46}$	$2513.01^{+138.03}_{-59.91}$	$2515.17^{+147.12}_{-62.55}$	$1.6^{+0.14}_{-0.08}$	20.8	41.9	34647*
GRB 230911B	0	54	1.0	2023-09-11 04:25:51.4	$15.0^{+2.24}_{-2.24}$	148.42±19.67	148.81±17.8	$247.06^{+43.77}_{-48.33}$	$572.25^{+50.26}_{-45.1}$	$819.32^{+73.12}_{-62.48}$	$869.0^{+73.66}_{-71.95}$	$2.32^{+0.46}_{-0.49}$	8.4	14.2	34664*
GRB 230911D	0	54	1.0	2023-09-11 07:53:25.8	$45.0^{+1.41}_{-1.41}$	512.95±25.16	495.23±24.45	$2006.27^{+72.33}_{-68.03}$	$3509.2^{+84.73}_{-84.31}$	$5515.46^{+120.73}_{-113.21}$	$5661.02^{+125.87}_{-121.72}$	$1.75^{+0.08}_{-0.07}$	20.3	54.7	34712*
GRB 231018A	0	54	1.0	2023-10-18 12:31:08.0	$33.0^{+1.41}_{-2.24}$	1219.76±36.69	1209.5±36.3	$6471.78^{+110.66}_{-107.57}$	$4769.35^{+89.34}_{-99.63}$	$11229.64^{+175.92}_{-167.25}$	$11296.06^{+181.17}_{-175.21}$	$0.74^{+0.02}_{-0.02}$	33.3	92.2	34850*
GRB 231030B	0	54	1.0	2023-10-30 19:58:20.7	$20.0^{+2.24}_{-1.41}$	179.07±17.55	171.39±16.85	$286.09^{+52.91}_{-39.38}$	$531.99^{+39.49}_{-40.6}$	$818.08^{+69.53}_{-56.1}$	$844.56^{+73.81}_{-59.14}$	$1.86^{+0.37}_{-0.29}$	10.2	14.7	34923*
GRB 231106B	0	54	1.0	2023-11-06 21:19:01.1	$1.0^{+1.41}_{-1.0}$	89.1±14.56	78.28±13.67	$31.66^{+16.04}_{-9.59}$	$46.78^{+24.83}_{-9.75}$	$78.28^{+38.05}_{-13.67}$	$89.1^{+35.52}_{-14.56}$	$1.48^{+1.08}_{-0.54}$	5.7	5.7	34998*
GRB 231117A	0	54	1.0	2023-11-17 03:03:19.3	$1.0^{+1.0}_{-1.0}$	325.57±22.69	309.66±20.98	$159.57^{+12.63}_{-12.63}$	$150.1^{+12.25}_{-12.25}$	$309.66^{+17.6}_{-17.6}$	$325.57^{+18.04}_{-18.04}$	$0.94^{+0.11}_{-0.11}$	14.8	17.6	35095*
GRB 231118A	0	54	1.0	2023-11-18 17:16:33.4	$6.0^{+3.16}_{-2.24}$	73.02±14.56	63.94±13.38	$49.33^{+21.36}_{-35.24}$	$120.72^{+71.36}_{-21.82}$	$170.05^{+58.83}_{-42.73}$	$180.86^{+66.58}_{-50.65}$	$2.45^{+1.79}_{-1.8}$	4.8	5.8	35151*
GRB 231124A	0	54	1.0	2023-11-24 08:38:16.7	$21.0^{+4.12}_{-3.16}$	66.01±14.46	64.3±13.56	$279.09^{+44.3}_{-60.24}$	$361.03^{+39.5}_{-52.33}$	$640.13^{+60.59}_{-85.42}$	$672.19^{+64.26}_{-92.51}$	$1.29^{+0.25}_{-0.34}$	4.7	11.4	35193*
GRB 231125A	0	54	1.0	2023-11-25 17:47:20.8	$2.0^{+1.0}_{-1.41}$	199.32±20.4	193.43±19.62	$140.45^{+18.87}_{-83.03}$	$210.4^{+19.42}_{-114.23}$	$350.85^{+27.07}_{-195.32}$	$357.85^{+28.11}_{-201.29}$	$1.5^{+0.24}_{-1.2}$	9.9	13.0	35199*
GRB 231127A	0	54	1.0	2023-11-27 05:14:20.9	$5.0^{+1.41}_{-1.41}$	196.3±19.26	178.48±17.35	$299.75^{+27.64}_{-53.18}$	$237.37^{+25.15}_{-40.5}$	$532.42^{+40.04}_{-86.34}$	$555.47^{+42.95}_{-98.88}$	$0.79^{+0.11}_{-0.19}$	10.3	15.7	35224*
GRB 231129C	0	54	1.0	2023-11-29 19:10:19.0	$6.0^{+1.0}_{-1.0}$	2288.33±49.1	2278.93±48.87	$3749.66^{+64.34}_{-64.34}$	$5100.8^{+73.23}_{-73.23}$	$8848.66^{+97.48}_{-97.48}$	$8927.02^{+98.3}_{-98.3}$	$1.36^{+0.03}_{-0.03}$	46.6	90.8	35236*
GRB 231208A	0	54	1.0	2023-12-08 02:29:45.5	$3.0^{+1.41}_{-1.0}$	43.54±13.08	45.17±12.41	$28.51^{+15.84}_{-14.76}$	$67.0^{+14.28}_{-14.75}$	$95.51^{+20.65}_{-20.54}$	$95.61^{+21.86}_{-21.87}$	$2.35^{+1.4}_{-1.32}$	3.6	4.6	35309*
GRB 231215A	0	54	1.0	2023-12-15 09:47:26.6	$16.0^{+2.24}_{-1.0}$	427.17±28.32	423.53±25.73	$1792.48^{+128.11}_{-59.47}$	$2223.61^{+144.95}_{-65.54}$	$4016.09^{+258.38}_{-88.5}$	$4137.26^{+256.1}_{-100.67}$	$1.24^{+0.12}_{-0.06}$	16.5	45.4	35380*
GRB 231222B	0	54	1.0	2023-12-22 07:26:04.0	$5.0^{+1.41}_{-1.41}$	57.06±13.08	56.76±12.53	$80.79^{+21.98}_{-25.79}$	$87.59^{+19.99}_{-17.8}$	$168.22^{+33.05}_{-32.92}$	$165.78^{+34.21}_{-34.5}$	$1.08^{+0.38}_{-0.41}$	4.5	6.5	35425*
GRB 240101C	0	54	1.0	2024-01-01 12:57:23.5	$1.0^{+1.0}_{-1.0}$	60.55±16.34	62.0±14.0	$19.99^{+4.47}_{-4.47}$	$41.61^{+6.45}_{-6.45}$	$62.0^{+7.87}_{-7.87}$	$60.55^{+7.78}_{-7.78}$	$2.08^{+0.57}_{-0.57}$	4.4	7.9	35459*
GRB 240106A	0	54	1.0	2024-01-06 00:36:36.7	$144.0^{+10.05}_{-9.06}$	112.16±16.25	104.94±14.8	$753.29^{+102.5}_{-108.11}$	$1677.69^{+98.85}_{-119.85}$	$2314.86^{+142.72}_{-169.57}$	$2421.48^{+160.3}_{-193.68}$	$2.23^{+0.33}_{-0.36}$	7.1	16.8	35497*

Table 4.2 (*continued*): GRBs detected by GRBAlpha.

name	channel	cutoff	t_{exp}	peak time (UTC)	T_{90}	P in 0–255 ADC	P in 0–127 ADC	S in 0–63 ADC	S in 64-127 ADC	S in 0–127 ADC	S in 0–255 ADC	HR	SNR_p	$SNR_{T_{90}}$	GCN no.
		ADC ch.	s	UTC	s	cnt/s	cnt/s	cnt	cnt	cnt	cnt	–	–	–	
GRB 240112C	0	54	1.0	2024-01-12 17:37:25.1	$5.0^{+1.41}_{-1.41}$	144.34±17.8	136.72±16.09	$276.09^{+33.52}_{-25.64}$	$131.45^{+19.82}_{-23.03}$	$411.83^{+34.8}_{-36.61}$	$452.6^{+38.28}_{-45.63}$	$0.48^{+0.09}_{-0.09}$	8.5	12.9	35536*
GRB 240118A	0	54	1.0	2024-01-18 01:49:21.8	$57.0^{+1.41}_{-1.0}$	1682.4±43.23	1640.94±42.07	$17698.64^{+167.77}_{-147.31}$	$19180.93^{+170.36}_{-150.06}$	$36876.08^{+264.75}_{-210.28}$	$38024.9^{+278.94}_{-220.55}$	$1.08^{+0.01}_{-0.01}$	39.0	175.4	35580*
GRB 240123A	0	54	1.0	2024-01-23 11:07:50.5	$12.0^{+5.1}_{-4.12}$	34.67±13.75	25.59±11.7	$80.72^{+30.96}_{-38.23}$	$86.21^{+26.04}_{-40.72}$	$166.93^{+43.08}_{-66.47}$	$161.43^{+44.6}_{-72.03}$	$1.07^{+0.52}_{-0.71}$	2.2	4.4	35628*
GRB 240123C	0	54	1.0	2024-01-23 23:12:36.5	$2.0^{+1.0}_{-1.41}$	236.23±21.21	235.31±19.8	$164.0^{+17.69}_{-116.71}$	$201.7^{+19.05}_{-122.79}$	$363.0^{+26.0}_{-236.74}$	$367.9^{+28.2}_{-237.9}$	$1.23^{+0.18}_{-1.15}$	11.9	14.0	35643*
GRB 240125A	0	54	1.0	2024-01-25 09:34:59.6	$1.0^{+1.0}_{-1.0}$	54.79±13.15	44.19±12.08	$4.98^{+2.23}_{-2.23}$	$39.21^{+6.26}_{-6.26}$	$44.19^{+6.65}_{-6.65}$	$54.79^{+7.4}_{-7.4}$	$7.87^{+3.75}_{-3.75}$	3.7	6.6	35645*
GRB 240128A	0	54	1.0	2024-01-28 15:13:45.8	$13.0^{+1.0}_{-2.24}$	66.09±16.94	54.44±14.66	$121.2^{+31.58}_{-34.79}$	$270.9^{+38.7}_{-51.67}$	$406.5^{+49.95}_{-73.15}$	$396.99^{+57.17}_{-74.74}$	$2.24^{+0.66}_{-0.77}$	3.7	8.1	35649*
GRB 240213A	0	54	0.5	2024-02-13 20:11:48.2	$44.0^{+1.12}_{-1.12}$	277.14±29.66	274.71±28.5	$1143.53^{+64.45}_{-68.95}$	$1486.34^{+72.85}_{-70.31}$	$2629.87^{+99.03}_{-102.49}$	$2635.56^{+105.83}_{-111.86}$	$1.3^{+0.1}_{-0.1}$	9.6	28.6	35745*
GRB 240215B	0	54	0.5	2024-02-15 19:51:48.8	$15.0^{+2.55}_{-2.06}$	267.76±28.43	265.19±27.71	$652.41^{+48.94}_{-49.81}$	$644.68^{+41.86}_{-37.47}$	$1297.08^{+71.88}_{-61.85}$	$1310.19^{+71.17}_{-64.85}$	$0.99^{+0.1}_{-0.09}$	9.6	23.4	35752*
GRB 240216A	0	54	0.5	2024-02-16 10:57:02.9	$1.5^{+0.5}_{-0.71}$	230.9±28.91	207.72±26.53	$46.8^{+12.27}_{-14.95}$	$114.33^{+15.23}_{-46.99}$	$161.13^{+19.44}_{-56.7}$	$185.91^{+21.61}_{-73.7}$	$2.44^{+0.72}_{-1.27}$	7.8	8.3	35753*
GRB 240222A	0	54	0.5	2024-02-22 08:51:30.9	$1.5^{+0.71}_{-0.5}$	80.21±20.0	69.89±18.76	$36.83^{+12.25}_{-14.61}$	$58.03^{+11.05}_{-20.0}$	$94.86^{+16.42}_{-30.51}$	$100.3^{+16.77}_{-34.34}$	$1.58^{+0.6}_{-0.83}$	3.7	6.0	35792*
GRB 240225C	0	54	0.5	2024-02-25 05:19:36.6	$8.0^{+1.58}_{-1.58}$	63.0±22.98	58.15±20.3	$119.9^{+32.23}_{-30.17}$	$105.98^{+33.46}_{-28.45}$	$205.42^{+49.88}_{-42.95}$	$204.02^{+53.69}_{-43.53}$	$0.88^{+0.37}_{-0.33}$	2.9	5.5	35802*
GRB 240226A	0	54	0.5	2024-02-26 19:33:09.6	$8.0^{+1.12}_{-0.71}$	52.86±19.29	54.97±18.65	$59.89^{+31.8}_{-24.49}$	$85.0^{+23.55}_{-27.49}$	$144.89^{+41.09}_{-34.7}$	$143.92^{+41.45}_{-36.88}$	$1.42^{+0.85}_{-0.74}$	2.9	4.4	35827*
GRB 240229A	0	54	0.5	2024-02-29 14:07:33.3	$24.5^{+1.12}_{-1.58}$	111.31±24.66	104.64±22.18	$178.97^{+58.91}_{-46.84}$	$284.4^{+47.4}_{-61.32}$	$463.37^{+71.08}_{-69.8}$	$564.15^{+78.51}_{-85.53}$	$1.59^{+0.59}_{-0.54}$	4.7	7.4	35894*
GRB 240329A	0	54	0.5	2024-03-29 21:43:07.7	$6.5^{+0.5}_{-0.71}$	174.64±24.33	174.55±23.66	$312.83^{+25.59}_{-26.24}$	$262.56^{+24.41}_{-24.64}$	$566.67^{+35.37}_{-36.37}$	$581.44^{+37.0}_{-38.21}$	$0.84^{+0.1}_{-0.11}$	7.4	16.0	35997*
GRB 240331A	0	54	0.5	2024-03-31 23:55:19.3	$8.0^{+4.03}_{-2.06}$	74.84±23.83	58.65±20.59	$97.06^{+31.18}_{-36.57}$	$162.69^{+33.65}_{-50.46}$	$262.61^{+51.43}_{-75.89}$	$278.58^{+48.57}_{-92.76}$	$1.68^{+0.64}_{-0.82}$	2.8	6.8	36035*
GRB 240402C	0	54	0.5	2024-04-02 05:30:53.0	$90.0^{+4.53}_{-42.0}$	69.38±19.9	61.21±18.65	$206.92^{+76.98}_{-82.6}$	$616.73^{+74.14}_{-196.15}$	$823.66^{+106.04}_{-171.71}$	$801.68^{+112.04}_{-184.78}$	$2.98^{+1.17}_{-1.52}$	3.3	7.8	36036*
GRB 240405A	0	54	0.5	2024-04-05 15:07:38.5	$24.0^{+2.55}_{-7.02}$	73.74±23.66	66.3±20.88	$173.97^{+46.39}_{-54.0}$	$212.04^{+46.34}_{-51.66}$	$417.38^{+66.32}_{-89.68}$	$443.49^{+75.59}_{-91.42}$	$1.22^{+0.42}_{-0.48}$	3.2	6.6	36054*
GRB 240408B	0	54	0.5	2024-04-08 00:10:03.8	$44.5^{+2.06}_{-2.06}$	66.79±19.29	68.69±18.55	$336.75^{+55.8}_{-60.66}$	$261.53^{+51.51}_{-49.28}$	$617.4^{+75.99}_{-87.55}$	$535.09^{+78.51}_{-90.06}$	$0.78^{+0.2}_{-0.2}$	3.7	8.5	36062*
GRB 240411A	0	54	0.5	2024-04-11 01:44:59.9	$0.5^{+0.5}_{-0.5}$	77.54±20.49	70.27±19.39	$6.43^{+2.54}_{-2.54}$	$28.71^{+5.36}_{-5.36}$	$35.14^{+5.93}_{-5.93}$	$38.77^{+6.23}_{-6.23}$	$4.47^{+1.95}_{-1.95}$	3.6	5.9	36068*
GRB 240421B	0	54	0.5	2024-04-21 09:42:53.6	$3.0^{+1.12}_{-1.58}$	178.95±27.64	164.01±25.3	$146.14^{+22.48}_{-54.79}$	$149.13^{+23.64}_{-47.61}$	$295.27^{+33.19}_{-95.24}$	$285.27^{+40.08}_{-100.42}$	$1.02^{+0.23}_{-0.5}$	6.5	10.7	36269*
GRB 240425A	0	54	0.5	2024-04-25 00:21:16.4	$29.0^{+2.55}_{-2.55}$	70.45±22.45	47.6±18.97	$354.79^{+73.09}_{-51.57}$	$136.95^{+45.1}_{-45.99}$	$491.74^{+92.33}_{-65.77}$	$451.12^{+107.41}_{-76.11}$	$0.39^{+0.15}_{-0.14}$	2.5	7.5	36350*
GRB 240430A	0	54	0.5	2024-04-30 19:21:24.7	$11.0^{+1.12}_{-1.12}$	128.38±22.09	124.29±21.26	$544.37^{+40.22}_{-44.72}$	$280.91^{+30.91}_{-30.21}$	$809.3^{+52.56}_{-58.58}$	$796.62^{+55.46}_{-57.4}$	$0.52^{+0.07}_{-0.07}$	5.8	18.4	36373*

Table 4.3: Solar flares detected by GRBAlpha. Columns are: name analogical to GRB naming convention, GRBAlpha read-out channel which acquired the data, low-energy cutoff, exposure time t_{exp}, peak time of the detection, T_{90} duration, peak flux P in two different energy bands, fluence S in four different energy bands, hardness ratio HR between the two lowest energy bands, and SNR at the peak time and during the T_{90} in the 0–127 ADC band. Explanation of the energy bands can be found in Sec. 3.1.

name	channel	cutoff	t_{exp}	peak time (UTC)	T_{90}	P in 0–255 ADC	P in 0–127 ADC	S in 0–63 ADC	S in 64-127 ADC	S in 0–127 ADC	S in 0–255 ADC	HR	SNR_p	$SNR_{T_{90}}$
		ADC ch.	s	UTC	s	cnt/s	cnt/s	cnt	cnt	cnt	cnt	–	–	–
SF 220815	0	54	4.0	2022-08-15 14:35:06.0	$96.0^{+8.94}_{-8.94}$	160.02±9.38	156.76±8.65	$3815.33^{+156.67}_{-185.61}$	$360.02^{+93.48}_{-89.65}$	$3902.29^{+148.41}_{-159.57}$	$4312.62^{+176.59}_{-192.43}$	$0.09^{+0.02}_{-0.02}$	18.1	29.5
SF 220816	0	54	4.0	2022-08-16 00:08:38.0	$48.0^{+8.94}_{-5.66}$	40.17±6.51	37.64±6.02	$1237.53^{+64.82}_{-106.18}$	$73.54^{+50.35}_{-47.41}$	$1326.59^{+80.61}_{-116.77}$	$1288.81^{+87.38}_{-128.71}$	$0.06^{+0.04}_{-0.04}$	6.3	16.5
SF 220904	0	54	3.0	2022-09-04 12:13:29.3	$9.0^{+4.24}_{-4.24}$	43.45±7.39	43.06±6.93	$212.81^{+44.86}_{-37.62}$	$26.83^{+40.46}_{-21.19}$	$240.55^{+70.99}_{-36.34}$	$221.05^{+74.21}_{-36.1}$	$0.13^{+0.19}_{-0.1}$	6.2	7.1
SF 221111a	0	54	1.0	2022-11-11 05:54:49.1	$42.0^{+3.16}_{-4.12}$	51.67±15.26	44.53±13.04	$744.12^{+61.11}_{-75.23}$	$63.7^{+55.36}_{-51.64}$	$807.82^{+85.86}_{-90.2}$	$747.74^{+97.9}_{-97.66}$	$0.09^{+0.07}_{-0.07}$	3.4	10.4
SF 221111b	0	54	1.0	2022-11-11 11:39:32.1	$45.0^{+6.08}_{-3.16}$	139.07±20.69	141.2±18.3	$855.29^{+93.33}_{-97.38}$	$-38.42^{+72.55}_{-75.04}$	$763.01^{+110.55}_{-121.94}$	$693.11^{+130.44}_{-135.41}$	$-0.04^{+-0.08}_{--0.09}$	7.7	7.9
SF 221111c	0	54	1.0	2022-11-11 13:49:12.1	$12.0^{+3.16}_{-2.24}$	93.41±16.58	73.91±14.49	$295.73^{+46.99}_{-63.54}$	$20.36^{+29.76}_{-29.93}$	$320.42^{+53.14}_{-73.14}$	$304.71^{+60.05}_{-62.9}$	$0.07^{+0.1}_{-0.1}$	5.1	7.2
SF 221229	0	54	1.0	2022-12-29 18:19:44.3	$161.0^{+4.12}_{-6.08}$	62.33±14.49	51.55±13.34	$2014.71^{+131.31}_{-164.09}$	$669.24^{+109.64}_{-107.39}$	$2746.49^{+181.39}_{-197.2}$	$2918.34^{+192.19}_{-217.29}$	$0.33^{+0.06}_{-0.06}$	3.9	18.0
SF 230210	0	54	1.0	2023-02-10 03:00:33.8	$13.0^{+1.41}_{-3.16}$	51.6±15.3	42.75±13.34	$320.27^{+36.77}_{-51.66}$	$-15.56^{+39.61}_{-30.05}$	$304.72^{+55.75}_{-50.91}$	$316.83^{+66.68}_{-57.73}$	$-0.05^{+-0.12}_{--0.09}$	3.2	6.7
SF 230211	0	54	1.0	2023-02-11 15:45:57.8	$59.0^{+1.41}_{-1.0}$	411.74±25.65	399.82±23.58	$8663.03^{+232.68}_{-114.41}$	$1083.08^{+79.13}_{-76.49}$	$9746.11^{+261.95}_{-137.62}$	$9675.6^{+274.15}_{-155.48}$	$0.12^{+0.01}_{-0.01}$	17.0	70.8
SF 230222	0	54	1.0	2023-02-22 13:47:59.8	$154.0^{+9.06}_{-7.07}$	155.42±17.72	152.57±16.79	$4352.06^{+160.15}_{-166.72}$	$261.99^{+100.05}_{-114.55}$	$4750.03^{+188.49}_{-231.12}$	$4665.7^{+189.09}_{-245.21}$	$0.06^{+0.02}_{-0.03}$	9.1	30.2
SF 230308	0	54	1.0	2023-03-08 22:41:58.8	$40.0^{+2.24}_{-3.16}$	46.81±13.45	49.42±12.88	$585.65^{+57.47}_{-92.12}$	$-15.81^{+44.44}_{-44.66}$	$575.81^{+72.69}_{-105.4}$	$531.3^{+77.93}_{-109.01}$	$-0.03^{+-0.08}_{--0.08}$	3.8	7.9
SF 230312	0	54	1.0	2023-03-12 06:07:16.8	$12.0^{+9.06}_{-5.1}$	47.88±13.08	43.76±12.33	$235.88^{+53.72}_{-62.46}$	$41.91^{+27.46}_{-26.57}$	$277.79^{+62.59}_{-74.79}$	$266.19^{+87.62}_{-76.45}$	$0.18^{+0.12}_{-0.12}$	3.5	7.0
SF 230417	0	54	1.0	2023-04-17 06:32:49.4	$34.0^{+3.16}_{-5.1}$	65.09±17.0	54.06±14.0	$565.93^{+65.3}_{-60.14}$	$353.56^{+53.38}_{-54.44}$	$937.72^{+84.96}_{-84.99}$	$801.4^{+98.73}_{-91.74}$	$0.62^{+0.12}_{-0.12}$	3.9	12.4
SF 230501	1	56	1.0	2023-05-01 13:08:00.2	$89.0^{+3.16}_{-3.16}$	624.82±28.07	625.59±27.5	$3542.3^{+113.69}_{-121.03}$	$1820.89^{+97.89}_{-106.98}$	$5456.42^{+158.42}_{-189.34}$	$5793.88^{+186.56}_{-208.85}$	$0.51^{+0.03}_{-0.03}$	22.8	42.0
SF 230509	0	54	1.0	2023-05-09 03:51:46.1	$95.0^{+1.41}_{-2.24}$	4424.68±67.79	4444.67±67.71	$142477.25^{+725.5}_{-1058.97}$	$46808.23^{+252.55}_{-309.0}$	$189285.47^{+847.66}_{-1274.34}$	$188692.0^{+847.61}_{-1268.8}$	$0.33^{+0.0}_{-0.0}$	65.6	420.0
SF 230523	0	54	1.0	2023-05-23 12:13:31.0	$121.0^{+5.1}_{-5.1}$	109.03±15.46	110.19±15.0	$3141.11^{+108.26}_{-126.24}$	$465.09^{+102.13}_{-91.69}$	$3606.2^{+160.24}_{-156.88}$	$3785.33^{+162.28}_{-163.96}$	$0.15^{+0.03}_{-0.03}$	7.3	27.2
SF 230615	1	56	1.0	2023-06-15 03:16:27.3	$40.0^{+3.16}_{-3.16}$	75.3±17.32	73.74±14.8	$510.14^{+62.38}_{-56.91}$	$108.3^{+67.22}_{-61.58}$	$650.08^{+96.43}_{-81.81}$	$644.09^{+106.68}_{-99.12}$	$0.21^{+0.13}_{-0.12}$	5.0	8.1
SF 230707	1	56	1.0	2023-07-07 06:27:32.3	$103.0^{+3.16}_{-3.16}$	731.54±29.66	726.81±29.33	$13584.35^{+173.87}_{-191.19}$	$1953.73^{+96.17}_{-100.97}$	$15367.81^{+200.33}_{-235.88}$	$15746.66^{+206.19}_{-249.57}$	$0.14^{+0.01}_{-0.01}$	24.8	90.3
SF 230711	1	54	1.0	2023-07-11 04:02:35.2	$54.0^{+1.41}_{-23.02}$	141.59±17.64	140.86±17.03	$787.47^{+72.61}_{-112.75}$	$34.35^{+73.57}_{-62.23}$	$821.82^{+97.78}_{-106.5}$	$870.28^{+102.06}_{-132.25}$	$0.04^{+0.09}_{-0.08}$	8.3	8.6
SF 230715	0	54	1.0	2023-07-15 07:30:09.3	$59.0^{+1.41}_{-1.41}$	406.98±25.51	412.27±24.21	$11631.23^{+166.24}_{-175.92}$	$1778.5^{+89.06}_{-92.41}$	$13409.74^{+195.16}_{-205.39}$	$13215.9^{+208.39}_{-211.58}$	$0.15^{+0.01}_{-0.01}$	17.0	87.0
SF 230902	0	54	1.0	2023-09-02 06:54:56.5	$70.0^{+23.02}_{-59.01}$	90.12±15.46	94.57±15.03	$1346.32^{+393.91}_{-701.42}$	$-49.49^{+95.88}_{-61.2}$	$1296.83^{+393.42}_{-634.54}$	$1263.12^{+360.81}_{-606.35}$	$-0.04^{+-0.07}_{--0.05}$	6.3	12.5
SF 230906	0	54	1.0	2023-09-06 14:02:17.4	$9.0^{+1.0}_{-1.41}$	129.39±19.62	129.09±17.69	$605.62^{+37.26}_{-52.82}$	$55.11^{+31.05}_{-31.62}$	$660.73^{+47.95}_{-67.06}$	$689.04^{+54.53}_{-78.08}$	$0.09^{+0.05}_{-0.05}$	7.3	13.8
SF 230916	1	56	1.0	2023-09-16 15:50:43.1	$11.0^{+2.24}_{-1.41}$	145.83±19.49	134.12±17.29	$512.01^{+45.25}_{-38.47}$	$238.16^{+41.07}_{-43.02}$	$767.41^{+73.64}_{-64.73}$	$757.33^{+75.69}_{-68.98}$	$0.47^{+0.09}_{-0.09}$	7.8	15.1
SF 231001	0	54	1.0	2023-10-01 03:23:27.3	$16.0^{+2.24}_{-1.0}$	816.37±31.06	806.5±30.63	$3593.63^{+110.63}_{-80.58}$	$695.0^{+40.37}_{-40.23}$	$4288.64^{+114.22}_{-97.08}$	$4292.96^{+117.34}_{-105.61}$	$0.19^{+0.01}_{-0.01}$	26.3	53.6
SF 231102	0	54	1.0	2023-11-02 12:22:10.8	$32.0^{+7.07}_{-2.24}$	199.91±20.88	190.43±19.13	$1347.24^{+85.19}_{-100.05}$	$464.36^{+60.58}_{-62.08}$	$1811.6^{+111.01}_{-129.64}$	$1816.77^{+128.01}_{-129.9}$	$0.34^{+0.05}_{-0.05}$	10.0	21.0
SF 231105	0	54	1.0	2023-11-05 21:33:28.0	$45.0^{+3.16}_{-6.08}$	88.1±14.32	82.04±13.56	$817.67^{+76.18}_{-77.68}$	$154.25^{+52.59}_{-48.29}$	$971.91^{+94.61}_{-89.26}$	$967.04^{+89.18}_{-94.35}$	$0.19^{+0.07}_{-0.06}$	6.0	13.1
SF 231204	0	54	1.0	2023-12-04 01:24:55.2	$9.0^{+1.41}_{-1.41}$	36.46±12.57	26.38±11.58	$104.29^{+26.65}_{-40.3}$	$31.86^{+21.62}_{-30.74}$	$139.04^{+34.54}_{-43.05}$	$166.05^{+35.51}_{-49.4}$	$0.31^{+0.22}_{-0.32}$	2.3	4.2
SF 231206	0	54	1.0	2023-12-06 05:38:46.4	$39.0^{+2.24}_{-3.16}$	44.75±13.08	38.3±12.12	$548.43^{+59.85}_{-68.44}$	$66.97^{+42.13}_{-42.21}$	$615.4^{+75.4}_{-82.22}$	$624.0^{+77.73}_{-88.2}$	$0.12^{+0.08}_{-0.08}$	3.2	8.8

Table 4.3 (*continued*): Solar flares detected by GRBAlpha.

name	channel	cutoff	t_{exp}	peak time (UTC)	T_{90}	P in 0–255 ADC	P in 0–127 ADC	S in 0–63 ADC	S in 64-127 ADC	S in 0–127 ADC	S in 0–255 ADC	HR	SNR_p	$SNR_{T_{90}}$
		ADC ch.	s	UTC	s	cnt/s	cnt/s	cnt	cnt	cnt	cnt	–	–	–
SF 231214	0	54	1.0	2023-12-14 17:06:14.5	$56.0^{+1.41}_{-1.41}$	219.31±22.89	222.58±21.73	$2200.95^{+101.31}_{-105.56}$	$1441.08^{+94.24}_{-95.14}$	$4022.21^{+144.18}_{-151.03}$	$4132.3^{+153.32}_{-163.35}$	$0.65^{+0.05}_{-0.05}$	10.2	30.0
SF 231215	0	54	1.0	2023-12-15 07:56:38.6	$112.0^{+3.16}_{-2.24}$	284.89±22.34	283.23±21.86	$13637.87^{+218.87}_{-196.12}$	$3025.42^{+100.58}_{-98.15}$	$16663.3^{+254.73}_{-219.08}$	$16553.55^{+257.54}_{-224.47}$	$0.22^{+0.01}_{-0.01}$	13.0	84.6
SF 231226	0	54	1.0	2023-12-26 03:13:01.1	$27.0^{+1.41}_{-1.41}$	582.38±26.65	573.87±26.19	$5095.0^{+97.62}_{-97.08}$	$1139.62^{+52.39}_{-55.91}$	$6179.24^{+118.27}_{-122.74}$	$6154.75^{+122.52}_{-127.22}$	$0.22^{+0.01}_{-0.01}$	21.9	64.4
SF 231231	0	54	1.0	2023-12-31 08:14:45.4	$48.0^{+5.1}_{-8.06}$	88.42±14.76	94.39±14.11	$1235.04^{+80.01}_{-123.7}$	$-39.55^{+44.66}_{-45.7}$	$1210.57^{+93.72}_{-131.7}$	$1174.01^{+95.54}_{-139.72}$	$-0.03^{+-0.04}_{--0.04}$	6.7	15.4
SF 240129	0	54	1.0	2024-01-29 04:17:35.9	$267.0^{+18.03}_{-5.1}$	330.38±22.14	324.04±21.49	$34631.99^{+1493.46}_{-435.54}$	$13675.23^{+566.69}_{-229.16}$	$48307.22^{+2061.15}_{-600.68}$	$48621.65^{+2080.81}_{-612.9}$	$0.39^{+0.02}_{-0.01}$	15.1	167.0
SF 240204	0	54	1.0	2024-02-04 18:25:56.7	$39.0^{+2.24}_{-2.24}$	219.52±18.87	214.48±18.28	$4716.72^{+107.88}_{-131.14}$	$355.01^{+49.64}_{-50.07}$	$5034.09^{+126.97}_{-148.78}$	$4955.95^{+130.13}_{-147.94}$	$0.08^{+0.01}_{-0.01}$	11.7	51.1
SF 240207	0	54	1.0	2024-02-07 03:24:52.9	$520.0^{+6.08}_{-6.08}$	78.86±15.23	87.7±14.53	$16181.22^{+279.87}_{-276.15}$	$3239.81^{+165.47}_{-173.52}$	$17068.26^{+329.29}_{-337.41}$	$12719.56^{+322.75}_{-320.15}$	$0.2^{+0.01}_{-0.01}$	6.0	61.2
SF 240210	0	54	0.5	2024-02-10 02:12:32.0	$8.0^{+12.01}_{-4.53}$	64.14±21.91	56.4±19.49	$87.9^{+31.38}_{-26.59}$	$35.67^{+27.2}_{-40.16}$	$123.58^{+37.54}_{-57.42}$	$111.18^{+42.22}_{-55.82}$	$0.41^{+0.34}_{-0.47}$	2.9	3.6
SF 240211	0	54	0.5	2024-02-11 22:41:14.1	$39.0^{+5.02}_{-5.52}$	126.95±22.54	125.59±22.0	$1427.9^{+65.17}_{-125.95}$	$148.27^{+56.11}_{-43.94}$	$1582.0^{+83.02}_{-130.42}$	$1717.74^{+98.15}_{-161.01}$	$0.1^{+0.04}_{-0.03}$	5.7	20.2
SF 240216	0	54	0.5	2024-02-16 06:51:18.9	$322.5^{+3.54}_{-5.02}$	1881.3±63.21	1874.58±62.9	$104140.62^{+560.91}_{-639.7}$	$29112.91^{+229.8}_{-248.55}$	$133607.15^{+675.26}_{-771.72}$	$132971.95^{+657.05}_{-753.47}$	$0.28^{+0.0}_{-0.0}$	29.8	324.9
SF 240222a	0	54	0.5	2024-02-22 06:29:17.9	$528.0^{+4.53}_{-6.52}$	360.93±31.05	362.55±30.59	$13835.78^{+247.62}_{-233.78}$	$1010.07^{+160.14}_{-156.92}$	$14748.87^{+304.56}_{-282.53}$	$15061.46^{+311.44}_{-297.28}$	$0.07^{+0.01}_{-0.01}$	11.8	55.6
SF 240222b	0	54	0.5	2024-02-22 20:40:39.9	$533.0^{+6.02}_{-7.52}$	67.21±19.49	61.65±18.44	$2770.19^{+198.28}_{-196.69}$	$883.71^{+166.73}_{-167.83}$	$2354.37^{+262.43}_{-260.74}$	$3355.0^{+275.31}_{-277.26}$	$0.32^{+0.06}_{-0.06}$	3.3	9.5
SF 240222c	0	54	0.5	2024-02-22 22:29:09.4	$402.5^{+0.5}_{-0.71}$	19082.34±196.06	19077.87±196.0	$3574458.25^{+1898.72}_{-2697.51}$	$713257.69^{+857.89}_{-860.65}$	$4287715.94^{+2083.53}_{-2877.71}$	$4290318.13^{+2085.43}_{-2880.87}$	$0.2^{+0.0}_{-0.0}$	97.3	2057.9
SF 240310	0	54	0.5	2024-03-10 12:09:18.9	$229.5^{+5.52}_{-2.55}$	2579.87±75.66	2629.27±75.21	$56557.2^{+570.7}_{-494.15}$	$24339.87^{+308.93}_{-305.91}$	$80897.08^{+803.26}_{-719.87}$	$71804.87^{+693.85}_{-681.01}$	$0.43^{+0.01}_{-0.01}$	35.0	232.2
SF 240311	0	54	0.5	2024-03-11 08:45:21.5	$48.5^{+2.55}_{-2.55}$	94.56±20.78	93.15±20.0	$943.27^{+79.19}_{-93.16}$	$292.26^{+54.46}_{-50.84}$	$1244.77^{+103.61}_{-103.37}$	$1201.34^{+101.84}_{-106.27}$	$0.31^{+0.06}_{-0.06}$	4.7	15.5
SF 240318	0	54	0.5	2024-03-18 03:27:34.2	$165.0^{+2.06}_{-3.04}$	98.5±21.82	99.68±20.88	$4844.44^{+134.36}_{-141.18}$	$216.75^{+95.22}_{-95.08}$	$4865.29^{+167.01}_{-173.81}$	$4727.1^{+174.37}_{-183.14}$	$0.04^{+0.02}_{-0.02}$	4.8	31.2
SF 240324	0	54	0.5	2024-03-24 06:05:51.4	$31.0^{+2.55}_{-2.55}$	240.6±27.2	241.6±26.68	$2085.77^{+68.16}_{-80.06}$	$462.09^{+45.84}_{-59.58}$	$2547.86^{+81.88}_{-108.59}$	$2522.89^{+83.71}_{-113.17}$	$0.22^{+0.02}_{-0.03}$	9.1	32.6
SF 240326	0	54	0.5	2024-03-26 02:26:02.0	$15.5^{+1.58}_{-2.06}$	148.53±24.25	150.78±23.41	$1055.97^{+69.0}_{-65.13}$	$63.12^{+30.81}_{-30.86}$	$1119.09^{+71.71}_{-73.85}$	$1095.25^{+73.9}_{-76.02}$	$0.06^{+0.03}_{-0.03}$	6.4	20.3
SF 240411	0	54	0.5	2024-04-11 03:35:07.9	$17.5^{+2.06}_{-1.58}$	146.39±25.92	126.52±22.98	$696.93^{+45.77}_{-63.85}$	$329.87^{+40.47}_{-40.12}$	$1026.8^{+61.55}_{-83.36}$	$1046.89^{+67.55}_{-82.5}$	$0.47^{+0.07}_{-0.07}$	5.5	17.5
SF 240425	0	54	0.5	2024-04-25 17:11:40.4	$25.5^{+4.03}_{-7.52}$	89.62±21.35	91.62±20.59	$131.3^{+88.93}_{-40.92}$	$89.08^{+40.59}_{-54.5}$	$219.46^{+80.83}_{-59.18}$	$223.36^{+77.62}_{-62.58}$	$0.68^{+0.55}_{-0.47}$	4.4	3.8

Table 4.4: Flashes from soft gamma repeaters and X-ray binaries detected by GRBAlpha. Columns are: event name, GRBAlpha read-out channel which acquired the data, low-energy cutoff, exposure time t_{exp}, peak time of the detection, T_{90} duration, peak flux P in two different energy bands, fluence S in four different energy bands, hardness ratio HR between the two lowest energy bands, SNR at the peak time and during the T_{90} in the 0–127 ADC band, and the GCN Circular number in which the detection was announced. Explanation of the energy bands can be found in Sec. 3.1. GCN Circulars which are marked with an asterix were prepared by the author of this work.

name	channel	cutoff	t_{exp}	peak time (UTC)	T_{90}	P in 0–255 ADC	P in 0–127 ADC	S in 0–63 ADC	S in 64-127 ADC	S in 0–127 ADC	S in 0–255 ADC	HR	SNR_{p}	$SNR_{\mathrm{T_{90}}}$	GCN no.
		ADC ch.	s	UTC	s	cnt/s	cnt/s	cnt	cnt	cnt	cnt	–	–	–	
SGR 1935+2154	0	54	4.0	2022-10-14 07:12:27.7	$4.0^{+4.0}_{-4.0}$	62.64±9.29	62.06±7.83	$184.84^{+13.6}_{-13.6}$	$63.4^{+7.96}_{-7.96}$	$248.24^{+15.76}_{-15.76}$	$250.56^{+15.83}_{-15.83}$	$0.34^{+0.05}_{-0.05}$	7.9	15.8	32794*
SGR 1935+2154	0	54	4.0	2022-10-14 17:27:39.7	$16.0^{+4.0}_{-4.0}$	265.32±11.26	265.11±10.16	$1731.05^{+53.39}_{-53.39}$	$430.12^{+40.94}_{-40.94}$	$2161.17^{+67.28}_{-67.28}$	$2204.4^{+77.89}_{-77.89}$	$0.25^{+0.02}_{-0.02}$	26.1	32.1	32814
LS V +44 17 / RX J0440.9+4431	0	54	1.0	2023-02-11 17:36:18.8	$13.0^{+1.41}_{-2.24}$	44.49±13.27	38.12±12.08	$187.69^{+34.42}_{-39.06}$	$42.69^{+25.68}_{-25.69}$	$233.84^{+42.34}_{-47.18}$	$242.84^{+45.89}_{-55.43}$	$0.23^{+0.14}_{-0.14}$	3.2	5.8	33320*

Table 4.5: GRBs detected by VZLUSAT-2. Columns are: GRB name, VZLUSAT-2 read-out channel which acquired the data, low-energy cutoff, exposure time t_{exp}, peak time of the detection, T_{90} duration, peak flux P in two different energy bands, fluence S in four different energy bands, hardness ratio HR between the two lowest energy bands, SNR at the peak time and during the T_{90} in the 0–127 ADC band, and the GCN Circular number in which the detection was announced. Explanation of the energy bands can be found in Sec. 3.1. GCN Circulars which are marked with an asterix were prepared by the author of this work.

name	channel	cutoff	t_{exp}	peak time (UTC)	T_{90}	P in 0–255 ADC	P in 0–127 ADC	S in 0–63 ADC	S in 64-127 ADC	S in 0–127 ADC	S in 0–255 ADC	HR	SNR_p	$SNR_{T_{90}}$	GCN no.
		ADC ch.	s	UTC	s	cnt/s	cnt/s	cnt	cnt	cnt	cnt	–	–	–	
GRB 220320A	2	45	15.0	2022-03-20 04:39:55.5	$15.0^{+15.0}_{-15.0}$	180.93±5.99	178.11±5.17	$1291.24^{+58.15}_{-58.15}$	$1380.39^{+51.29}_{-51.29}$	$2671.62^{+77.54}_{-77.54}$	$2713.92^{+89.84}_{-89.84}$	$1.07^{+0.06}_{-0.06}$	34.5	34.5	31803
GRB 220423A	0	45	1.0	2022-04-23 14:14:14.5	$14.0^{+14.04}_{-2.24}$	320.39±22.23	299.47±21.1	$717.79^{+78.93}_{-95.19}$	$904.48^{+87.92}_{-110.7}$	$1622.26^{+160.36}_{-196.4}$	$1680.52^{+191.84}_{-197.84}$	$1.26^{+0.18}_{-0.23}$	14.2	26.8	31965
GRB 220423A	2	45	1.0	2022-04-23 14:14:14.5	$29.0^{+14.04}_{-14.04}$	324.86±22.09	322.65±21.4	$768.36^{+78.3}_{-93.17}$	$1097.83^{+75.75}_{-72.76}$	$1866.2^{+131.08}_{-150.89}$	$1926.96^{+135.46}_{-133.19}$	$1.43^{+0.18}_{-0.2}$	15.1	24.6	31965
GRB 220608B	2	45	1.0	2022-06-08 07:36:39.5	$22.0^{+5.1}_{-3.16}$	72.35±15.43	67.51±14.73	$302.6^{+53.63}_{-74.1}$	$184.0^{+33.5}_{-47.42}$	$490.03^{+61.94}_{-97.14}$	$511.83^{+64.71}_{-98.92}$	$0.61^{+0.15}_{-0.22}$	4.6	8.0	32196
GRB 220719A	2	45	1.0	2022-07-19 19:09:43.5	$7.0^{+1.41}_{-1.41}$	98.64±18.95	95.96±18.41	$212.47^{+41.78}_{-47.15}$	$75.45^{+23.88}_{-19.74}$	$287.92^{+51.24}_{-51.8}$	$299.77^{+56.06}_{-57.29}$	$0.36^{+0.13}_{-0.12}$	5.2	6.5	32463
GRB 220912A	2	48	1.0	2022-09-12 00:50:23.5	$32.0^{+5.1}_{-3.16}$	102.31±15.17	99.56±14.53	$768.55^{+65.48}_{-81.8}$	$750.99^{+53.25}_{-68.8}$	$1519.54^{+89.85}_{-113.16}$	$1581.8^{+89.94}_{-115.49}$	$0.98^{+0.11}_{-0.14}$	6.9	21.3	32624
GRB 221028A	2	48	1.0	2022-10-28 13:16:26.5	$43.0^{+2.24}_{-3.16}$	71.51±15.03	64.91±13.96	$359.49^{+66.66}_{-62.13}$	$327.4^{+71.73}_{-48.75}$	$686.9^{+110.14}_{-79.02}$	$727.43^{+118.23}_{-85.26}$	$0.91^{+0.26}_{-0.21}$	4.6	8.7	32904
GRB 221028A	0	48	1.0	2022-10-28 13:16:26.5	$22.0^{+3.16}_{-2.24}$	87.23±15.49	89.99±14.73	$283.08^{+59.91}_{-56.18}$	$228.97^{+40.21}_{-40.08}$	$527.33^{+81.65}_{-79.05}$	$575.18^{+92.4}_{-97.71}$	$0.81^{+0.22}_{-0.21}$	6.1	9.2	32904
GRB 221120A	2	48	1.0	2022-11-20 21:29:27.5	$2.0^{+2.24}_{-1.41}$	34.73±12.45	39.2±12.0	$45.22^{+21.37}_{-27.65}$	$28.07^{+10.1}_{-18.12}$	$73.29^{+19.94}_{-42.66}$	$68.35^{+19.66}_{-38.93}$	$0.62^{+0.37}_{-0.55}$	3.3	4.4	32982
GRB 221202B	2	48	1.0	2022-12-02 21:42:03.5	$18.0^{+3.16}_{-3.16}$	77.17±20.25	70.25±17.64	$173.19^{+58.29}_{-60.84}$	$214.31^{+47.2}_{-70.11}$	$375.09^{+78.58}_{-101.35}$	$346.51^{+90.33}_{-103.56}$	$1.24^{+0.5}_{-0.59}$	4.0	5.5	33019
GRB 221216A	2	48	1.0	2022-12-16 11:22:41.5	$24.0^{+6.08}_{-4.12}$	29.35±12.53	28.46±11.87	$84.69^{+44.0}_{-49.54}$	$84.84^{+35.89}_{-32.34}$	$169.53^{+54.63}_{-60.48}$	$172.42^{+57.12}_{-67.9}$	$1.0^{+0.67}_{-0.7}$	2.4	3.2	33088
GRB 230114A	2	48	1.0	2023-01-14 16:59:17.5	$7.0^{+9.06}_{-3.16}$	56.58±14.93	49.33±13.53	$110.06^{+39.44}_{-48.88}$	$119.48^{+67.57}_{-50.62}$	$229.54^{+94.83}_{-95.11}$	$249.82^{+64.01}_{-107.88}$	$1.09^{+0.73}_{-0.67}$	3.6	6.7	33170
GRB 230114B	2	48	1.0	2023-01-14 20:40:54.5	$1.0^{+1.0}_{-1.0}$	85.26±18.06	72.76±15.0	$39.96^{+6.32}_{-6.32}$	$32.8^{+5.73}_{-5.73}$	$72.76^{+8.53}_{-8.53}$	$85.26^{+9.23}_{-9.23}$	$0.82^{+0.19}_{-0.19}$	4.8	8.5	33218
GRB 230126A	0	48	1.0	2023-01-26 18:21:10.5	$15.0^{+1.0}_{-1.41}$	45.16±14.18	38.86±12.69	$174.99^{+39.54}_{-39.03}$	$50.03^{+24.08}_{-33.3}$	$230.59^{+45.78}_{-51.77}$	$247.89^{+51.66}_{-56.98}$	$0.29^{+0.15}_{-0.2}$	3.1	5.0	33246*
GRB 230307A	0	48	1.0	2023-03-07 15:44:11.5	$29.0^{+1.41}_{-1.0}$	5194.04±73.2	4870.29±70.71	$23130.6^{+202.16}_{-159.84}$	$27026.12^{+181.54}_{-168.31}$	$50156.72^{+301.11}_{-232.11}$	$52425.37^{+306.77}_{-238.97}$	$1.17^{+0.01}_{-0.01}$	68.9	216.1	33424
GRB 230307A	2	48	1.0	2023-03-07 15:44:11.5	$35.0^{+1.0}_{-1.41}$	4407.22±67.62	4056.61±64.73	$19248.11^{+148.79}_{-180.24}$	$28693.42^{+174.45}_{-219.49}$	$47931.02^{+229.28}_{-328.0}$	$50740.54^{+237.61}_{-336.06}$	$1.49^{+0.01}_{-0.02}$	62.7	209.0	33424
GRB 230405B	2	48	1.0	2023-04-05 19:58:04.5	$4.0^{+1.0}_{-1.41}$	462.53±24.98	458.71±24.39	$469.73^{+28.67}_{-98.38}$	$494.8^{+26.23}_{-82.07}$	$964.53^{+38.86}_{-176.21}$	$971.71^{+40.22}_{-176.41}$	$1.05^{+0.09}_{-0.28}$	18.8	24.8	33590*
GRB 230409D	2	48	1.0	2023-04-09 15:01:08.5	$18.0^{+7.07}_{-6.08}$	123.82±16.7	117.27±15.72	$165.19^{+42.14}_{-55.86}$	$418.15^{+35.5}_{-63.87}$	$583.34^{+54.72}_{-106.1}$	$676.29^{+59.1}_{-113.74}$	$2.53^{+0.68}_{-0.94}$	7.5	10.8	33605*
GRB 230409D	0	48	1.0	2023-04-09 15:01:08.5	$19.0^{+2.24}_{-3.16}$	329.89±22.0	323.94±21.26	$857.99^{+53.48}_{-54.73}$	$916.0^{+44.37}_{-53.75}$	$1774.0^{+71.19}_{-86.26}$	$1794.33^{+73.71}_{-83.04}$	$1.07^{+0.08}_{-0.09}$	15.2	27.3	33605*
GRB 230410B	2	48	1.0	2023-04-10 04:31:18.5	$1.0^{+1.0}_{-1.0}$	162.36±17.97	146.97±16.79	$57.78^{+7.6}_{-7.6}$	$89.19^{+9.44}_{-9.44}$	$146.97^{+12.12}_{-12.12}$	$162.36^{+12.74}_{-12.74}$	$1.54^{+0.26}_{-0.26}$	8.8	12.1	33606*
GRB 230426A	2	48	1.0	2023-04-26 20:29:21.5	$24.0^{+1.41}_{-1.41}$	931.52±32.76	930.69±32.47	$4842.05^{+86.65}_{-108.22}$	$2072.17^{+61.8}_{-62.33}$	$6900.58^{+112.78}_{-140.23}$	$6948.37^{+116.11}_{-140.0}$	$0.43^{+0.01}_{-0.02}$	28.7	69.5	33702*
GRB 230426A	0	48	1.0	2023-04-26 20:29:20.5	$32.0^{+4.12}_{-4.12}$	167.36±17.44	172.3±17.06	$936.29^{+82.66}_{-62.51}$	$388.33^{+37.76}_{-40.49}$	$1324.62^{+90.13}_{-77.53}$	$1340.33^{+95.52}_{-79.88}$	$0.41^{+0.05}_{-0.05}$	10.1	18.5	33702*
GRB 230518B	2	48	1.0	2023-05-18 02:18:17.5	$131.0^{+6.08}_{-39.01}$	223.04±21.17	204.34±19.18	$2985.47^{+211.65}_{-125.23}$	$2277.36^{+129.71}_{-138.97}$	$5262.83^{+278.35}_{-190.37}$	$5459.95^{+314.95}_{-191.8}$	$0.76^{+0.07}_{-0.06}$	10.7	32.9	33847*
GRB 230521A	2	48	1.0	2023-05-21 18:52:10.5	$38.0^{+3.16}_{-2.24}$	157.34±16.97	155.24±16.37	$662.72^{+65.35}_{-81.19}$	$408.77^{+55.63}_{-55.27}$	$1095.28^{+95.55}_{-116.65}$	$1098.84^{+96.35}_{-129.8}$	$0.62^{+0.1}_{-0.11}$	9.5	14.9	33906*
GRB 230521A	0	48	1.0	2023-05-21 18:52:10.5	$36.0^{+14.04}_{-4.12}$	191.2±17.97	189.18±17.46	$268.81^{+76.16}_{-70.0}$	$404.23^{+61.3}_{-63.93}$	$673.05^{+123.34}_{-113.95}$	$700.76^{+146.87}_{-125.47}$	$1.5^{+0.48}_{-0.46}$	10.8	9.6	33906*
GRB 230522A	0	48	1.0	2023-05-22 03:34:43.5	$11.0^{+1.41}_{-1.41}$	299.58±21.54	279.16±20.4	$751.89^{+44.26}_{-62.72}$	$907.59^{+38.26}_{-68.47}$	$1659.48^{+60.36}_{-118.23}$	$1712.23^{+60.91}_{-122.59}$	$1.21^{+0.09}_{-0.14}$	13.7	29.5	33905*
GRB 230522A	2	48	1.0	2023-05-22 03:34:43.5	$10.0^{+8.06}_{-3.16}$	70.95±15.3	58.12±13.86	$130.64^{+32.58}_{-41.22}$	$156.7^{+88.54}_{-27.69}$	$281.43^{+82.73}_{-50.25}$	$302.76^{+100.95}_{-50.3}$	$1.2^{+0.74}_{-0.43}$	4.2	7.0	33905*
GRB 230626A	2	48	1.0	2023-06-26 14:30:32.5	$13.0^{+2.24}_{-1.41}$	305.86±24.12	315.55±22.52	$777.25^{+86.78}_{-95.66}$	$618.3^{+46.31}_{-59.84}$	$1395.55^{+98.75}_{-142.26}$	$1320.87^{+97.2}_{-145.34}$	$0.8^{+0.11}_{-0.12}$	14.0	22.4	34143*

Table 4.5 (*continued*): GRBs detected by VZLUSAT-2.

name	channel	cutoff	t_{exp}	peak time (UTC)	T_{90}	P in 0–255 ADC	P in 0–127 ADC	S in 0–63 ADC	S in 64-127 ADC	S in 0–127 ADC	S in 0–255 ADC	HR	SNR_p	$SNR_{T_{90}}$	GCN no.
		ADC ch.	s	UTC	s	cnt/s	cnt/s	cnt	cnt	cnt	cnt	–	–	–	
GRB 230818B	2	48	1.0	2023-08-18 10:13:04.5	$30.0^{+2.24}_{-2.24}$	95.6±18.17	90.48±16.0	$645.35^{+57.02}_{-87.34}$	$512.83^{+53.93}_{-55.84}$	$1163.03^{+78.42}_{-113.44}$	$1060.87^{+89.94}_{-121.3}$	$0.79^{+0.11}_{-0.14}$	5.7	14.9	34525*
GRB 230818B	0	48	1.0	2023-08-18 10:12:53.5	$35.0^{+2.24}_{-1.41}$	97.31±18.25	90.96±16.03	$672.81^{+69.84}_{-72.19}$	$467.12^{+62.06}_{-54.33}$	$1139.93^{+97.17}_{-87.03}$	$1232.24^{+119.95}_{-99.59}$	$0.69^{+0.12}_{-0.11}$	5.7	13.7	34525*
GRB 230826A	2	48	1.0	2023-08-26 19:32:48.5	$20.0^{+8.06}_{-3.16}$	94.16±15.43	93.86±14.9	$696.62^{+51.74}_{-86.76}$	$325.83^{+32.85}_{-53.73}$	$1023.51^{+61.87}_{-122.57}$	$1017.33^{+65.39}_{-122.81}$	$0.47^{+0.06}_{-0.1}$	6.3	17.1	34586*
GRB 230826A	0	48	1.0	2023-08-26 19:32:49.5	$17.0^{+9.06}_{-4.12}$	54.08±13.67	54.11±13.08	$331.61^{+42.31}_{-72.82}$	$181.25^{+29.35}_{-43.49}$	$512.66^{+52.24}_{-105.95}$	$518.39^{+57.97}_{-115.16}$	$0.55^{+0.11}_{-0.18}$	4.1	10.3	34586*
GRB 230827B	2	48	1.0	2023-08-27 06:08:33.5	$13.0^{+2.24}_{-7.07}$	145.75±20.12	131.98±18.06	$290.0^{+56.86}_{-101.8}$	$353.51^{+44.97}_{-90.97}$	$643.51^{+84.8}_{-184.44}$	$701.76^{+104.23}_{-206.88}$	$1.22^{+0.28}_{-0.53}$	7.3	11.4	34585*
GRB 230827B	0	48	1.0	2023-08-27 06:08:33.5	$20.0^{+1.41}_{-1.41}$	175.88±24.06	178.26±22.69	$434.45^{+82.01}_{-75.69}$	$422.07^{+52.35}_{-47.22}$	$856.51^{+105.59}_{-91.21}$	$860.82^{+108.08}_{-100.89}$	$0.97^{+0.22}_{-0.2}$	7.9	9.8	34585*
GRB 230827A	0	48	1.0	2023-08-27 18:18:09.5	$83.0^{+4.12}_{-3.16}$	53.11±15.23	44.67±14.0	$834.05^{+100.03}_{-104.02}$	$145.37^{+60.31}_{-59.67}$	$979.73^{+116.87}_{-119.57}$	$1047.34^{+125.45}_{-128.54}$	$0.17^{+0.08}_{-0.07}$	3.2	8.5	34588*
GRB 230827A	2	48	1.0	2023-08-27 18:18:18.5	$51.0^{+4.12}_{-4.12}$	187.67±19.03	185.83±18.3	$1184.82^{+107.81}_{-87.11}$	$1445.0^{+121.13}_{-73.46}$	$2629.82^{+210.32}_{-132.19}$	$2657.57^{+212.87}_{-140.26}$	$1.22^{+0.15}_{-0.11}$	10.2	26.0	34588*
GRB 230911B	2	48	1.0	2023-09-11 04:25:50.5	$15.0^{+2.24}_{-2.24}$	116.36±19.52	117.49±18.73	$315.0^{+60.68}_{-54.8}$	$274.38^{+36.32}_{-36.03}$	$563.86^{+69.6}_{-66.8}$	$590.95^{+74.72}_{-80.12}$	$0.87^{+0.2}_{-0.19}$	6.3	8.8	34664*
GRB 231018A	2	48	1.0	2023-10-18 12:31:10.5	$31.0^{+3.16}_{-27.02}$	347.45±25.2	340.75±23.75	$435.75^{+95.68}_{-257.43}$	$457.37^{+58.59}_{-282.45}$	$826.01^{+127.06}_{-474.46}$	$876.2^{+148.36}_{-503.09}$	$1.05^{+0.27}_{-0.9}$	14.3	9.6	34865*
GRB 231019A	0	48	1.0	2023-10-19 17:10:01.5	$9.0^{+1.41}_{-1.41}$	63.18±14.59	69.75±14.35	$131.81^{+33.76}_{-36.05}$	$82.37^{+21.79}_{-21.0}$	$214.62^{+41.13}_{-45.16}$	$207.77^{+43.05}_{-44.21}$	$0.62^{+0.23}_{-0.23}$	4.9	5.7	34866*
GRB 231019A	2	48	1.0	2023-10-19 17:10:01.5	$6.0^{+3.16}_{-2.24}$	53.61±13.75	48.65±13.08	$81.58^{+28.8}_{-29.85}$	$39.73^{+17.49}_{-17.36}$	$121.31^{+37.47}_{-37.47}$	$124.06^{+34.79}_{-37.89}$	$0.49^{+0.27}_{-0.28}$	3.7	4.1	34866*
GRB 231028B	0	48	1.0	2023-10-28 22:25:58.5	$46.0^{+4.12}_{-4.12}$	67.71±14.73	74.82±14.35	$661.33^{+79.07}_{-86.72}$	$567.58^{+50.73}_{-49.37}$	$1170.32^{+100.97}_{-105.37}$	$1154.4^{+107.46}_{-103.62}$	$0.86^{+0.13}_{-0.14}$	5.2	13.7	34922*
GRB 231028B	2	48	1.0	2023-10-28 22:26:31.5	$38.0^{+7.07}_{-5.1}$	49.54±13.78	47.1±12.92	$348.69^{+66.1}_{-65.52}$	$209.81^{+48.17}_{-50.87}$	$573.11^{+89.32}_{-92.41}$	$541.93^{+91.41}_{-93.19}$	$0.6^{+0.18}_{-0.18}$	3.6	8.0	34922*
GRB 231104A	2	48	1.0	2023-11-04 01:47:39.5	$27.0^{+5.1}_{-3.16}$	443.43±24.6	428.92±23.71	$702.69^{+53.53}_{-71.53}$	$813.59^{+48.01}_{-56.22}$	$1516.28^{+71.75}_{-108.07}$	$1603.41^{+77.46}_{-103.62}$	$1.16^{+0.11}_{-0.14}$	18.1	21.3	35008*
GRB 231118A	2	48	1.0	2023-11-18 17:16:34.5	$8.0^{+3.16}_{-4.12}$	74.11±15.26	68.37±14.66	$137.55^{+44.15}_{-78.84}$	$77.43^{+18.72}_{-35.68}$	$198.44^{+37.06}_{-101.28}$	$217.21^{+44.72}_{-110.76}$	$0.56^{+0.23}_{-0.41}$	4.7	5.4	35143*
GRB 231128A	2	48	1.0	2023-11-28 11:44:15.5	$24.0^{+2.24}_{-1.41}$	51.93±13.56	53.67±13.04	$442.84^{+50.29}_{-55.66}$	$186.61^{+33.52}_{-32.76}$	$618.88^{+62.19}_{-67.16}$	$608.32^{+66.24}_{-70.18}$	$0.42^{+0.09}_{-0.09}$	4.1	10.6	35246*
GRB 231129A	2	48	1.0	2023-11-29 05:06:01.5	$156.0^{+4.12}_{-5.1}$	81.11±14.11	79.49±13.53	$4586.96^{+154.92}_{-187.39}$	$1393.51^{+87.07}_{-90.46}$	$5980.47^{+195.57}_{-233.52}$	$5632.44^{+190.03}_{-231.87}$	$0.3^{+0.02}_{-0.02}$	5.9	41.6	35248*
GRB 231204A	0	48	1.0	2023-12-04 20:00:07.5	$5.0^{+1.41}_{-1.0}$	49.12±15.13	47.51±14.32	$44.47^{+27.57}_{-27.48}$	$94.5^{+16.89}_{-18.06}$	$135.54^{+30.38}_{-31.08}$	$137.08^{+32.19}_{-32.72}$	$2.13^{+1.37}_{-1.37}$	3.3	4.5	35371*
GRB 231204A	2	48	1.0	2023-12-04 20:00:07.5	$5.0^{+1.41}_{-1.0}$	85.05±16.19	87.38±15.62	$131.9^{+26.96}_{-27.06}$	$165.56^{+19.61}_{-18.79}$	$297.46^{+33.03}_{-32.86}$	$332.38^{+34.99}_{-34.87}$	$1.26^{+0.3}_{-0.29}$	5.6	9.1	35371*
GRB 231205B	2	48	1.0	2023-12-05 16:43:56.5	$25.0^{+5.1}_{-12.04}$	145.44±17.12	143.48±16.55	$173.08^{+74.08}_{-49.04}$	$439.83^{+38.15}_{-62.69}$	$586.14^{+65.98}_{-63.73}$	$616.27^{+66.62}_{-69.51}$	$2.54^{+1.11}_{-0.81}$	8.7	9.5	35372*
GRB 231205B	0	48	1.0	2023-12-05 16:43:57.5	$31.0^{+1.41}_{-1.41}$	116.28±16.52	114.55±15.97	$586.77^{+62.49}_{-64.77}$	$381.77^{+39.97}_{-49.14}$	$1029.53^{+74.25}_{-87.14}$	$1025.7^{+77.13}_{-89.71}$	$0.65^{+0.1}_{-0.11}$	7.2	14.1	35372*
GRB 240107A	0	48	1.0	2024-01-07 19:17:17.5	$42.0^{+5.1}_{-1.41}$	79.13±15.81	78.64±15.13	$588.38^{+74.74}_{-81.82}$	$231.62^{+46.28}_{-43.41}$	$819.99^{+90.06}_{-96.01}$	$871.82^{+95.66}_{-101.63}$	$0.39^{+0.09}_{-0.09}$	5.2	9.7	35544*
GRB 240112C	2	48	1.0	2024-01-12 17:37:27.5	$3.0^{+1.41}_{-1.0}$	171.38±18.44	172.35±17.86	$223.72^{+27.7}_{-23.0}$	$92.68^{+16.24}_{-15.23}$	$320.63^{+35.59}_{-27.59}$	$318.63^{+33.15}_{-28.72}$	$0.41^{+0.09}_{-0.08}$	9.6	11.6	35545*
GRB 240229A	0	48	1.0	2024-02-29 14:07:19.5	$27.0^{+2.24}_{-2.24}$	172.58±18.44	170.81±17.86	$768.77^{+72.79}_{-68.66}$	$587.25^{+39.15}_{-47.06}$	$1356.02^{+87.41}_{-92.14}$	$1357.05^{+89.94}_{-97.03}$	$0.76^{+0.09}_{-0.09}$	9.6	18.5	35872*
GRB 240229A	2	48	1.0	2024-02-29 14:06:59.5	$25.0^{+2.24}_{-2.24}$	111.91±16.4	99.45±15.43	$327.36^{+52.78}_{-63.67}$	$388.33^{+40.42}_{-71.84}$	$715.69^{+68.15}_{-116.78}$	$745.69^{+72.44}_{-123.34}$	$1.19^{+0.23}_{-0.32}$	6.4	11.1	35872*
GRB 240303B	2	48	1.0	2024-03-03 12:18:38.5	$5.0^{+1.41}_{-1.0}$	429.83±24.37	414.08±23.43	$407.19^{+102.18}_{-29.15}$	$591.54^{+179.12}_{-28.64}$	$998.72^{+277.77}_{-40.87}$	$998.36^{+290.02}_{-42.54}$	$1.45^{+0.57}_{-0.13}$	17.7	24.4	35873*
GRB 240303C	2	48	1.0	2024-03-03 20:04:52.5	$3.0^{+3.16}_{-1.41}$	42.0±13.38	44.65±12.77	$88.93^{+22.47}_{-26.06}$	$26.72^{+13.67}_{-20.99}$	$115.96^{+26.46}_{-40.9}$	$104.0^{+32.68}_{-40.09}$	$0.3^{+0.17}_{-0.25}$	3.5	5.3	35915*
GRB 240303C	0	48	1.0	2024-03-03 20:04:53.5	$6.0^{+1.41}_{-2.24}$	81.87±15.87	85.87±15.39	$229.07^{+30.64}_{-65.8}$	$45.06^{+16.5}_{-17.83}$	$268.63^{+35.09}_{-77.53}$	$276.75^{+36.01}_{-103.16}$	$0.2^{+0.08}_{-0.1}$	5.6	7.8	35915*
GRB 240407A	2	48	1.0	2024-04-07 00:59:52.5	$13.0^{+1.0}_{-1.0}$	135.88±16.79	136.56±16.4	$792.38^{+44.78}_{-44.78}$	$413.07^{+29.82}_{-29.82}$	$1173.33^{+53.8}_{-53.8}$	$1185.02^{+55.52}_{-55.52}$	$0.52^{+0.05}_{-0.05}$	8.3	21.8	36357*

Table 4.5 (*continued*): GRBs detected by VZLUSAT-2.

name	channel	cutoff	t_{exp}	peak time (UTC)	T_{90}	P in 0–255 ADC	P in 0–127 ADC	S in 0–63 ADC	S in 64-127 ADC	S in 0–127 ADC	S in 0–255 ADC	HR	SNR_p	$SNR_{T_{90}}$	GCN no.
		ADC ch.	s	UTC	s	cnt/s	cnt/s	cnt	cnt	cnt	cnt	–	–	–	
GRB 240408B	2	48	1.0	2024-04-08 00:10:03.5	$43.0^{+3.16}_{-2.24}$	103.19±18.3	85.39±16.16	$750.59^{+72.72}_{-74.16}$	$787.05^{+66.96}_{-65.42}$	$1537.63^{+101.53}_{-102.24}$	$1544.82^{+109.6}_{-116.06}$	$1.05^{+0.14}_{-0.14}$	5.3	16.2	36358*
GRB 240425A	2	48	1.0	2024-04-25 00:21:35.5	$33.0^{+3.16}_{-3.16}$	77.14±14.28	69.5±13.49	$398.6^{+65.03}_{-58.23}$	$246.12^{+48.58}_{-37.87}$	$644.74^{+92.88}_{-70.72}$	$613.7^{+100.47}_{-70.43}$	$0.62^{+0.16}_{-0.13}$	5.2	9.7	36363*
GRB 240426A	2	48	1.0	2024-04-26 13:24:05.5	$26.0^{+2.24}_{-2.24}$	45.18±13.86	39.11±12.96	$264.49^{+50.81}_{-56.59}$	$198.43^{+38.29}_{-38.34}$	$462.7^{+65.05}_{-72.74}$	$455.19^{+69.15}_{-71.25}$	$0.75^{+0.2}_{-0.22}$	3.0	7.5	36364*

Table 4.6: Solar flares detected by VZLUSAT-2. Columns are: name analogical to GRB naming convention, VZLUSAT-2 read-out channel which acquired the data, low-energy cutoff, exposure time t_{exp}, peak time of the detection, T_{90} duration, peak flux P in two different energy bands, fluence S in four different energy bands, hardness ratio HR between the two lowest energy bands, and SNR at the peak time and during the T_{90} in the 0–127 ADC band. Explanation of the energy bands can be found in Sec. 3.1.

name	channel	cutoff	t_{exp}	peak time (UTC)	T_{90}	P in 0–255 ADC	P in 0–127 ADC	S in 0–63 ADC	S in 64-127 ADC	S in 0–127 ADC	S in 0–255 ADC	HR	SNR_{p}	$SNR_{\mathrm{T_{90}}}$
		ADC ch.	s	UTC	s	cnt/s	cnt/s	cnt	cnt	cnt	cnt	–	–	–
SF 220421	0	45	1.0	2022-04-21 21:03:46.5	$54.0^{+26.18}_{-14.04}$	106.2±16.25	99.23±15.56	$1335.88^{+121.26}_{-156.14}$	$-60.56^{+46.02}_{-69.68}$	$1257.4^{+103.79}_{-165.87}$	$1394.2^{+144.31}_{-181.82}$	$-0.05^{+-0.03}_{--0.05}$	6.4	13.3
SF 220421	2	45	1.0	2022-04-21 21:03:47.5	$60.0^{+4.12}_{-7.07}$	370.45±22.72	365.69±22.2	$5382.4^{+136.94}_{-169.67}$	$271.84^{+53.34}_{-57.34}$	$5654.23^{+155.23}_{-195.68}$	$5541.03^{+152.93}_{-175.31}$	$0.05^{+0.01}_{-0.01}$	16.5	48.9
SF 220520	2	45	1.0	2022-05-20 22:09:59.5	$11.0^{+5.1}_{-3.16}$	79.85±15.72	76.02±15.03	$284.97^{+48.4}_{-57.2}$	$36.3^{+22.65}_{-26.56}$	$321.27^{+48.16}_{-64.0}$	$329.32^{+49.19}_{-65.16}$	$0.13^{+0.08}_{-0.1}$	5.1	7.2
SF 220715	2	45	1.0	2022-07-15 23:08:47.5	$35.0^{+4.12}_{-4.12}$	151.74±20.45	148.01±19.92	$2175.71^{+119.23}_{-155.24}$	$-16.23^{+39.39}_{-37.82}$	$2159.48^{+127.26}_{-153.32}$	$2129.65^{+130.13}_{-148.45}$	$-0.01^{+-0.02}_{--0.02}$	7.4	20.7
SF 221216	2	48	1.0	2022-12-16 21:58:00.5	$28.0^{+6.08}_{-2.24}$	89.48±18.38	76.48±15.3	$369.47^{+56.43}_{-70.42}$	$130.13^{+43.74}_{-54.12}$	$515.05^{+70.14}_{-102.36}$	$471.87^{+88.36}_{-100.6}$	$0.35^{+0.13}_{-0.16}$	5.0	7.3
SF 221224	2	48	1.0	2022-12-24 04:10:40.5	$38.0^{+7.07}_{-5.1}$	145.11±17.44	147.51±16.7	$2561.79^{+173.52}_{-189.14}$	$99.15^{+44.38}_{-45.81}$	$2660.94^{+180.06}_{-211.5}$	$2470.63^{+171.43}_{-189.28}$	$0.04^{+0.02}_{-0.02}$	8.8	30.4
SF 221224	0	48	1.0	2022-12-24 04:10:57.5	$56.0^{+25.02}_{-7.07}$	66.0±14.42	54.01±13.11	$1542.45^{+244.32}_{-190.0}$	$27.19^{+48.53}_{-69.69}$	$1646.59^{+222.5}_{-218.48}$	$1831.24^{+273.0}_{-259.39}$	$0.02^{+0.03}_{-0.05}$	4.1	18.1
SF 230106	2	48	1.0	2023-01-06 18:48:16.5	$19.0^{+13.04}_{-12.04}$	30.27±12.61	23.95±11.62	$200.01^{+57.57}_{-116.73}$	$-3.13^{+29.72}_{-44.54}$	$200.6^{+50.98}_{-120.06}$	$180.72^{+53.22}_{-111.14}$	$-0.02^{+-0.15}_{--0.22}$	2.1	4.2
SF 230110a	0	48	1.0	2023-01-10 02:13:19.5	$37.0^{+3.16}_{-2.24}$	99.82±16.97	95.5±15.49	$1059.45^{+78.98}_{-79.2}$	$-35.32^{+44.28}_{-43.72}$	$1038.79^{+92.55}_{-90.17}$	$852.33^{+92.48}_{-95.65}$	$-0.03^{+-0.04}_{--0.04}$	6.2	13.0
SF 230110b	2	48	1.0	2023-01-10 17:47:48.5	$38.0^{+3.16}_{-4.12}$	89.01±17.03	77.93±15.1	$478.36^{+67.57}_{-60.24}$	$139.63^{+54.9}_{-52.62}$	$617.98^{+91.81}_{-80.17}$	$788.86^{+112.08}_{-93.26}$	$0.29^{+0.12}_{-0.12}$	5.2	7.8
SF 230110c	2	48	1.0	2023-01-10 22:46:38.5	$98.0^{+5.1}_{-4.12}$	4536.16±68.33	4532.63±68.15	$87561.85^{+358.94}_{-913.19}$	$15697.96^{+140.93}_{-156.58}$	$103580.39^{+394.79}_{-1001.14}$	$103404.41^{+389.78}_{-996.77}$	$0.18^{+0.0}_{-0.0}$	66.5	305.8
SF 230110c	0	48	1.0	2023-01-10 22:46:39.5	$73.0^{+10.05}_{-7.07}$	907.83±32.34	909.57±32.02	$16020.06^{+390.88}_{-417.55}$	$2062.56^{+68.56}_{-75.75}$	$18082.61^{+384.46}_{-441.1}$	$17714.54^{+337.01}_{-398.78}$	$0.13^{+0.01}_{-0.01}$	28.4	111.1
SF 230111	0	48	1.0	2023-01-11 01:53:58.5	$72.0^{+1.41}_{-1.41}$	2841.48±54.62	2837.9±54.42	$77841.89^{+392.97}_{-558.4}$	$6000.95^{+95.63}_{-96.91}$	$83842.84^{+415.51}_{-585.95}$	$83757.02^{+417.33}_{-583.59}$	$0.08^{+0.0}_{-0.0}$	52.2	275.4
SF 230111	2	48	1.0	2023-01-11 01:53:26.5	$55.0^{+2.24}_{-2.24}$	1107.18±35.52	1113.16±35.34	$26960.63^{+359.5}_{-437.17}$	$4079.43^{+82.99}_{-96.32}$	$30886.13^{+376.46}_{-440.42}$	$30759.59^{+371.92}_{-432.76}$	$0.15^{+0.0}_{-0.0}$	31.5	157.7
SF 230211	0	48	1.0	2023-02-11 15:46:21.5	$81.0^{+2.24}_{-7.07}$	489.81±25.57	494.67±25.2	$5939.36^{+143.66}_{-148.04}$	$248.06^{+58.98}_{-61.34}$	$6187.42^{+155.04}_{-164.9}$	$6019.4^{+156.09}_{-180.03}$	$0.04^{+0.01}_{-0.01}$	19.6	47.2
SF 230211	2	48	1.0	2023-02-11 15:45:35.5	$79.0^{+1.41}_{-1.0}$	378.43±22.8	384.13±22.43	$15192.22^{+199.39}_{-161.43}$	$1151.71^{+71.0}_{-69.65}$	$16411.07^{+224.46}_{-181.75}$	$16070.27^{+224.8}_{-188.48}$	$0.08^{+0.0}_{-0.0}$	17.1	102.0
SF 230220	2	48	1.0	2023-02-20 14:55:26.5	$119.0^{+6.08}_{-3.16}$	218.28±21.75	226.63±19.9	$6352.93^{+177.82}_{-164.29}$	$596.42^{+105.16}_{-105.06}$	$7018.61^{+218.32}_{-189.59}$	$7243.3^{+238.82}_{-210.89}$	$0.09^{+0.02}_{-0.02}$	11.4	42.5
SF 230224	2	48	1.0	2023-02-24 17:13:51.5	$40.0^{+13.04}_{-8.06}$	51.21±17.0	34.32±14.0	$539.85^{+98.14}_{-77.1}$	$219.81^{+65.04}_{-68.45}$	$759.66^{+129.45}_{-113.67}$	$781.35^{+174.44}_{-136.5}$	$0.41^{+0.14}_{-0.14}$	2.5	8.9
SF 230307	0	48	1.0	2023-03-07 04:04:35.5	$9.0^{+3.16}_{-3.16}$	40.63±14.14	35.93±12.73	$157.97^{+60.34}_{-36.43}$	$-2.78^{+20.95}_{-18.02}$	$156.02^{+66.38}_{-41.33}$	$119.53^{+70.15}_{-40.91}$	$-0.02^{+-0.13}_{--0.11}$	2.8	4.4
SF 230307	2	48	1.0	2023-03-07 04:02:10.5	$26.0^{+7.07}_{-7.07}$	32.63±13.3	32.0±12.53	$219.66^{+48.34}_{-79.13}$	$37.08^{+39.74}_{-35.03}$	$241.27^{+59.55}_{-80.2}$	$240.01^{+63.74}_{-80.45}$	$0.17^{+0.18}_{-0.17}$	2.6	4.1
SF 230319	2	48	1.0	2023-03-19 02:14:52.5	$28.0^{+8.06}_{-3.16}$	196.66±22.93	203.58±20.95	$1442.64^{+101.42}_{-122.72}$	$140.43^{+56.47}_{-61.09}$	$1605.5^{+109.47}_{-142.94}$	$1640.39^{+128.73}_{-165.65}$	$0.1^{+0.04}_{-0.04}$	9.7	17.7
SF 230319	0	48	1.0	2023-03-19 02:14:52.5	$26.0^{+3.16}_{-4.12}$	276.27±25.14	287.41±23.13	$1898.42^{+119.53}_{-117.31}$	$135.11^{+53.55}_{-52.77}$	$2033.53^{+135.32}_{-122.15}$	$2068.33^{+145.66}_{-121.87}$	$0.07^{+0.03}_{-0.03}$	12.4	22.1
SF 230407	0	48	1.0	2023-04-07 23:33:28.5	$41.0^{+3.16}_{-4.12}$	54.56±13.42	54.77±12.81	$510.3^{+81.57}_{-72.08}$	$98.1^{+42.38}_{-37.25}$	$643.1^{+102.37}_{-84.88}$	$628.95^{+106.33}_{-84.46}$	$0.19^{+0.09}_{-0.08}$	4.3	9.0
SF 230407	2	48	1.0	2023-04-07 23:32:38.5	$74.0^{+4.12}_{-4.12}$	62.76±13.6	57.64±12.85	$1626.83^{+121.33}_{-120.67}$	$254.5^{+58.02}_{-57.69}$	$1881.33^{+142.72}_{-145.57}$	$1933.42^{+146.45}_{-159.13}$	$0.16^{+0.04}_{-0.04}$	4.5	19.0
SF 230410	2	48	1.0	2023-04-10 13:49:21.5	$33.0^{+5.1}_{-1.41}$	435.65±26.51	432.94±24.68	$3857.18^{+166.09}_{-129.19}$	$297.8^{+53.64}_{-52.99}$	$4001.85^{+170.48}_{-134.84}$	$3911.04^{+152.49}_{-144.96}$	$0.08^{+0.01}_{-0.01}$	17.5	40.3
SF 230520a	2	48	1.0	2023-05-20 07:30:54.5	$108.0^{+3.16}_{-2.24}$	308.02±23.77	319.99±22.07	$13146.72^{+265.02}_{-201.93}$	$1431.0^{+106.62}_{-105.38}$	$14577.73^{+311.71}_{-239.8}$	$13687.06^{+301.81}_{-263.85}$	$0.11^{+0.01}_{-0.01}$	14.5	80.7
SF 230520b	2	48	1.0	2023-05-20 12:34:34.5	$144.0^{+12.04}_{-13.04}$	172.86±17.32	178.03±16.82	$4626.73^{+154.83}_{-260.78}$	$3179.25^{+201.38}_{-287.45}$	$6788.06^{+261.58}_{-439.29}$	$6562.53^{+258.44}_{-444.42}$	$0.69^{+0.05}_{-0.07}$	10.6	46.3
SF 230531	0	48	1.0	2023-05-31 12:25:56.5	$56.0^{+1.41}_{-1.41}$	675.62±29.39	682.23±28.84	$20841.01^{+222.63}_{-238.08}$	$3313.32^{+98.88}_{-84.37}$	$24152.89^{+277.21}_{-266.13}$	$24059.89^{+277.11}_{-269.48}$	$0.16^{+0.0}_{-0.0}$	23.7	133.8

Table 4.6 (*continued*): Solar flares detected by VZLUSAT-2.

name	channel	cutoff	t_{exp}	peak time (UTC)	T_{90}	P in 0–255 ADC	P in 0–127 ADC	S in 0–63 ADC	S in 64-127 ADC	S in 0–127 ADC	S in 0–255 ADC	HR	SNR_{p}	$SNR_{\mathrm{T_{90}}}$
		ADC ch.	s	UTC	s	cnt/s	cnt/s	cnt	cnt	cnt	cnt	–	–	–
SF 230618	2	48	1.0	2023-06-18 00:30:22.5	$58.0^{+2.24}_{-3.16}$	348.41±22.63	351.36±22.05	$6453.71^{+166.74}_{-153.19}$	$53.43^{+60.88}_{-50.99}$	$6640.46^{+188.37}_{-145.4}$	$6603.25^{+192.32}_{-154.84}$	$0.01^{+0.01}_{-0.01}$	15.9	55.3
SF 230702	2	48	1.0	2023-07-02 02:32:54.5	$68.0^{+3.16}_{-2.24}$	145.04±20.25	143.2±18.08	$3354.29^{+114.01}_{-119.36}$	$1117.02^{+84.7}_{-93.16}$	$4504.85^{+141.05}_{-160.01}$	$4638.55^{+159.0}_{-183.99}$	$0.33^{+0.03}_{-0.03}$	7.9	34.6
SF 230704	0	48	1.0	2023-07-04 21:32:40.5	$13.0^{+3.16}_{-6.08}$	55.87±14.11	45.63±13.11	$121.45^{+51.09}_{-36.79}$	$6.94^{+20.61}_{-22.44}$	$132.81^{+51.25}_{-42.37}$	$190.85^{+53.52}_{-58.58}$	$0.06^{+0.17}_{-0.19}$	3.5	3.2
SF 230704	2	48	1.0	2023-07-04 21:32:30.5	$14.0^{+2.24}_{-5.1}$	45.19±13.6	45.17±12.88	$188.16^{+46.51}_{-62.52}$	$-23.55^{+26.53}_{-28.16}$	$173.71^{+45.42}_{-64.4}$	$148.41^{+47.26}_{-56.89}$	$-0.13^{+-0.14}_{--0.16}$	3.5	4.0
SF 230725	2	48	1.0	2023-07-25 23:44:06.5	$91.0^{+8.06}_{-9.06}$	83.31±15.26	86.34±14.73	$3538.87^{+130.1}_{-153.84}$	$-15.08^{+58.9}_{-64.87}$	$3528.32^{+138.86}_{-177.34}$	$3385.46^{+140.56}_{-168.91}$	$-0.0^{+-0.02}_{--0.02}$	5.9	28.4
SF 230906	2	48	1.0	2023-09-06 00:49:47.5	$39.0^{+2.24}_{-2.24}$	310.21±23.98	310.5±22.25	$5003.62^{+126.23}_{-142.05}$	$1101.95^{+60.17}_{-59.27}$	$6044.16^{+137.23}_{-147.42}$	$5767.72^{+137.98}_{-149.54}$	$0.22^{+0.01}_{-0.01}$	14.0	52.4
SF 231120	2	48	1.0	2023-11-20 03:10:11.5	$18.0^{+3.16}_{-6.08}$	51.41±13.78	47.85±13.04	$278.3^{+54.58}_{-68.83}$	$18.02^{+33.98}_{-28.37}$	$326.33^{+68.05}_{-72.68}$	$332.07^{+68.29}_{-75.67}$	$0.06^{+0.12}_{-0.1}$	3.7	6.5
SF 231206	0	48	1.0	2023-12-06 05:38:39.5	$21.0^{+2.24}_{-3.16}$	118.85±19.03	111.05±17.23	$1132.17^{+77.44}_{-72.23}$	$44.61^{+40.15}_{-46.09}$	$1183.58^{+91.54}_{-92.92}$	$1232.94^{+114.29}_{-92.33}$	$0.04^{+0.04}_{-0.04}$	6.4	16.6
SF 231230	2	48	1.0	2023-12-30 21:25:50.5	$6.0^{+1.41}_{-2.24}$	64.94±16.61	66.16±14.76	$216.54^{+31.69}_{-55.82}$	$-6.28^{+24.92}_{-20.49}$	$210.26^{+41.51}_{-48.42}$	$197.15^{+51.57}_{-50.29}$	$-0.03^{+-0.12}_{--0.09}$	4.5	6.3
SF 240104	2	48	1.0	2024-01-04 01:13:04.5	$67.0^{+13.04}_{-9.06}$	54.7±13.42	58.94±13.08	$1308.29^{+108.42}_{-139.88}$	$-46.42^{+60.0}_{-51.01}$	$1261.87^{+135.56}_{-135.81}$	$1247.14^{+141.33}_{-127.77}$	$-0.04^{+-0.05}_{--0.04}$	4.5	13.5
SF 240104	0	48	1.0	2024-01-04 01:13:04.5	$65.0^{+2.24}_{-2.24}$	435.9±24.39	432.77±24.04	$8776.05^{+188.8}_{-150.85}$	$38.98^{+51.4}_{-47.88}$	$8814.07^{+201.35}_{-156.07}$	$8829.08^{+202.7}_{-160.27}$	$0.0^{+0.01}_{-0.01}$	18.0	65.3
SF 240111	2	48	1.0	2024-01-11 17:50:56.5	$30.0^{+5.1}_{-4.12}$	100.36±15.46	93.31±14.7	$1394.06^{+76.32}_{-99.16}$	$68.26^{+43.23}_{-43.57}$	$1462.32^{+82.43}_{-103.25}$	$1452.91^{+88.97}_{-105.65}$	$0.05^{+0.03}_{-0.03}$	6.3	20.4
SF 240222	2	48	1.0	2024-02-22 06:29:19.5	$135.0^{+4.12}_{-3.16}$	667.52±28.16	644.25±27.82	$27807.26^{+310.28}_{-296.97}$	$374.97^{+76.03}_{-76.9}$	$28182.23^{+317.48}_{-308.21}$	$31000.85^{+358.03}_{-352.15}$	$0.01^{+0.0}_{-0.0}$	23.2	131.6
SF 240319	0	48	1.0	2024-03-19 23:25:01.5	$30.0^{+2.24}_{-3.16}$	77.77±17.92	81.53±16.34	$806.77^{+68.54}_{-91.6}$	$180.97^{+48.31}_{-48.23}$	$987.74^{+87.1}_{-106.86}$	$987.6^{+96.32}_{-119.58}$	$0.22^{+0.06}_{-0.06}$	5.0	12.2
SF 240324	2	48	1.0	2024-03-24 06:05:44.5	$26.0^{+4.12}_{-3.16}$	249.63±19.95	252.22±19.49	$2355.49^{+88.92}_{-112.65}$	$189.26^{+36.89}_{-39.64}$	$2537.2^{+90.26}_{-135.41}$	$2515.2^{+96.14}_{-128.11}$	$0.08^{+0.02}_{-0.02}$	12.9	33.1
SF 240326	0	48	1.0	2024-03-26 02:25:44.5	$16.0^{+2.24}_{-3.16}$	74.55±15.56	71.6±14.76	$771.8^{+56.01}_{-68.65}$	$-47.77^{+30.58}_{-23.49}$	$691.2^{+58.04}_{-61.64}$	$702.48^{+61.62}_{-68.81}$	$-0.06^{+-0.04}_{--0.03}$	4.8	12.5
SF 240326	2	48	1.0	2024-03-26 02:25:49.5	$18.0^{+1.41}_{-2.24}$	116.96±16.43	115.52±15.75	$1163.6^{+55.41}_{-69.93}$	$47.42^{+29.22}_{-28.46}$	$1211.02^{+64.14}_{-77.96}$	$1185.3^{+71.9}_{-75.09}$	$0.04^{+0.03}_{-0.02}$	7.3	20.2

Table 4.7: Flashes from soft gamma repeaters detected by VZLUSAT-2. Columns are: event name, VZLUSAT-2 read-out channel which acquired the data, low-energy cutoff, exposure time t_{exp}, peak time of the detection, T_{90} duration, peak flux P in two different energy bands, fluence S in four different energy bands, hardness ratio HR between the two lowest energy bands, SNR at the peak time and during the T_{90} in the 0–127 ADC band, and the GCN Circular number in which the detection was announced. Explanation of the energy bands can be found in Sec. 3.1. GCN Circulars which are marked with an asterix were prepared by the author of this work.

name	channel	cutoff	t_{exp}	peak time (UTC)	T_{90}	P in 0–255 ADC	P in 0–127 ADC	S in 0–63 ADC	S in 64-127 ADC	S in 0–127 ADC	S in 0–255 ADC	HR	SNR_{p}	$SNR_{\mathrm{T_{90}}}$	GCN no.
		ADC ch.	s	UTC	s	cnt/s	cnt/s	cnt	cnt	cnt	cnt	–	–	–	
SGR 1935+2154	2	48	1.0	2022-10-12 23:26:41.5	$1.0^{+1.0}_{-1.41}$	173.14±19.77	167.81±18.33	$164.34^{+16.19}_{-165.13}$	$2.88^{+8.6}_{-11.2}$	$167.81^{+18.33}_{-168.81}$	$173.14^{+19.77}_{-181.76}$	$0.02^{+0.05}_{-0.07}$	9.2	9.2	32797
SGR 1935+2154	2	48	1.0	2022-10-13 02:02:43.5	$1.0^{+1.41}_{-1.0}$	176.45±20.62	169.65±19.16	$166.17^{+37.96}_{-19.18}$	$3.48^{+9.86}_{-9.94}$	$169.65^{+38.03}_{-19.95}$	$176.45^{+62.44}_{-23.39}$	$0.02^{+0.06}_{-0.06}$	8.9	8.9	32797
SGR 1935+2154	2	48	1.0	2022-10-13 22:41:28.5	$1.0^{+1.0}_{-1.0}$	1185.79±36.4	1189.57±36.21	$1103.07^{+33.21}_{-33.21}$	$85.64^{+9.25}_{-9.25}$	$1189.57^{+34.49}_{-34.49}$	$1185.79^{+34.44}_{-34.44}$	$0.08^{+0.01}_{-0.01}$	32.9	34.5	32797
SGR 1935+2154	2	48	1.0	2022-10-14 17:27:36.5	$3.0^{+10.05}_{-1.0}$	1145.56±38.97	1137.7±37.46	$1267.93^{+695.6}_{-42.63}$	$359.22^{+102.08}_{-24.92}$	$1627.15^{+794.82}_{-49.38}$	$1658.55^{+762.31}_{-52.86}$	$0.28^{+0.18}_{-0.02}$	30.4	33.0	32814
SGR 1806-20	2	48	1.0	2023-03-10 21:00:34.5	$1.0^{+1.0}_{-1.0}$	556.32±28.55	558.06±27.11	$549.9^{+23.45}_{-23.45}$	$8.15^{+2.85}_{-2.85}$	$558.06^{+23.62}_{-23.62}$	$556.32^{+23.59}_{-23.59}$	$0.01^{+0.01}_{-0.01}$	20.6	23.6	33473*
SGR 1806-20	0	48	1.0	2023-03-10 21:00:34.5	$1.0^{+1.0}_{-1.0}$	182.21±21.42	190.33±19.47	$187.85^{+13.71}_{-13.71}$	$2.48^{+1.57}_{-1.57}$	$190.33^{+13.8}_{-13.8}$	$182.21^{+13.5}_{-13.5}$	$0.01^{+0.01}_{-0.01}$	9.8	13.8	33473*

4.1.2 Distributions of observational characteristics

Duration vs. spectral hardness

Fig. 4.3 shows all detected transients in the $HR - T_{90}$ plane separated by the event type. GRBs are further divided into long and short based on the classification done by other missions with better temporal resolution. The well-known bimodal distribution of GRB durations is clearly seen and the bimodal nature is strengthened when the hardness ratio is introduced. The anti-correlation of hardness ratio on the event duration does not stop at long GRBs but continues towards longer and softer solar flares. The longest events detected are among solar flares which seem to have a rather uniform HR distribution with sharper boundary at the high-energy end around 0.6 and with a weak tail at low-energy end. Most of soft gamma repeaters fall into the fourth, bottom left, corner of the plot which encompasses short and soft events. Few SGR bursts appear longer, however, this is because of a so-called forest of bursts, a collection of many brief spikes which are either indistinguishable by our temporal resolution or separated by only one or two bins. So far, only one outburst from an X-ray binary has been detected and on the $HR - T_{90}$ plane it lies at the boundary of the transient types.

This simple but elegant division of the $HR - T_{90}$ plane by the event types suggests it to be used for a classification of uncertain peaks. One of the related issues is the aforementioned forest of SGR bursts. To avoid misclassification of these events, another parameter would need to be introduced. Solar flares are typically broad-peaked structures, therefore, the parameter could describe the spikiness of the light curves. However, the characterization of a light curve structure is a long-standing problem, especially in the GRB community. Another helpful use case of this classification method could be to distinguish real transients from background-induced detections. However, it is very challenging to create a representative sample of background peaks because the van Allen radiation belts, especially their boundaries, are highly variable. To identify these non-astrophysical sources, introducing satellite's position as yet another parameter could be beneficial.

A comparison of the hardness ratio and the T_{90} duration for events which were observed by both CubeSats or both detector units on-board VZLUSAT-2 is shown in Fig. 4.4. The differences between GRBAlpha and VZLUSAT-2 values can be caused by different satellite orientations and positions in their orbits, i.e. different background levels. The discrepancies between the two detector units on-board VZLUSAT-2 are likely related to the orientation and rotation of the satellite. For instance, GRB 230409D was observed to be harder by the detector unit 1 (channel 2) but this is likely only a side effect of the satellite orientation. Large portion of the detector unit 1 was covered by the detector unit 0 (Fig. 4.6, top) and to reach its uncovered part, the incident particles must have crossed the satellite body which might have reduced the signal in the lowest energies where the satellite is least transparent. Moreover, the satellite's orientation often changes throughout the entire duration of an event which brings further complications to the analysis. The data can be corrected for these effects by the detector response matrix (Sec. 2.1.3), however, the DRM is not yet simulated for VZLUSAT-2. Although GRBAlpha's DRM is available, we lack the information about its orientation.

Fig. 4.5 shows a comparison of the T_{90} durations measured by the CubeSat missions and Fermi/GBM for all joint GRB detections. On average, the GBM duration is longer

than that measured by GRBAlpha and VZLUSAT-2. The median T_{90} of GRBAlpha GRBs is 15 s while median GBM duration for the same dataset is 22 s. VZLUSAT-2 observed a median T_{90} duration to be 19 s while GBM measured median of 26 s for the VZLUSAT-2 GRBs. This can be explained by the fact that the GBM detectors have much larger effective area and are thus more sensitive to GRB precursors and fainter extended emission. Another reason for this offset can be the polar orbit of the CubeSats. Some GRBs were observed near the radiation belts what caused that these events were detected only partially. For instance, this was the case of the brightest-of-all-time GRB 221009A (Ripa et al., 2022; Řípa et al., 2023), a second part of which was detected inside of the radiation belt, and also the extremely bright GRB 230307A (Dafcikova et al., 2023) which was detected by GRBAlpha shortly before it entered the radiation belt, and therefore the tail part of the burst is buried under the particle background. Many events were also observed near the poles where the background is usually stable but nearly twice as high as at the equator. Therefore, the significance and also the duration of these events is measured to be lower than by other missions with better signal-to-noise ratio.

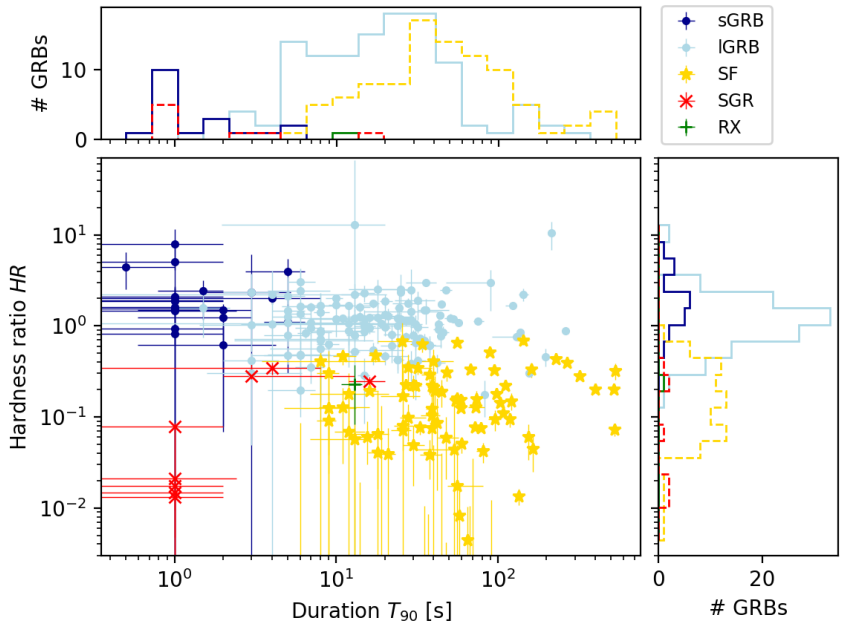

Figure 4.3: Hardness ratio vs. T_{90} duration for all GRBAlpha and VZLUSAT-2 detections. The hardness ratio *HR* is defined as the ratio of the total counts in T_{90} of the two lowest energy bands. Note that the energy bands do not correspond to the same energies for all detections because different cutoff is used at each satellite, and the degradation of MPPCs at GRBAlpha has decreased the gain which shifted the energies to higher values (Sec. 3.1). Colors distinguish between GRBs, SGRs, solar flares (SF) and X-ray binaries (RX). GRBs are significantly harder than other classes. Among softer sources are longer solar flares and shorter soft gamma repeaters. Activity from an X-ray binary was only detected once and this detection lies at the boundary of GRBs, SFs and SGRs. Some of the SGRs appear longer what might be caused by a burst forest which was considered as one event in our analysis, however, in reality was a series of individual short bursts. GRBs are furthermore divided into short and long based on their duration determined by other missions with finer temporal resolution.

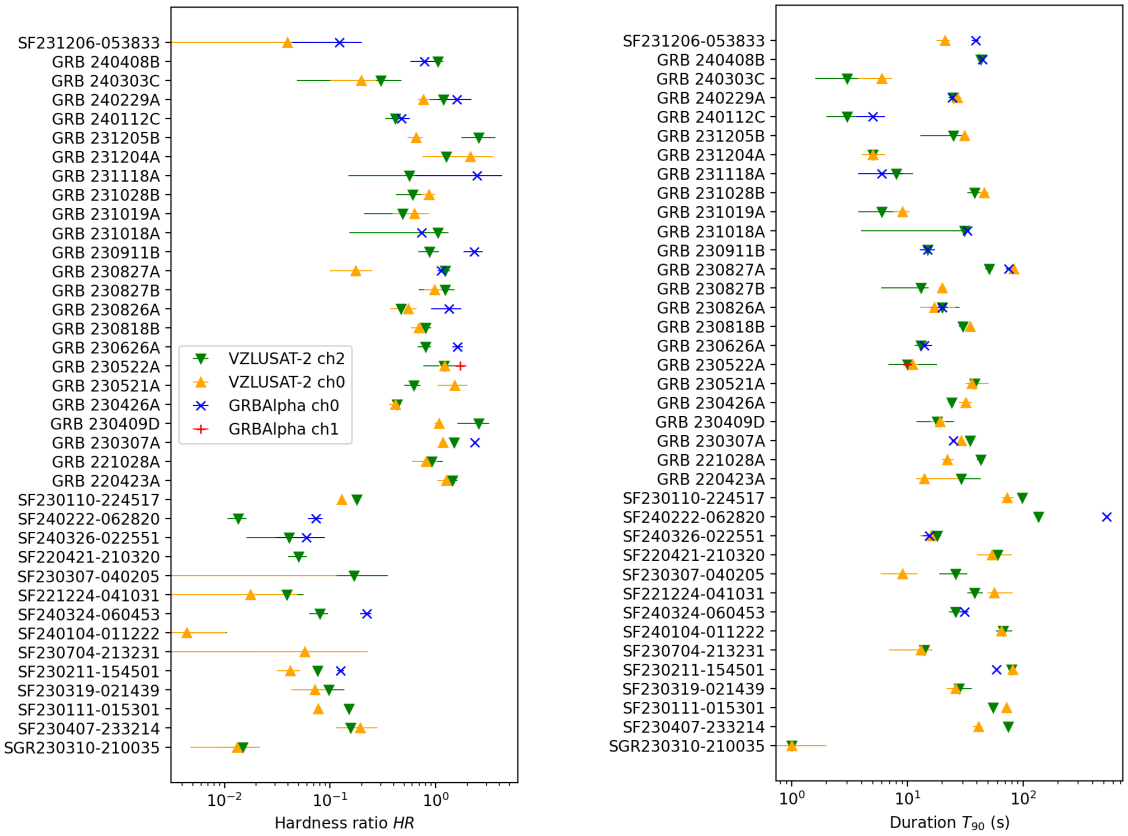

Figure 4.4: A comparison of the hardness ratios *HR* (left) and T_{90} durations (right) of the events detected by more detectors.

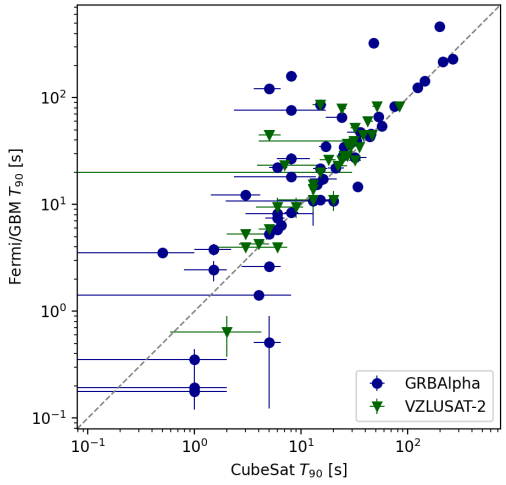

Figure 4.5: A comparison of the GRB T_{90} durations as observed by GRBAlpha and VZLUSAT-2 with Fermi/GBM. On average, the CubeSats measure shorter durations than GBM. This is likely due to the larger effective area of GBM that is therefore more sensitive to fainter precursors and extended emission of GRBs. Many events were also observed near the van Allen radiation belts where the measured background is higher and less stable, and the significance of the detection, thus the observed duration, decreases. On the short-duration end, the sensitivity is limited by the exposure time of the CubeSats which is currently 1 s for VZLUSAT-2 and 0.5 s for GRBAlpha.

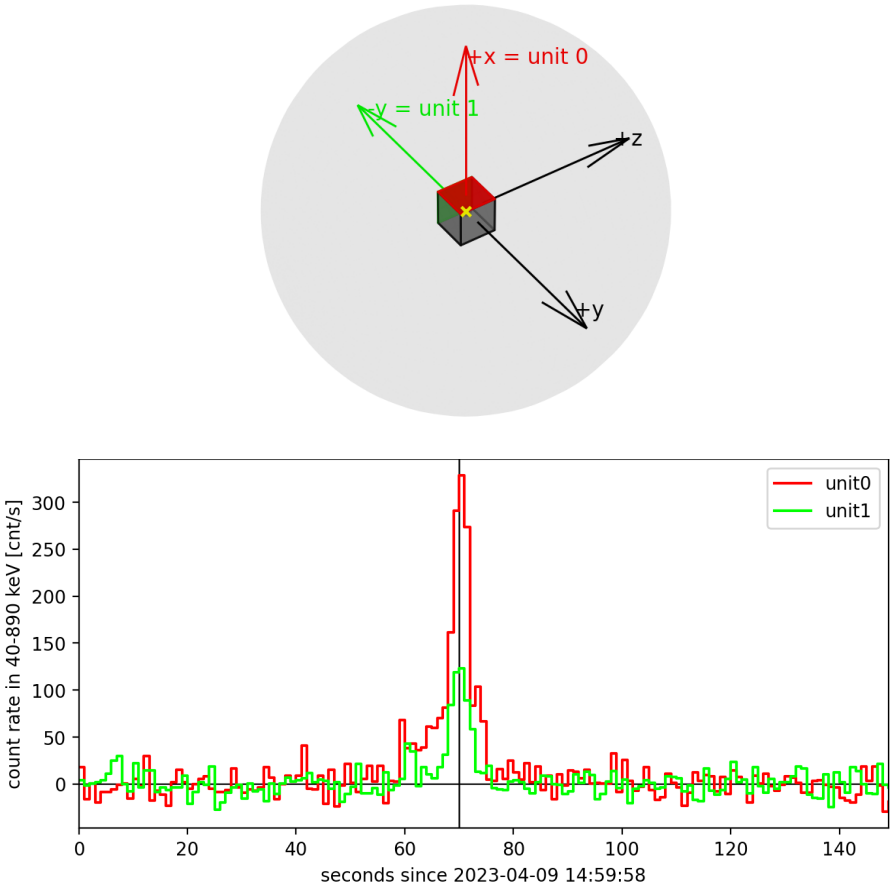

Figure 4.6: An example of VZLUSAT-2 orientation at the peak time of GRB 230409D. Bottom panel shows the background-subtracted light curves measured by both detector units. The vertical solid line marks the time for which the satellite's orientation is illustrated in the top panel. The satellite is depicted as would be seen from the source location. It is evident that the detector unit 0 covered large portion of the detector unit 1. Consequently, the measured count rate is higher in data from unit 0. Moreover, unit 1 only detected those particles and photons which were energetic enough to cross the satellite body. This reduced the detected count rate in the lowest energies which resulted in harder observed spectrum of this GRB by the detector unit 1.

Peak flux and fluence

The distribution of the measured peak flux does not significantly vary between individual transient types. The distribution is skewed with median values of ~ 73 cnt/s for short GRBs, ~ 112 cnt/s for long GRBs, ~ 127 cnt/s for solar flares, and ~ 228 cnt/s for soft gamma repeaters. The higher median of SGR fluxes is most likely only a result of a small sample size. The sharper boundary at low fluxes is related to the detection limit of faint events. The weak tail towards high fluxes represents the low occurrence rate of very bright transients.

The observed fluence is higher in case of long GRBs and solar flares. However, the distributions follow the T_{90} distributions (Fig. 4.3, top panel). Therefore, this can be explained solely by the fact that these events last longer and in the end accumulate more counts during their duration.

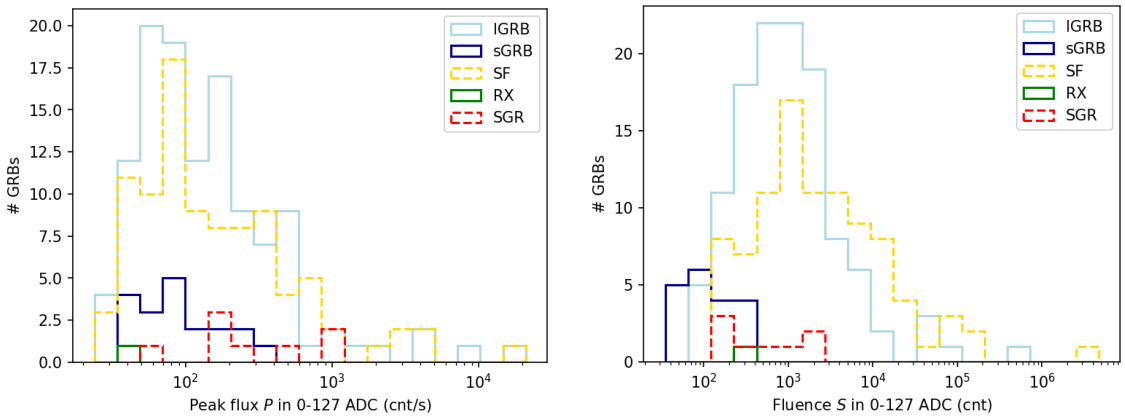

Figure 4.7: Distributions of the peak flux P (left) and fluence S (right) for different transient types. The distribution of peak flux does not significantly vary for different types of events. The fluence is on average higher for long GRBs and solar flares which is related to their longer duration.

Solar flares

A relatively large sample of solar flares detected by GRBAlpha and VZLUSAT-2 allows us to look closer at the characteristics of individual SF classes. Most of the 77 detections belong to the C (32) and M (37) classes, two B class solar flares were observed and six bright ones belonging to the X class.

The distributions of their durations, hardness ratios, peak fluxes and fluences are presented in Fig. 4.8. The T_{90} duration, peak flux and fluence all appear to be in accordance with each other and also with the SF class. Brighter solar flares in soft X-rays last longer and are also brighter in soft gamma-rays.

The most interesting result regarding solar flares is the distribution of their observed hardness ratios which seems to be uniform across individual classes. Note, that many solar flares were only detected in the lowest energies and therefore this distribution might be biased by background fluctuations present in the second lowest energy band. Some solar flares even have negative values of the hardness ratios and lie outside of this plot. However, few strong solar flares were also observed in our highest energies (Sec. 4.1.3).

4.1.3 Selected events

Every transient included in this catalogue demonstrates the extraordinary nature of our universe and deserves an admiration on its own. In this section, we briefly mention few of the most exceptional detections.

GRB 231215A: the most distant GRB

This long GRB is the most distant transient with known redshift detected by GRBAlpha at z = 2.305 (Thoene et al., 2023). Assuming a flat ΛCDM model (H_0 = 69.6 km/s/Mpc, Ω_M = 0.29, Ω_0 = 0.71), the light travel time is 10.8 Gyr. This is the look-back time of a satellite which can be hold in one hand.

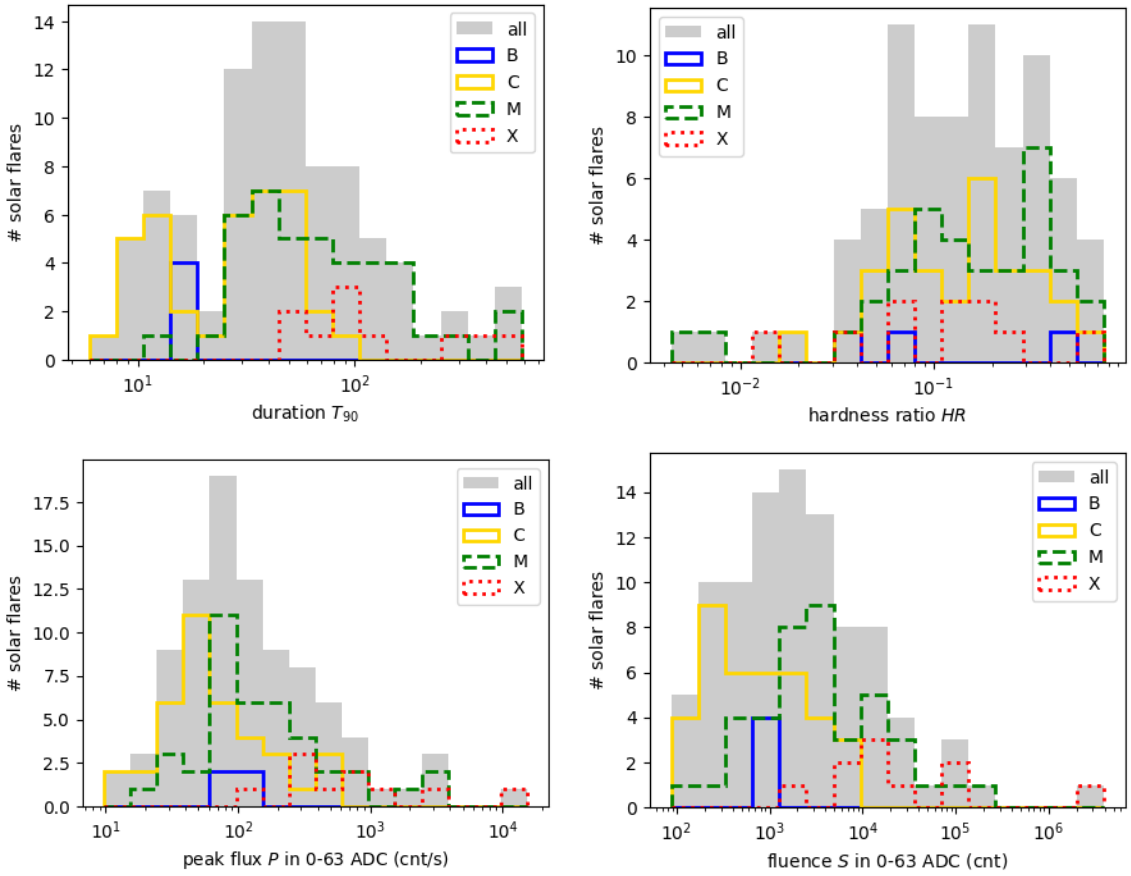

Figure 4.8: Distributions of the T_{90} duration (top left), hardness ratio HR (top right), peak flux P (bottom left) and fluence S (bottom right) for solar flares separated into their sub-classes based on their peak flux in soft X-rays. Although the hardness ratio does not significantly vary between the classes, stronger flares seem to last longer and exhibit higher peak fluxes and fluences also in soft gamma-rays.

GRB 221009A: the brightest-of-all-time GRB

GRBAlpha got lucky when, only shortly after a software upgrade which allowed us to run continuous measurements, the brightest-of-all-time (BOAT) GRB 221009A occurred. The small detector size turned out to be an advantage in such an extreme case as it did not get saturated, compared to large spacecrafts such as Fermi or Swift. This allowed us to accurately measure the peak flux of this exceptional event (Řípa et al., 2023).

SF 240222c: an X6 class solar flare

Another example of an extraordinarily bright event comes from much closer distances of our solar system. An X6 class solar flare was observed by GRBAlpha on February 22, 2024 (Fig. 4.9). The peak flux of this solar flare was nearly as high as the peak flux of the BOAT and in the fluence distribution it is the brightest transient of this catalogue. GRBAlpha and VZLUSAT-2 have detected more X-class solar flares, however, none of them showed such extraordinary behaviour in soft gamma-rays. Another peculiarity about

this event is that it was observed in the highest energies. This high-energy bump was also observed for an M6.5 class solar flare on May 9, 2023 which was also very bright with a peak flux of ~ 5000 cnt/s. It is interesting that in the middle energy band the detection is absent. Although GRBAlpha was approaching the radiation belt (Fig. 4.10), at these latitudes we usually observe no or very few counts in the highest energy band.

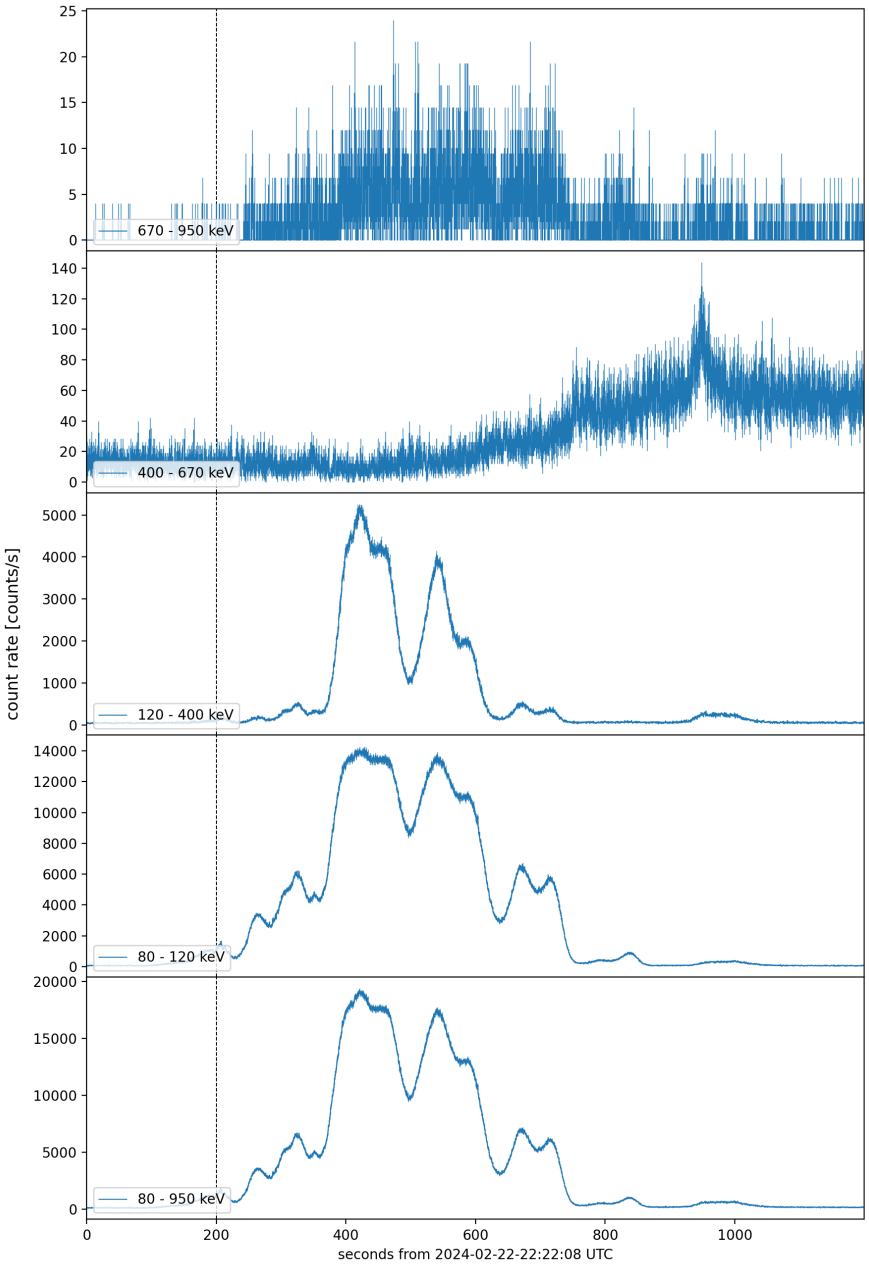

Figure 4.9: Light curve of an X6 class solar flare as observed by GRBAlpha. The vertical dashed line marks the trigger time by Konus/Wind. The peak flux of this solar flare was nearly as high as the peak flux of the BOAT GRB 221009A. In the energies of $\sim 400 - 670$ keV, only the LEO particle background is observed which is increasing as the satellite is moving towards the radiation belt (Fig. 4.10).

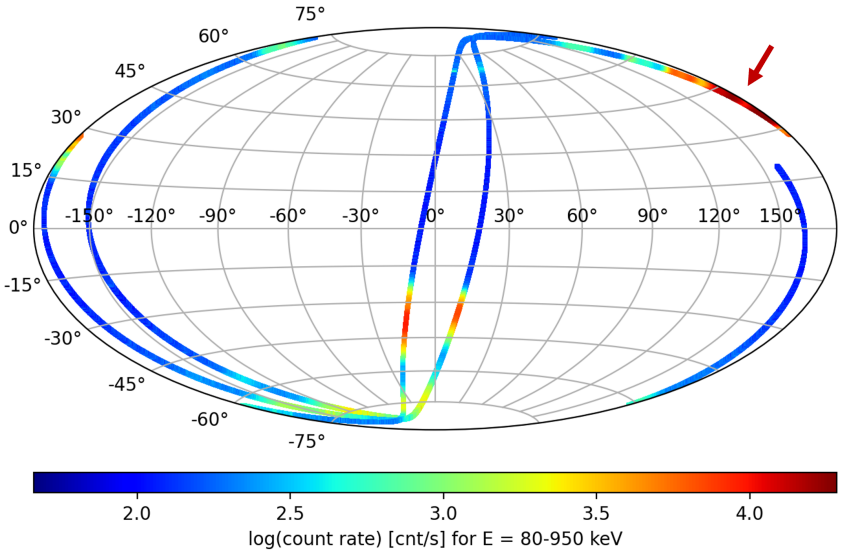

Figure 4.10: Ground tracks of GRBAlpha during two orbits around the Earth on February 22, 2024. The red arrow points at the brightest transient in our catalogoue, an X6-class solar flare.

4.2 Detector sensitivity

4.2.1 Theoretical sensitivity

We demonstrate the theoretical sensitivity in terms of fluence of a typical long and short GRB which would be detected by our nanosatellites with SNR = 5. The estimation was done according to the steps described in Sec. 3.3. The typical spectral parameters for a CPL model used in the calculation are stated in Tab. 4.8. The calculated threshold fluence values S_{thr} for GRBAlpha and VZLUSAT-2 are presented in Tab. 4.9 and 4.10, respectively. Fig. 4.11 shows the simulated photon spectra of the typical GRBs and the count spectra which would be measured by the detectors on-board GRBAlpha and VZLUSAT-2 if the GRBs were observed as 5σ detections. The difference between the two satellites is due to lower low-energy threshold used for data acquisition by VZLUSAT-2 which is therefore more sensitive to softer events.

Fig. 4.12 shows the threshold values plotted over the complementary cumulative distribution function (CCDF) of Fermi/GBM GRBs. Depending on the low-energy threshold, the detector should be able to detect at least $\sim 50-60\%$ of long GBM GRBs and $\sim 70-80\%$ of short GBM GRBs. GBM yearly detects ~ 200 long and ~ 40 short GRBs. Assuming the same orbit as Fermi, our detector should detect $\sim 120-150$ GRBs per year. For a constellation of satellites providing a full-sky coverage, the expected detection rate is $\sim 170-210$ GRBs per year. This estimation is more positive than the one derived from the observed detection rate by GRBAlpha discussed in Sec. 4.1.1. The longest continuous observing time of GRBAlpha was around three months and although it is getting higher, occasionally there is a few-week-long period without any operations. Therefore, the estimation of the detection rate for continuous operations may be biased by the selected periods and we expect it to increase with more stable observing time.

Table 4.8: Spectral and temporal parameters of typical GRBs (Galgóczi et al., 2021) used to simulate the spectrum of a 5σ detection by the detectors on-board GRBAlpha and VZLUSAT-2.

	A	α	E_{peak}	T_{90}
	ph cm^{-2} s^{-1} keV^{-1}	–	keV	s
sGRB	0.0068	-0.38	669	1
lGRB	0.009	-0.96	183	20

Table 4.9: Calculated values of the threshold amplitude A_{thr} and fluence S_{thr} of a typical short and long GRB as would be observed by GRBAlpha.

	A	S_{thr} (10–1000 keV)	S_{thr} (50–300 keV)
	ph cm^{-2} s^{-1} keV^{-1}	10^{-6} erg/cm^2	10^{-6} erg/cm^2
sGRB	0.013373	1.5072	0.4704
lGRB	0.005451	2.9427	1.7856

Table 4.10: The same as Tab. 4.9 but for VZLUSAT-2.

	A	S_{thr} (10–1000 keV)	S_{thr} (50–300 keV)
	ph cm^{-2} s^{-1} keV^{-1}	10^{-6} erg/cm^2	10^{-6} erg/cm^2
sGRB	0.010256	1.1559	0.3608
lGRB	0.003301	1.7821	1.0813

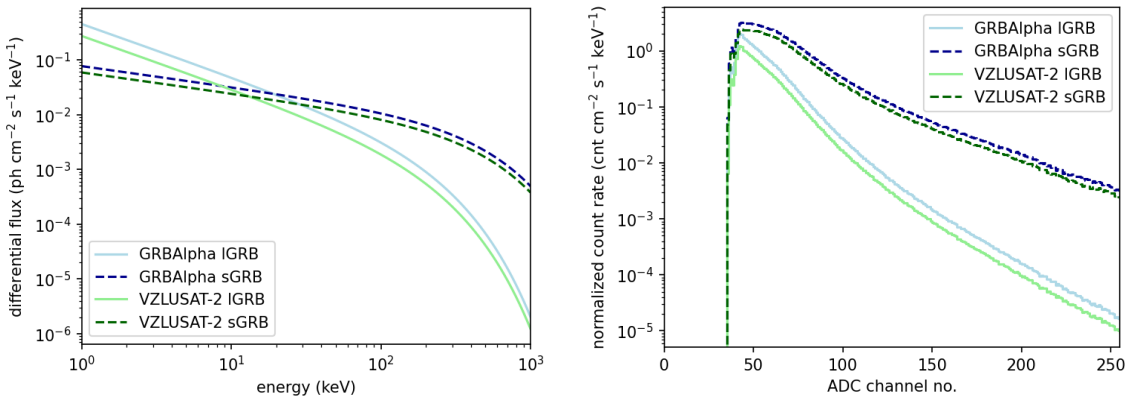

Figure 4.11: Simulated photon spectra (left) and count spectra which would be measured on-axis by our detectors (right) of a typical long and short GRB detected with SNR = 5.

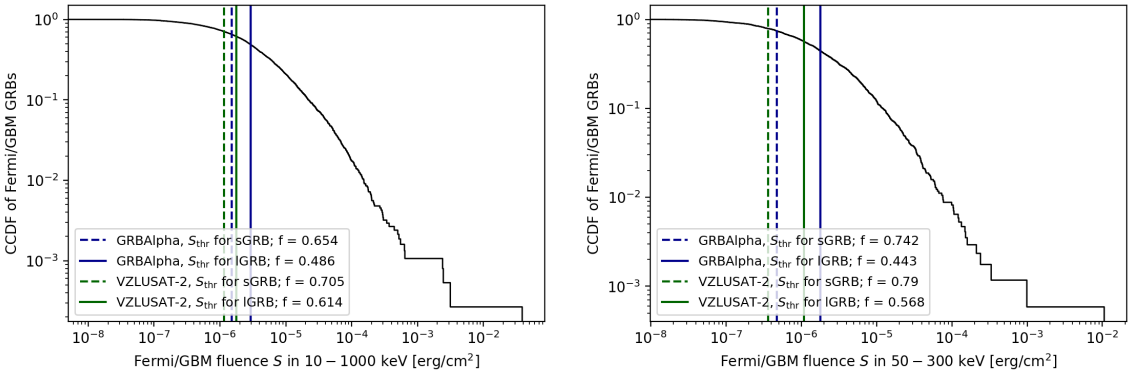

Figure 4.12: Complementary cumulative distribution functions of the fluence of all GRBs detected by Fermi/GBM. The black curve marks the normalized number of GBM GRBs with fluence higher than or equal to the given value. The vertical solid lines mark the theoretical value for GRBAlpha and VZLUSAT-2 threshold detection of a typical long GRB with SNR = 5. The vertical dashed lines mark the theoretical value for GRBAlpha and VZLUSAT-2 threshold detection of a typical short GRB with SNR = 5. In the legends, f is the fraction of GRBs brighter than the marked value.

4.2.2 Cross-correlation with Fermi/GBM

Thanks to its large effective area and field of view, Fermi/GBM has the highest GRB detection rate from all current GRB-observing instruments. To study the empirical sensitivity of our detector, we compare the observed characteristics by our missions with those measured by GBM for all jointly detected GRBs. Fig. 4.13 shows the correlations between the peak flux and fluence observed by GBM and GRBAlpha or VZLUSAT-2. The light and bright color distinguishes between sub-threshold ($3 \leq \mathrm{SNR} < 5$) and significant ($\mathrm{SNR} \geq 5$) detections. The sub-threshold detections of bright GRBs are likely due to satellite orientation and higher background levels. In case of VZLUSAT-2, the detection significance is also reduced if one detector unit partially covers the other.

Detection of faint GRBs

More interesting are the significant observations of faint GRBs. We identify four significant detections below the calculated threshold values discussed in Sec. 4.2.1; one short and two long GRBs detected by GRBAlpha, and one long GRB observed by VZLUSAT-2. Their spectral parameters for a CPL model are summarized in Tab. 4.11 and the comparison of their spectra with the theoretical spectrum of a threshold detection of a typical GRB is shown in Fig. 4.14. Closer inspection reveals that the three faint long GRBs were harder than a typical long GRB which explains the higher observed significance. This suggests that although due to the higher low-energy cutoff we lose some softer events, because we collect less of the noisier low-energy background the higher cutoff may be beneficial for detecting harder GRBs. These are usually short GRBs which are related to neutron star mergers. The detector concept is thus suitable for contributing to the search for electromagnetic counterparts to gravitational waves. Interestingly, the spectrum of the faint short GRB 230102A appears to be softer compared to a typical short GRB. However, the SNR of this event is only slightly above the 5σ threshold (SNR = 5.4), therefore, this detection could be explained by favourable satellite orientation and low background level.

Table 4.11: Spectral parameters of significant ($\mathrm{SNR} \geq 5$) GRB detections with Fermi/GBM fluence lower than the threshold value calculated for a 5σ detection (Tab. 4.9, 4.10). The indices G and V mark whether the GRB was observed by GRBAlpha or VZLUSAT-2, respectlively. The GBM fluence S_{GBM} is for the entire energy range of $10 - 10^3$ keV, the GBM BATSE fluence $S_{\mathrm{GBM,batse}}$ is for the band $50 - 300$ keV. References: [1] Krimm et al. (2024), [2] Cheung et al. (2024), [3] Cheung et al. (2023), [4] Fletcher and Meegan (2023).

name	S_{GBM}	$S_{\mathrm{GBM,batse}}$	α	E_{peak}	ref.
	10^{-6} erg/cm^2	10^{-6} erg/cm^2	–	keV	
lGRB 240222A$^{\mathrm{G}}$	0.484	0.263	0.104	155	[1]
lGRB 240216A$^{\mathrm{G}}$	2.27	1.09	0.3	1230	[2]
lGRB 231019A$^{\mathrm{V}}$	1.48	0.912	4.3	130	[3]
sGRB 230102A$^{\mathrm{G}}$	1.15	0.450	-0.94	1508	[4]

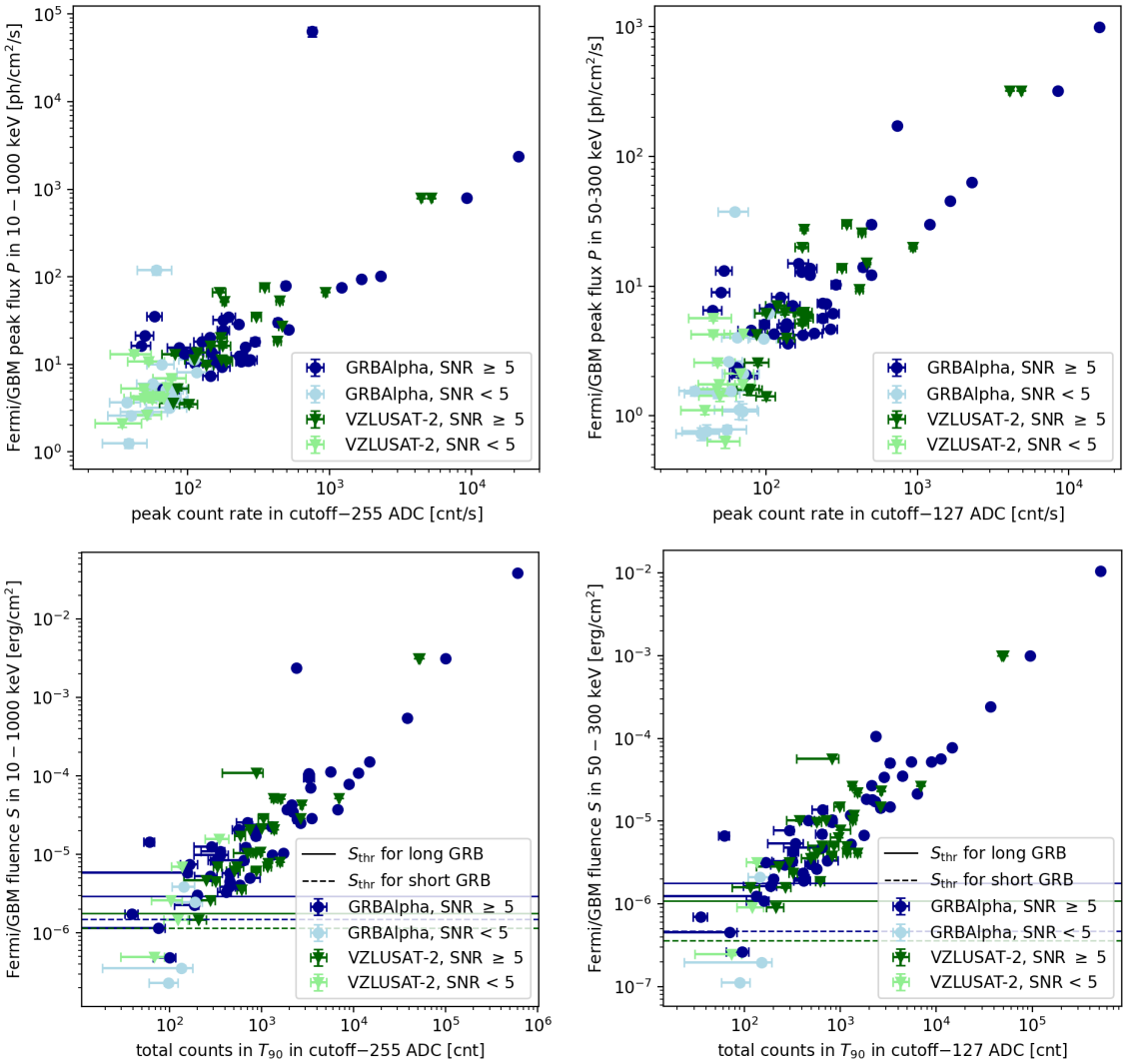

Figure 4.13: *Top:* Comparison of peak flux measured by Fermi/GBM and peak count rate measured by GRBAlpha and VZLUSAT-2 CubeSats for different energy bands. *Bottom:* Comparison of fluence measured by Fermi/GBM and total counts detected during T90 by GRBAlpha and VZLUSAT-2 CubeSats for different energy bands. The horizontal solid (dashed) lines mark the theoretical fluence of a typical long (short) GRB calculated for a threshold detection with SNR = 5. All GRBs observed by both, Fermi and GRBAlpha or VZLUSAT-2 satellites, are included in the figure. The ones shown in light color are sub-threshold detections and those shown in dark color are significant detections. The boundary between sub-threshold and significant detections represents the empirical detector sensitivity. Few GRBs fainter than the threshold were detected by the CubeSats as significant detections. These are further investigated in Sec. 4.2.2. The CubeSat data shown in the figure are subject to some undesired effects; they are not corrected for the satellite orientation, GRBAlpha and VZLUSAT-2 use different cutoff for low energies, the energy bands differ for individual detections as described in Sec. 3.1.

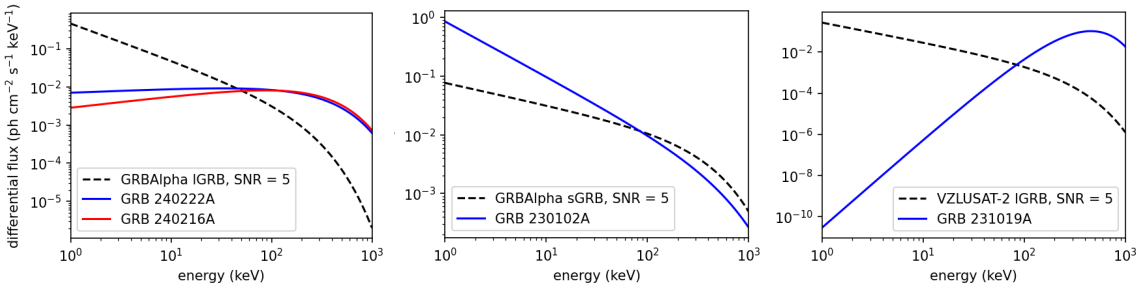

Figure 4.14: Spectra of GRBs fainter than the calculated threshold for a 5σ detection compared to the theoretical spectrum of a GRB used for calculation of the sensitivity threshold. *Left*: GRBAlpha long GRBs, *middle*: GRBAlpha short GRBs, *right*: VZLUSAT-2 long GRBs. The detection of fainter long GRBs can be explained by their harder spectra, compared to the threshold GRB, at $\sim$ 100 keV where the detectors have maximum effective area. The spectrum of the short GRB 230102A is softer than that of a typical short GRB, however, the significance of this detection was close to the 5σ threshold.

Non-detection of bright GRBs

Besides the detections themselves, it is also interesting to look at the reasons why we did not see those events that we did not see. On a polar LEO at an altitude of $\sim$ 550 km, satellites are usually exposed to the particle environment of the Earth's radiation belts around $\sim$ 40% of the time (Fig. 3.1). However, the LEO environment is very dynamic and at times of high solar activity we have observed the particle background to extend up to $\sim$ 20 degrees of latitude what dramatically decreases the duty cycle. The LEO environment thus presents one of the obstructions against more detections. Another one is the limited sky coverage of a satellite at LEO. Despite the great advantage of gamma-ray detectors being practically omnidirectional, approximately $\sim$ 30% of the sky is occulted by the Earth at a $\sim$ 550 km orbit.

To study these non-detections in more detail, we cross-correlated the times of all GBM GRBs with available data from the CubeSat missions and assembled a list of GRBs for which either of the nanosatellites has data. Subsequently, we removed those GRBs which were detected. For the rest of the sample, we manually inspected the light curves and determined the state of the background. We dropped those triggers which occurred in high background regions. For the subset of GRBs which happened in low and stable background, we further checked if the localized GRB position was not occulted by the Earth. Finally, we were left with a set of undetected GRBs which occurred in low background and were in our field of view.

Ideally, we would expect all of these GRBs to be below our detection limit. Fig. 4.15 and 4.16 compare the distributions of the peak flux and fluence of sub-threshold and significant detections with the non-detected GRBs. The division between detections and non-detections is apparent in the peak flux distributions. The overlap of the fluence distributions is more significant. For both CubeSats, 30% of the non-detections have higher fluence than the threshold value calculated in Sec. 4.2.1. All of these bright undetected GRBs belong to the long-duration group. The reason for these non-detections could be the edge-on orientation of the detector with respect to the source, for which the effec-

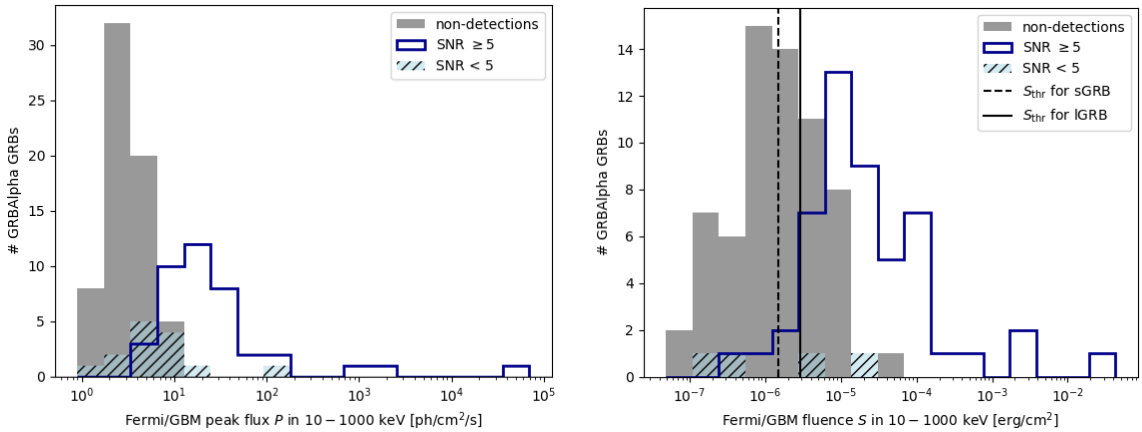

Figure 4.15: The distributions of peak flux (*left*) and fluence (*right*) measured by Fermi/GBM of all GRBs which were in GRBAlpha's field of view and happened in low background region, separated according to the detection significance. The vertical lines mark theoretical values of a threshold 5σ detection of a typical short and long GRB (Sec. 4.2.1).

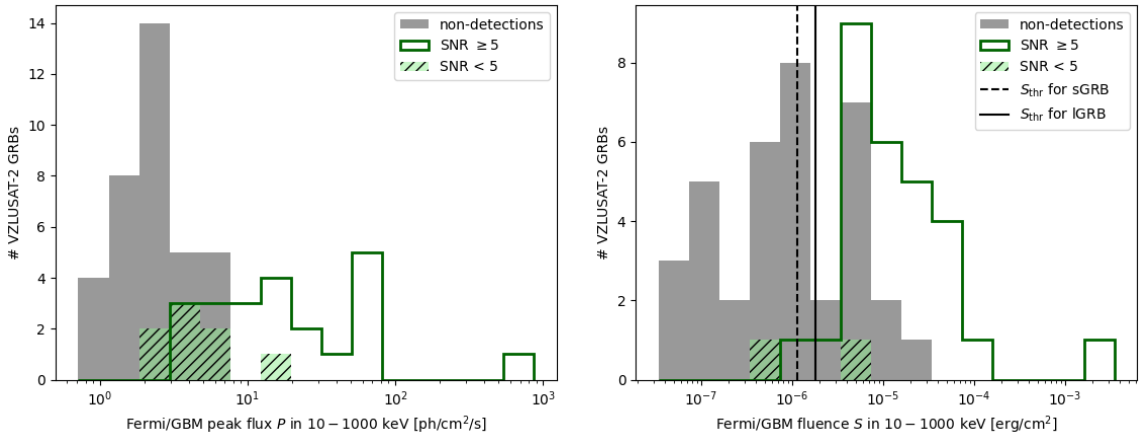

Figure 4.16: The same as Fig. 4.15 but for VZLUSAT-2.

tive area of the detector is considerably lower (Fig. 2.7). However, since we do not have the information about the orientation of GRBAlpha and the VZLUSAT-2 AOCS data is only download for confirmed detections, we cannot confirm nor reject this hypothesis. VZLUSAT-2 carries two detector units which are placed perpendicularly to each other. This suggests that the overlap of the undetected and observed GRBs should be smaller compared to GRBAlpha, because the chance of a simultaneous edge-on orientation for two detectors is much lower than for only one detector. However, VZLUSAT-2 often measures data only with one detector unit, depending on the power consumption needs of the other instruments on-board.

Detectivity of gamma-ray bursts

Fig. 4.17 shows the faintest sub-threshold and significant GRBs detected by GRBAlpha and VZLUSAT-2 plotted over the CCDF of the peak flux and fluence of Fermi/GBM

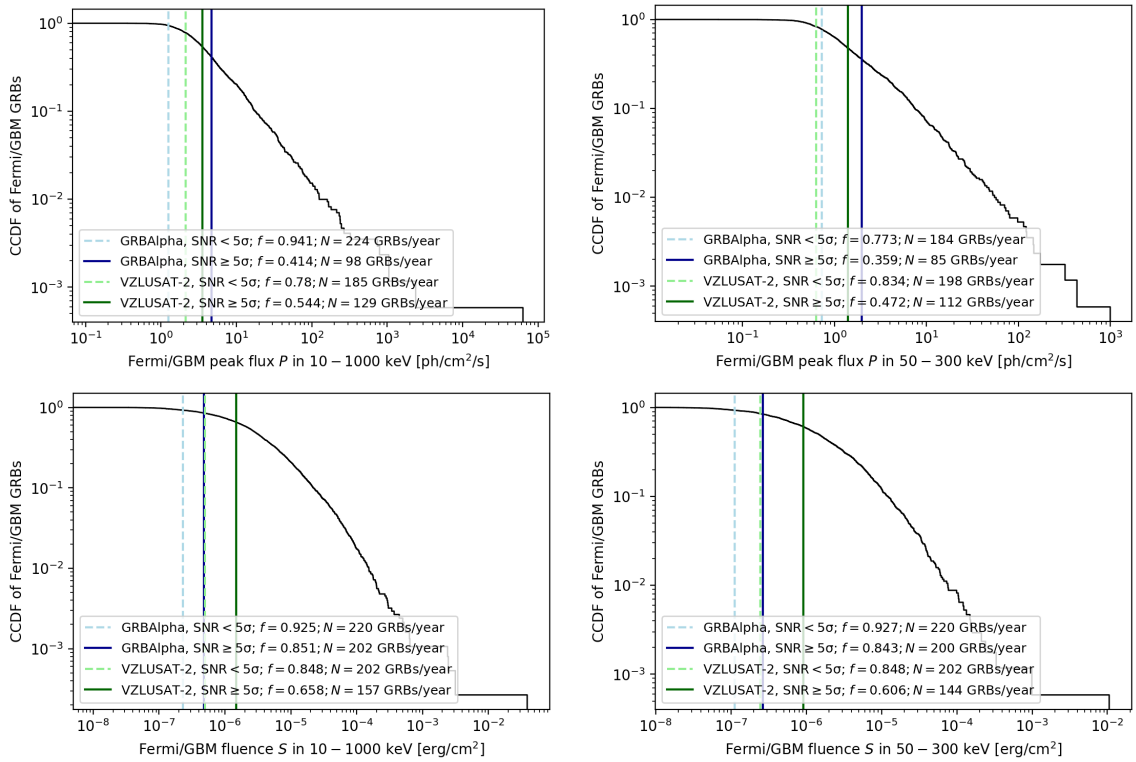

Figure 4.17: Complementary cumulative distribution functions of the peak flux (top) and fluence (bottom) of all GRBs detected by Fermi/GBM. The black curve marks the normalized number of GBM GRBs with peak flux or fluence higher than or equal to the given value. The vertical solid lines mark the faintest GRBs detected by GRBAlpha and VZLUSAT-2 with SNR ≥ 5. The vertical dashed lines mark the faintest events detected by the CubeSats with SNR < 5. In the legends, f is the fraction of GRBs brighter than the marked value and N is the number of GRBs which would be detected per year with this sensitivity, derived from the yearly detection rate of GBM.

GRBs. The faintest GRB detected by GRBAlpha with SNR$\geq 5\sigma$ belongs to 15% of the faintest GRBs observed by GBM. This suggests that the detector should be able to see all of the brighter 85%. However, this faintest GRB detection is the long GRB 240222A which, as discussed earlier, was harder compared to a typical long GRB (Fig. 4.14). The faintest GRB detected significantly by VZLUSAT-2 is located at 65% of the CCDF. The fact that the value is lower than the faintest GRBAlpha GRB can be simply explained by GRBAlpha's luck. If VZLUSAT-2 was taking measurements at that time and was in the same location as GRBAlpha, there is no reason why it should not observe this GRB. With more detections, the empirical sensitivity of VZLUSAT-2 is expected to increase.

When looking at sub-threshold detections, the empirical sensitivity in terms of what fraction of GBM GRBs could be observed by our detector exceeds 90%. While this is very impressive considering the much smaller effective area of our detector compared to that of GBM, the sub-threshold detections were confirmed by cross-correlation with the light curves observed by GBM and other missions and due to their low significance they would most likely not be triggered by an automatic trigger algorithm on-board. Therefore, the estimated ability to detect 85% of GBM GRBs is more realistic.

Conclusions

This work studies astrophysical gamma-ray transients observed by two nanosatellite missions; GRBAlpha and VZLUSAT-2. The main results can be divided into two sections. In the first part, we present a catalogue of transients detected during the first ~ 3 years of GRBAlpha and ~ 2 years of VZLUSAT-2 operations. The second part is dedicated to a detailed study of the detector sensitivity.

The catalogue (Sec. 4.1) includes 198 gamma-ray transients, specifically, 17 short and 95 long gamma-ray bursts (GRBs), 79 solar flares, six flashes from two different magnetars known as soft gamma repeaters (SGR), and one outburst from an X-ray binary. Individual transient types are clearly separated in the $HR - T_{90}$ plane (Fig. 4.3). GRBs are hard with a bimodal duration distribution and the soft region is occupied by the long solar flares and very short SGRs. The distribution of the peak flux is similar for all types of transients and the distribution of measured fluence follows that of the T_{90} duration (Fig. 4.7). The distributions for individual solar flare classes (Fig. 4.8) reveal that while higher-class flares last longer and are brighter in soft gamma-rays, their hardness ratio is uniform among the individual classes. This result can be biased by background fluctuations because most solar flares were only observed in the lowest energy band.

Some notable detections are (Sec. 4.1.3):

- GRB 231215A is the most distant GRB, localized at z = 2.305. This is equivalent to a look-back time of 10.8 Gyr for a 1U CubeSat.
- The shortest time interval between two subsequent detections was 42 minutes between GRB 230709B and GRB 230709C. This demonstrates the capability of nanosatellites to routinely detect GRBs.
- GRBAlpha observed the brightest-of-all-time (BOAT) GRB 221009A and thanks to the small detector size it provided an unsaturated measurement of its peak flux. Both CubeSats also observed the second brightest GRB 230307A.
- An X6 class solar flare on February 22, 2024 was at its peak nearly as bright as the BOAT while its fluence was $1000\times$ higher than the fluence of an average detection. Interesting is also its detection in the highest energy band where detection of any transient type is extremely rare.

The sensitivity study was done by theoretical calculations of fluence for a 5σ detection of a typical GRB (Sec. 4.2.1) and by cross-correlating our detections with GRBs observed by Fermi/GBM (Sec. 4.2.2). The calculated theoretical fluence implies a feasible detectivity of $\sim 60\%$ of long and $\sim 80\%$ of short GBM GRBs (Fig. 4.12). Three GRBs

significantly (SNR$\geq$ 5) detected by GRBAlpha and one by VZLUSAT-2 fall below the theoretical threshold. We find that their spectra were harder than the spectrum of a typical GRB (Fig. 4.14) what can explain our significant detections. We also find that 30% of GRBs which were not detected but occurred in the satellites' field of view while they were in a low-background region have fluence higher than the theoretical threshold value (Fig. 4.15 and 4.16). A potential explanation for these non-detections is an edge-on orientation of the detector with respect to the source, however, we cannot reject nor confirm this hypothesis because we do not have the attitude information. The faintest GRB observed significantly by the CubeSat missions is the GRB 240222A which belongs to the 15% of the faintest GBM GRBs. This suggests that the detector should be able to see 85% of the brightest GBM GRBs. However, the spectrum of this event was harder than that of a typical long GRB, therefore, the real sensitivity is likely lower. Nevertheless, it demonstrates that the detector sensitivity is high for harder events which are usually short GRBs, the electromagnetic counterparts to gravitational waves.

The observed detection rate (Sec. 4.1.1) of GRBAlpha during non-stop observations is two transients per week, out of which one is a GRB. Extrapolating for a constellation of similar satellites which would provide an all-sky coverage from low-background region, we estimate a yearly detection of $\sim$ 250 transients, at least half of which would be GRBs. VZLUSAT-2 on average observes one transient in ten days. The lower number compared to GRBAlpha is due to irregular measurements done by the GRB detectors on-board.

The author of this work is actively involved in operating the GRBAlpha satellite, routine search for interesting events in the acquired data, and announcing new detections to the astrophysical community via GCN Circulars[3]. A list of all published GCN Circulars and co-authored publications can be found in Appendix B.

[3] https://gcn.nasa.gov/circulars

Appendix A

Catalogue of detected transients

Light curves of all detected transients by the gamma-ray detectors on-board GRBAlpha and VZLUSAT-2 are presented on the following pages.

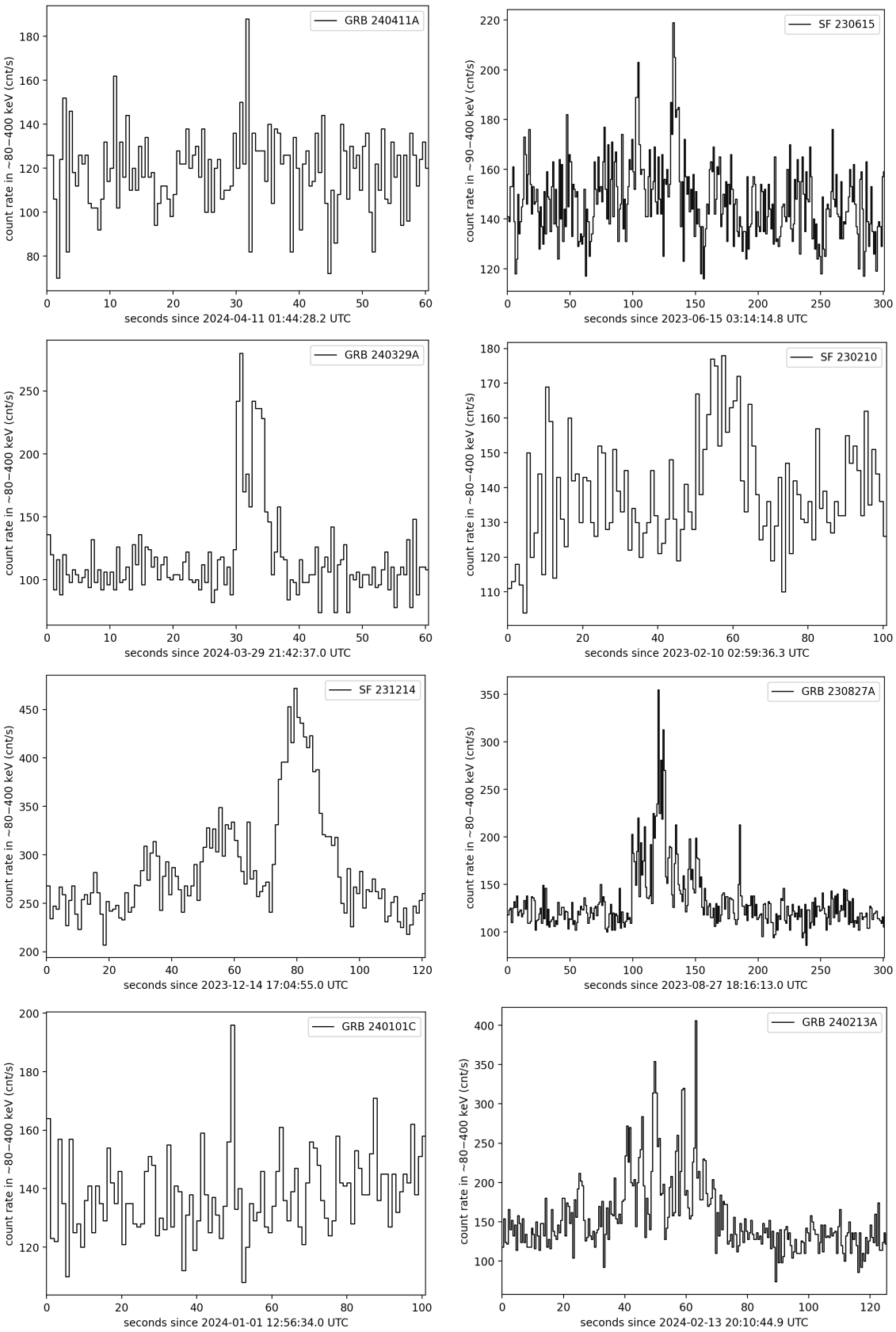

Figure 4.18: Light curves of transients detected by GRBAlpha.

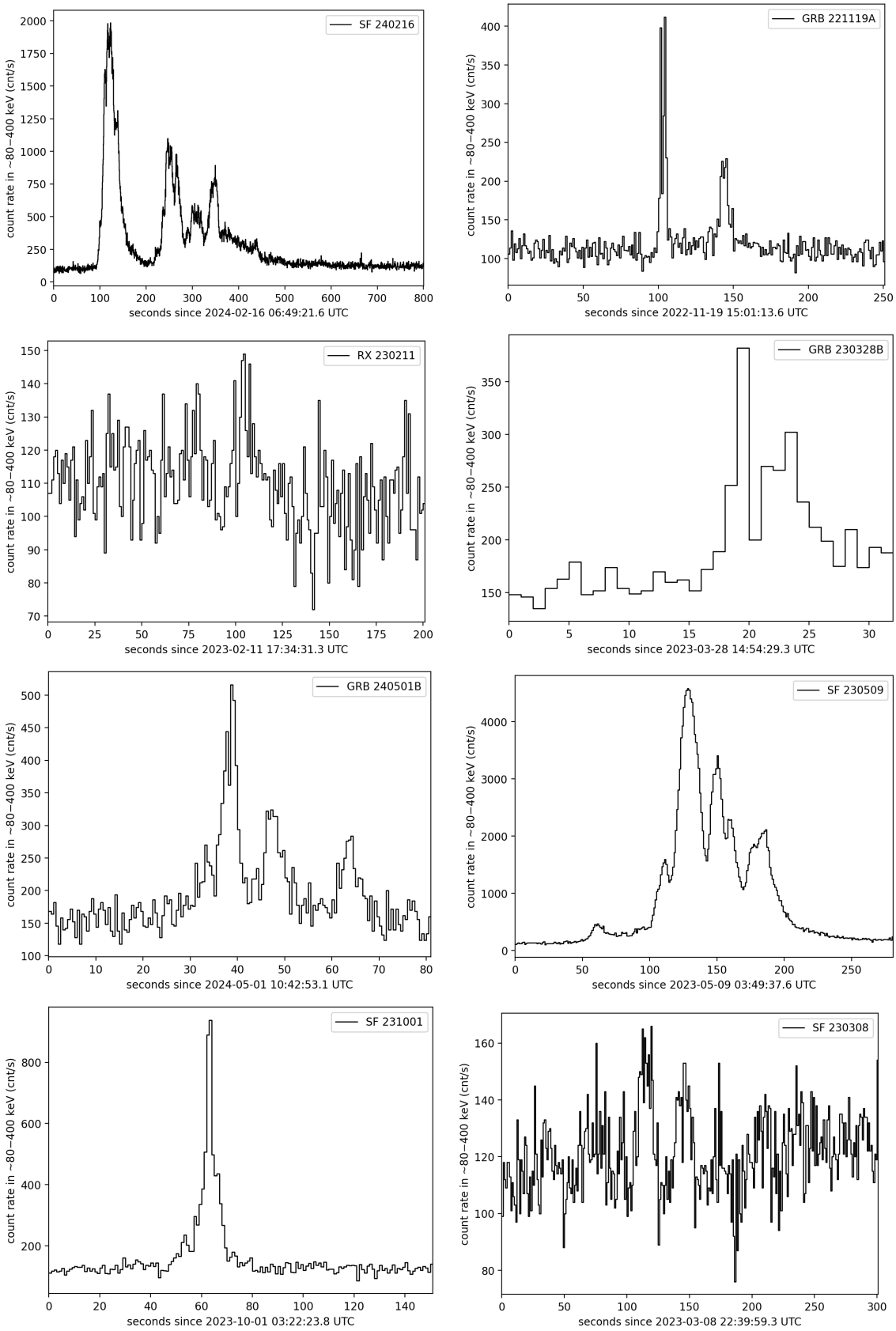

Figure 4.18: Light curves of transients detected by GRBAlpha.

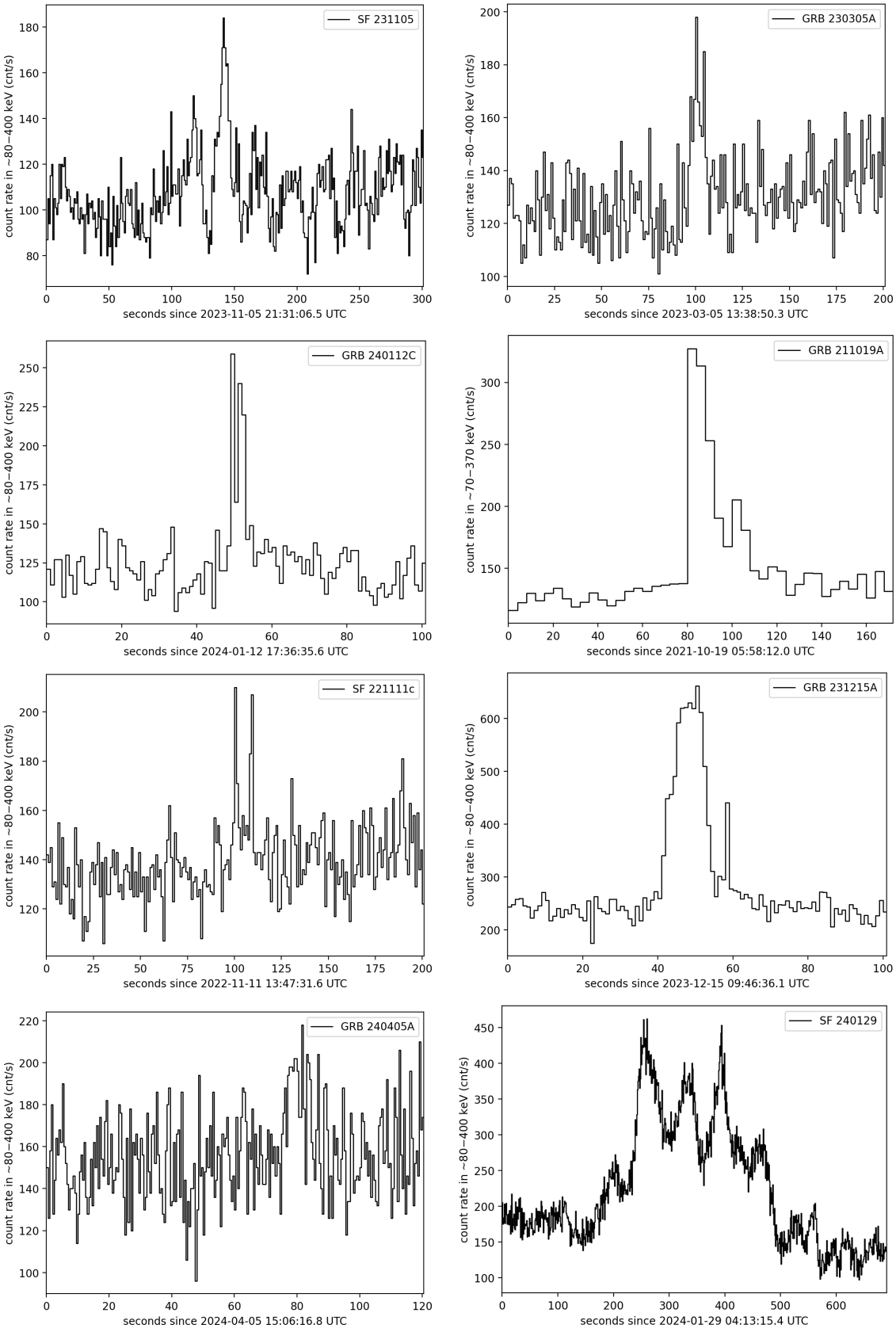

Figure 4.18: Light curves of transients detected by GRBAlpha.

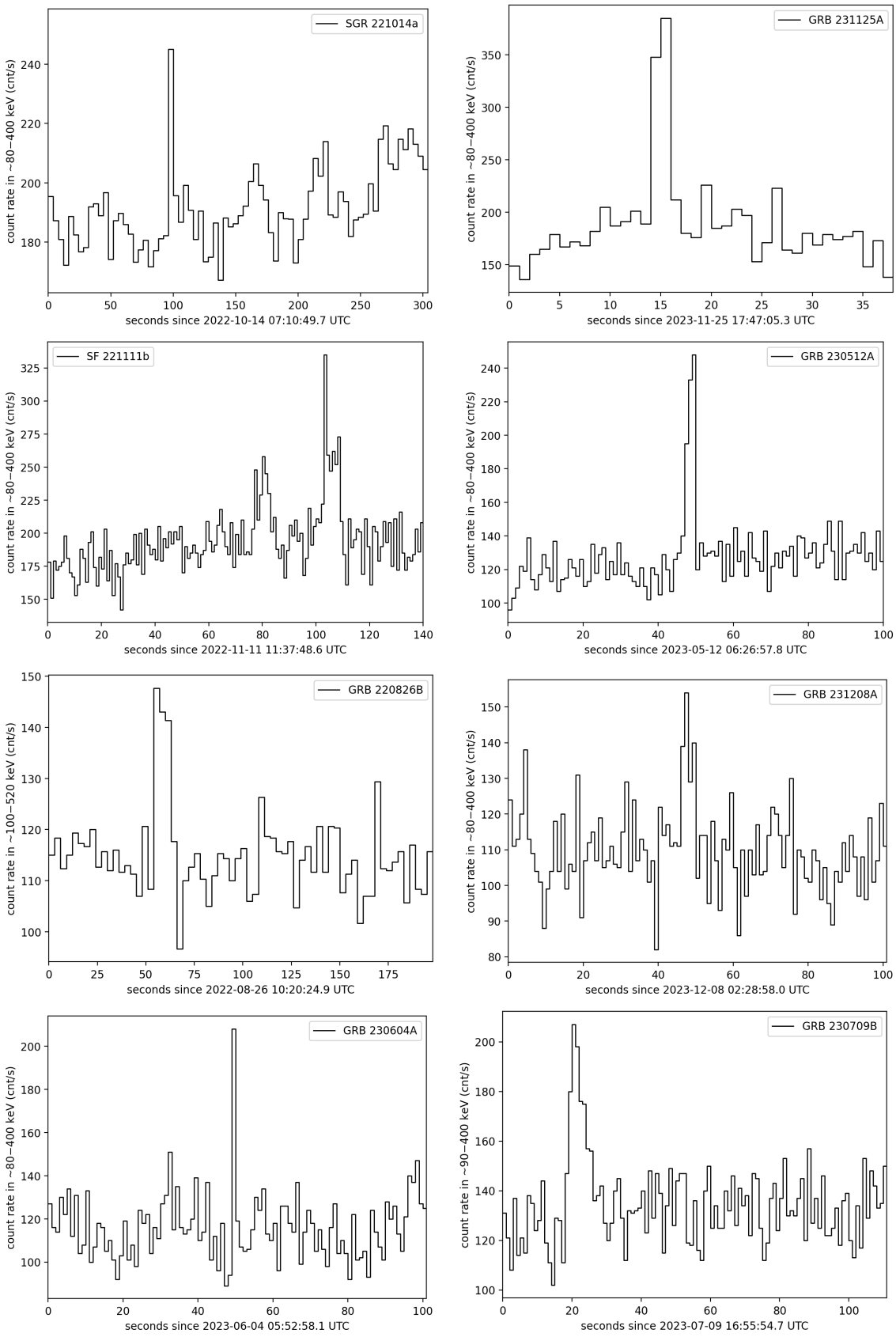

Figure 4.18: Light curves of transients detected by GRBAlpha.

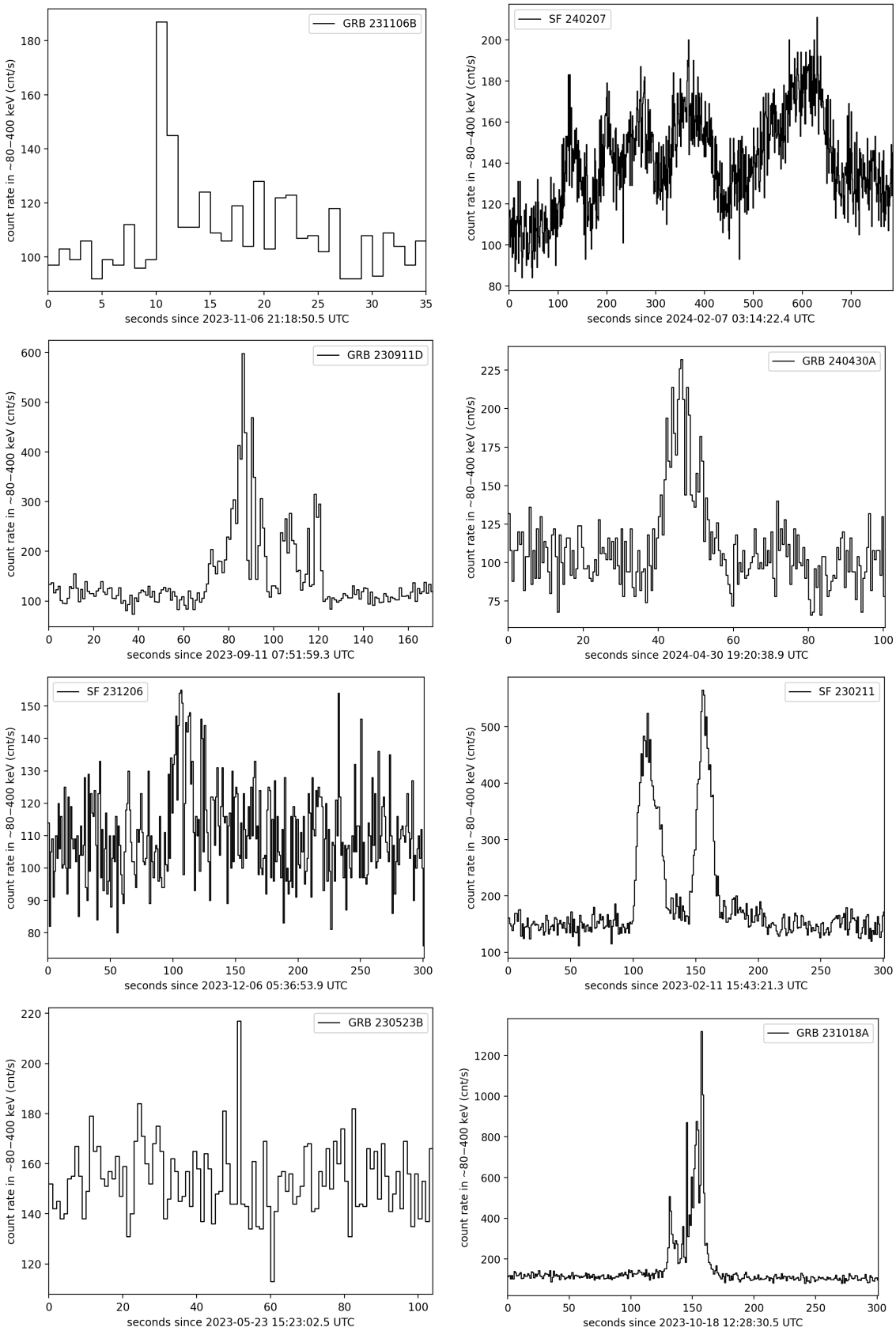

Figure 4.18: Light curves of transients detected by GRBAlpha.

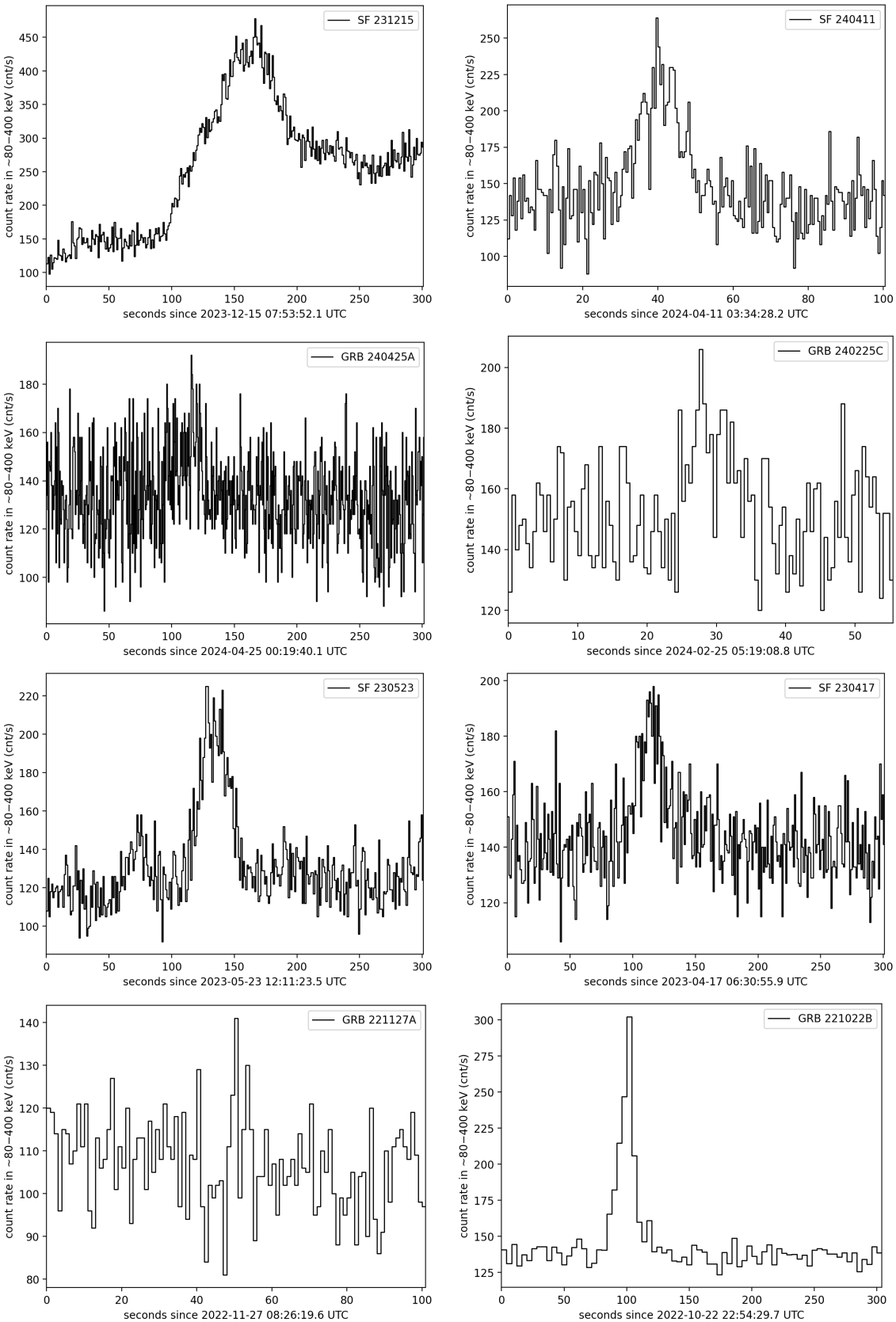

Figure 4.18: Light curves of transients detected by GRBAlpha.

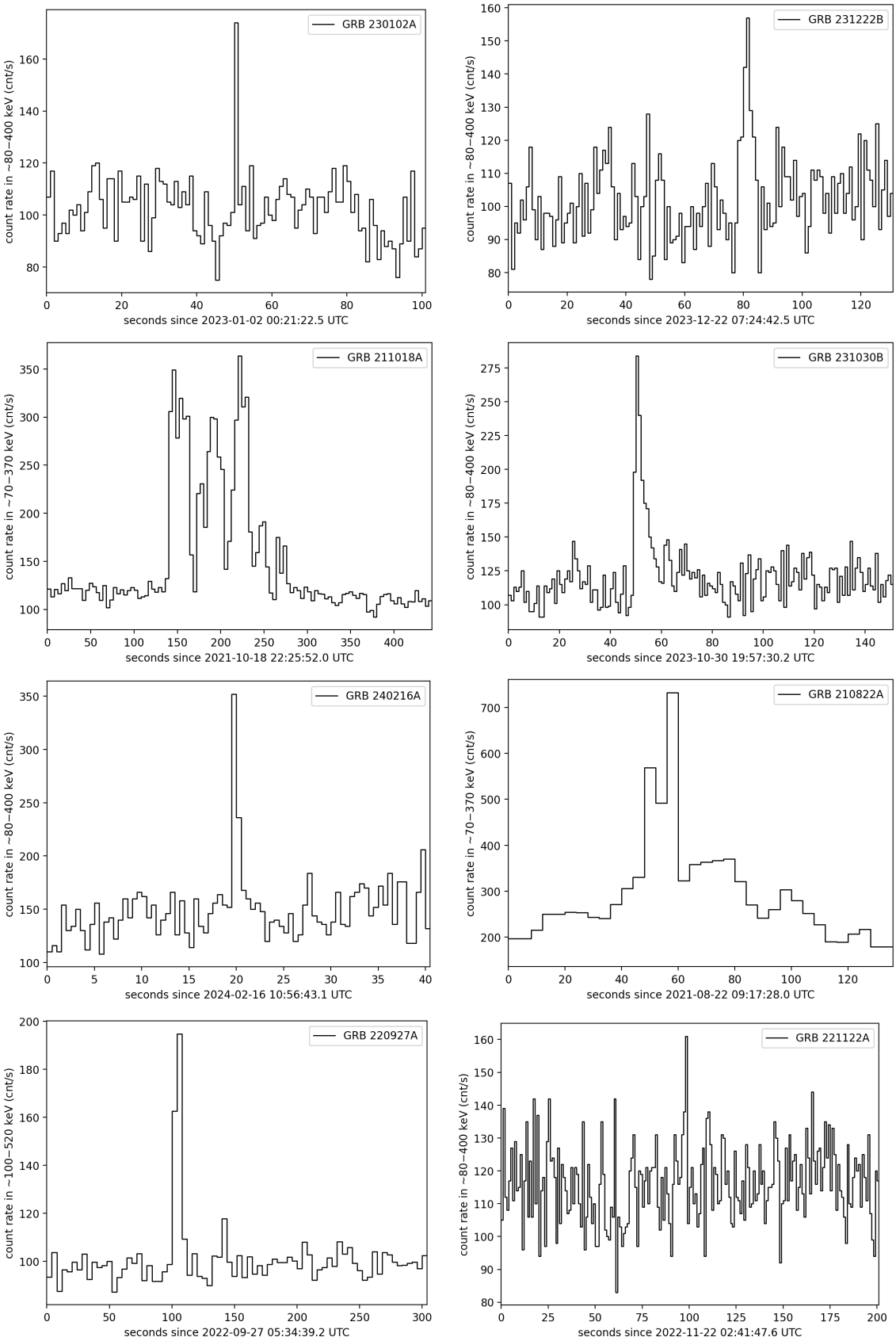

Figure 4.18: Light curves of transients detected by GRBAlpha.

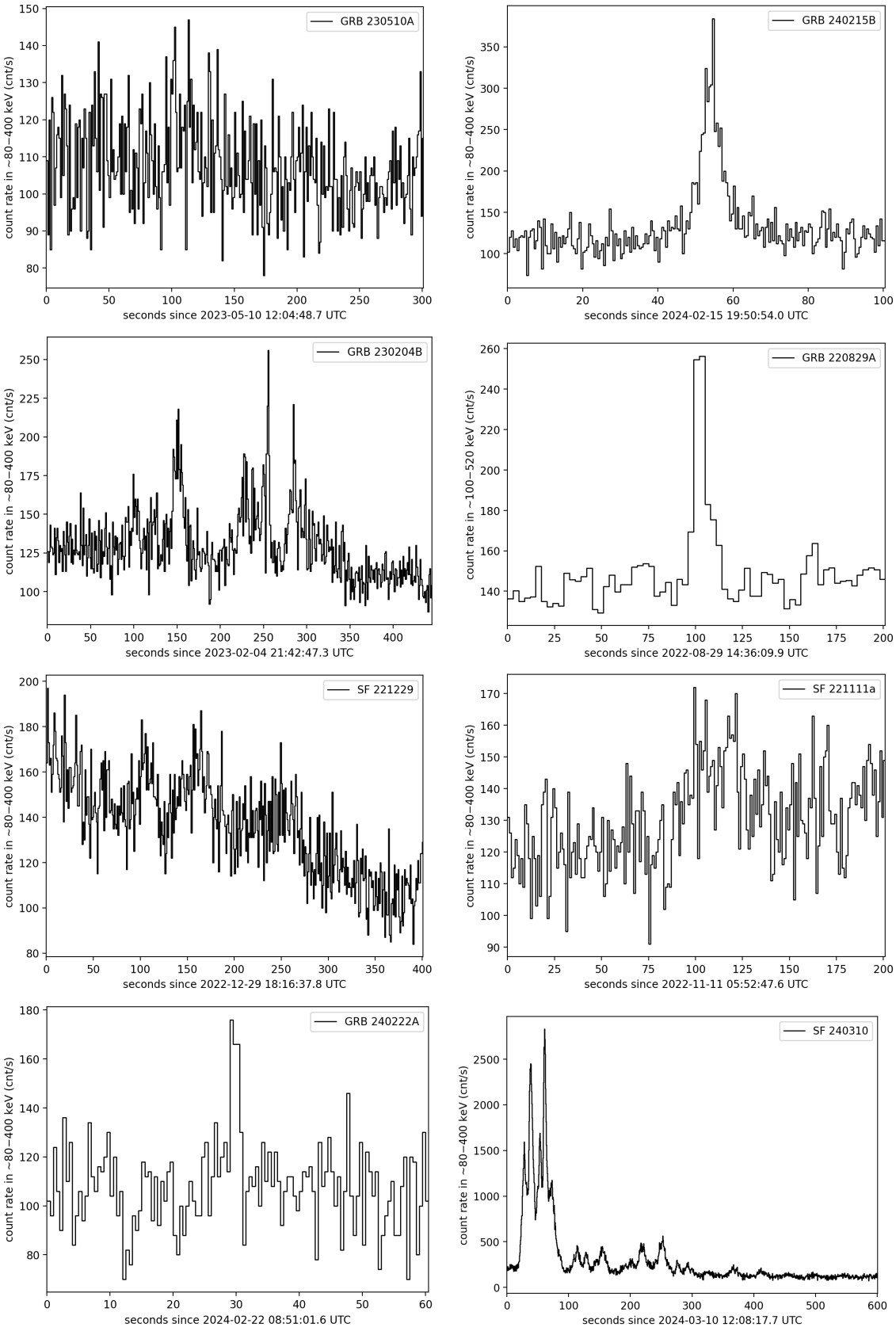

Figure 4.18: Light curves of transients detected by GRBAlpha.

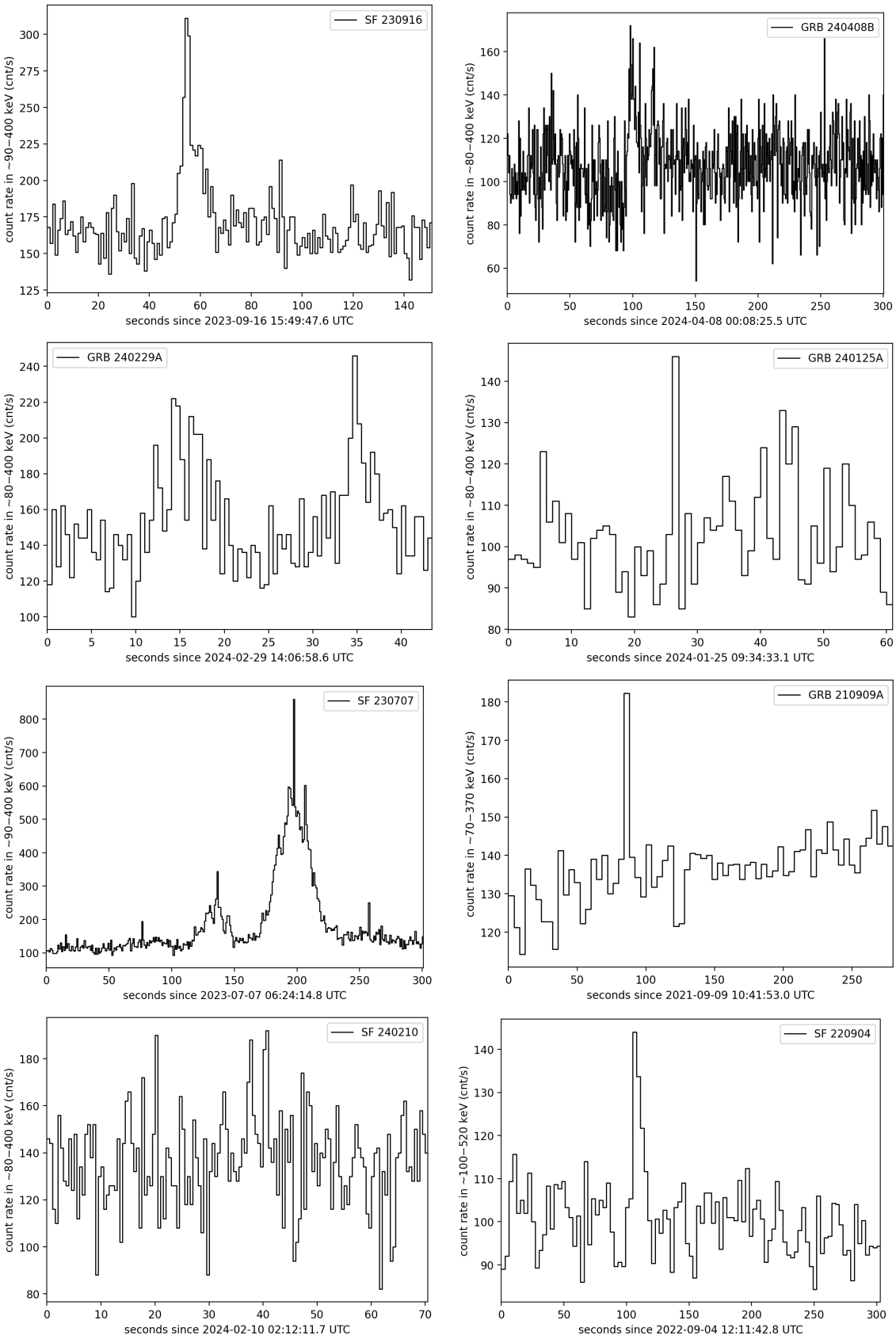

Figure 4.18: Light curves of transients detected by GRBAlpha.

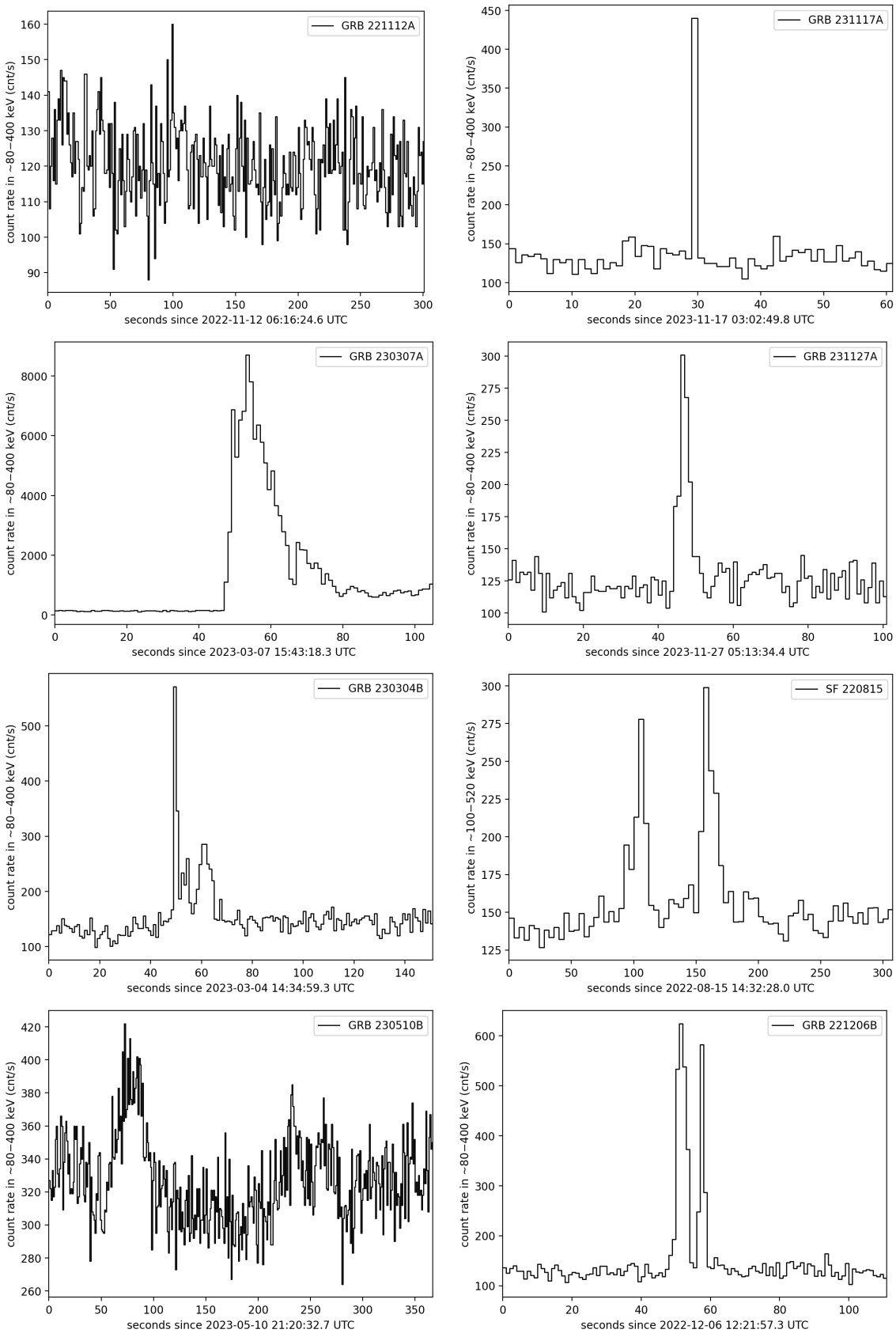

Figure 4.18: Light curves of transients detected by GRBAlpha.

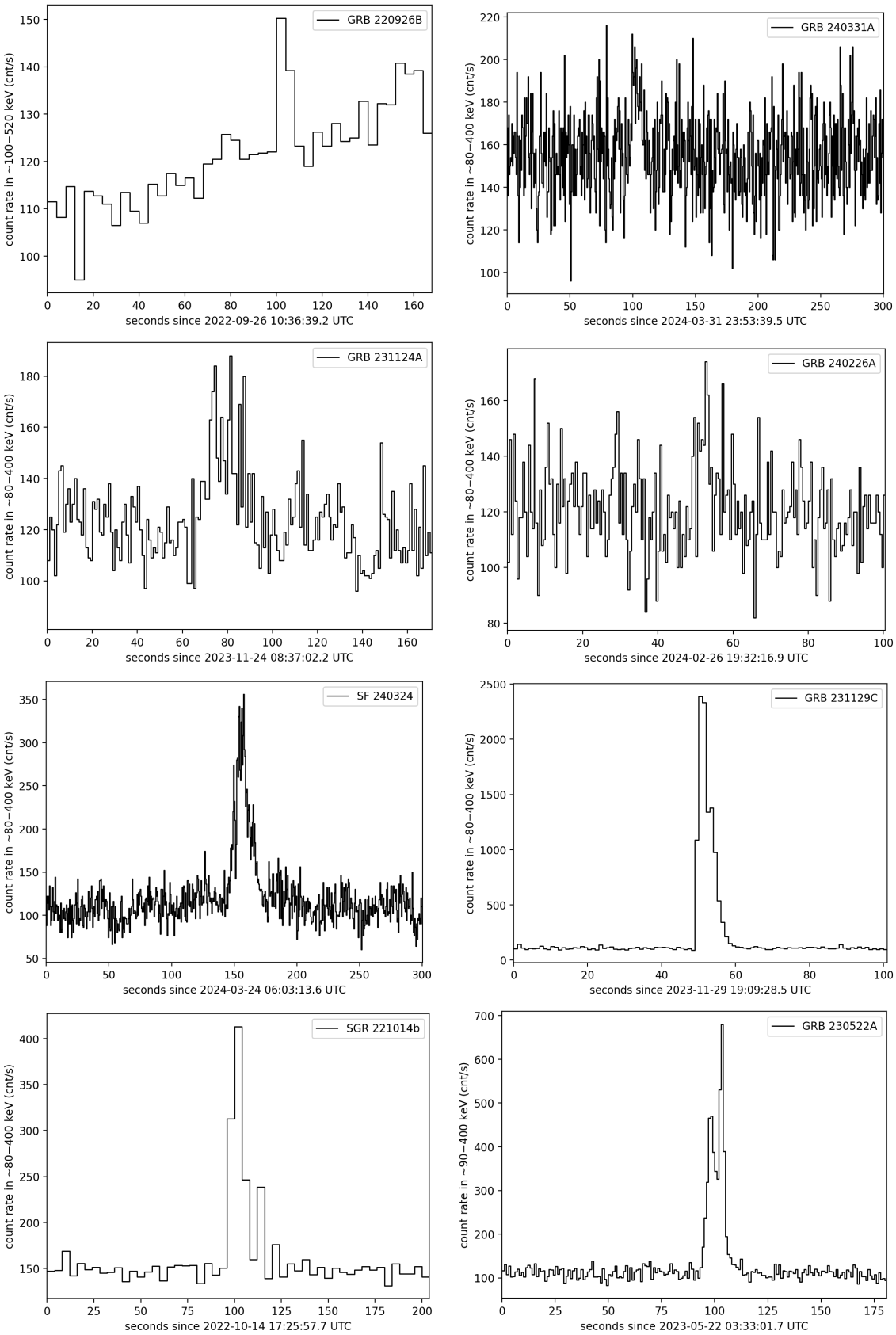

Figure 4.18: Light curves of transients detected by GRBAlpha.

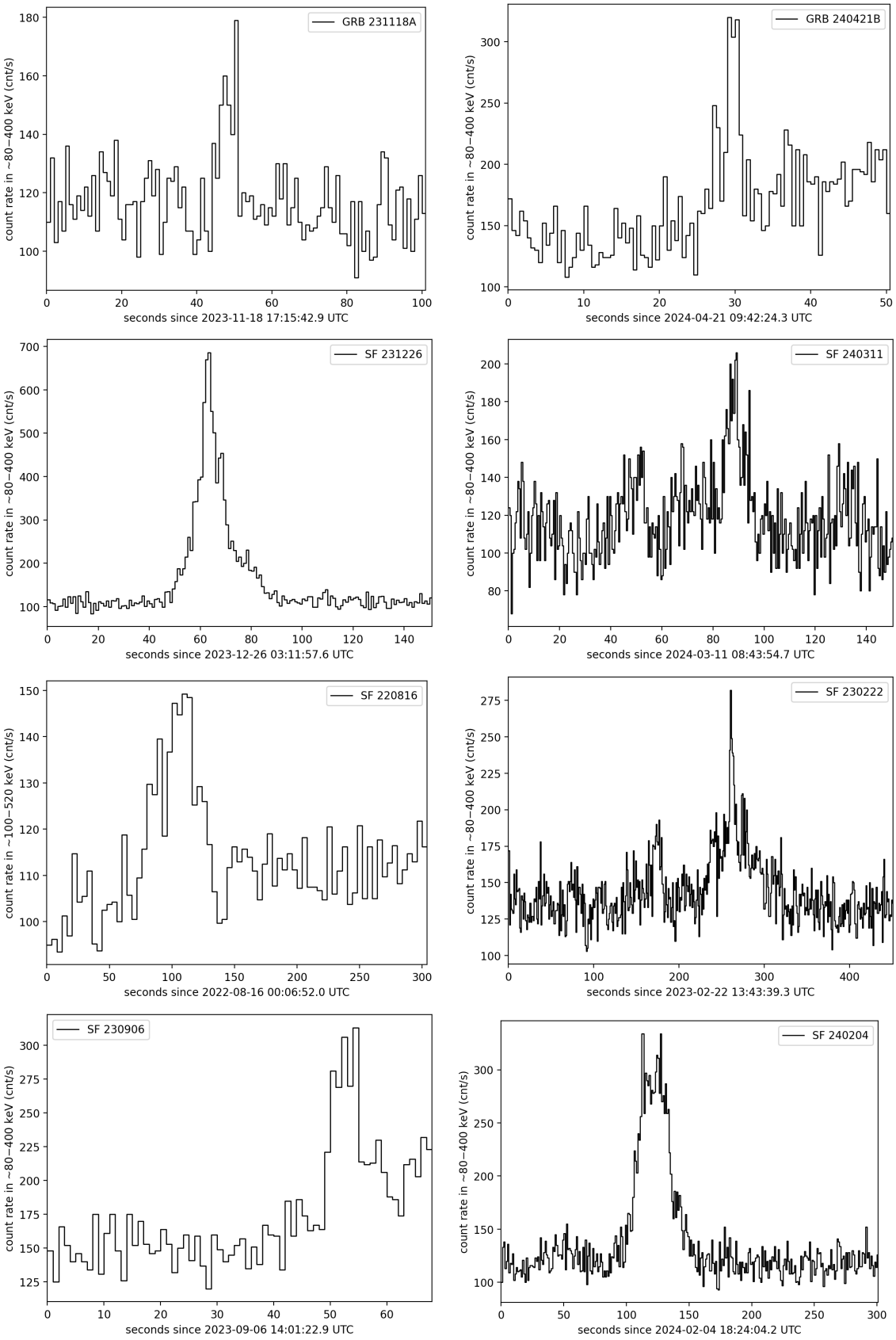

Figure 4.18: Light curves of transients detected by GRBAlpha.

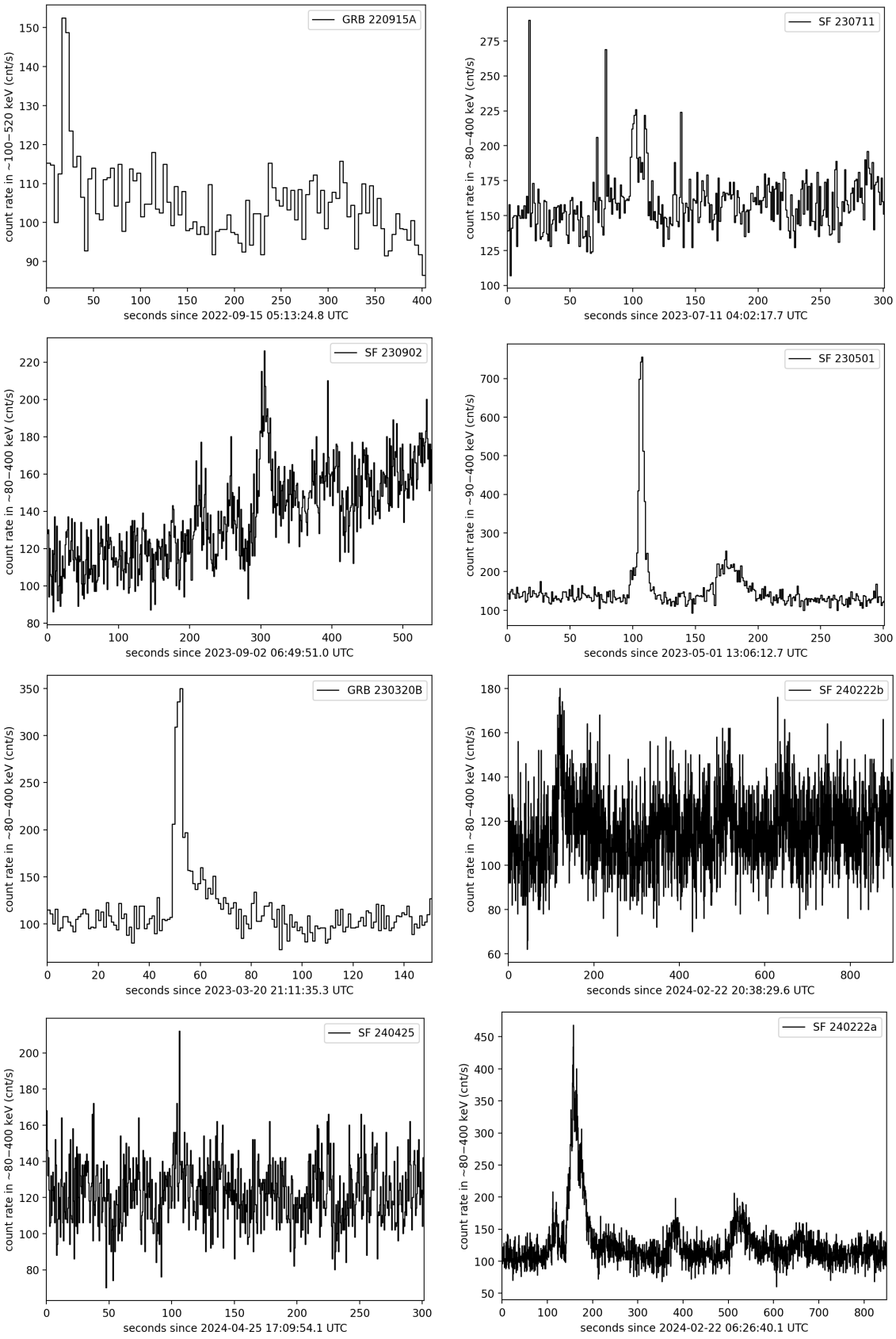

Figure 4.18: Light curves of transients detected by GRBAlpha.

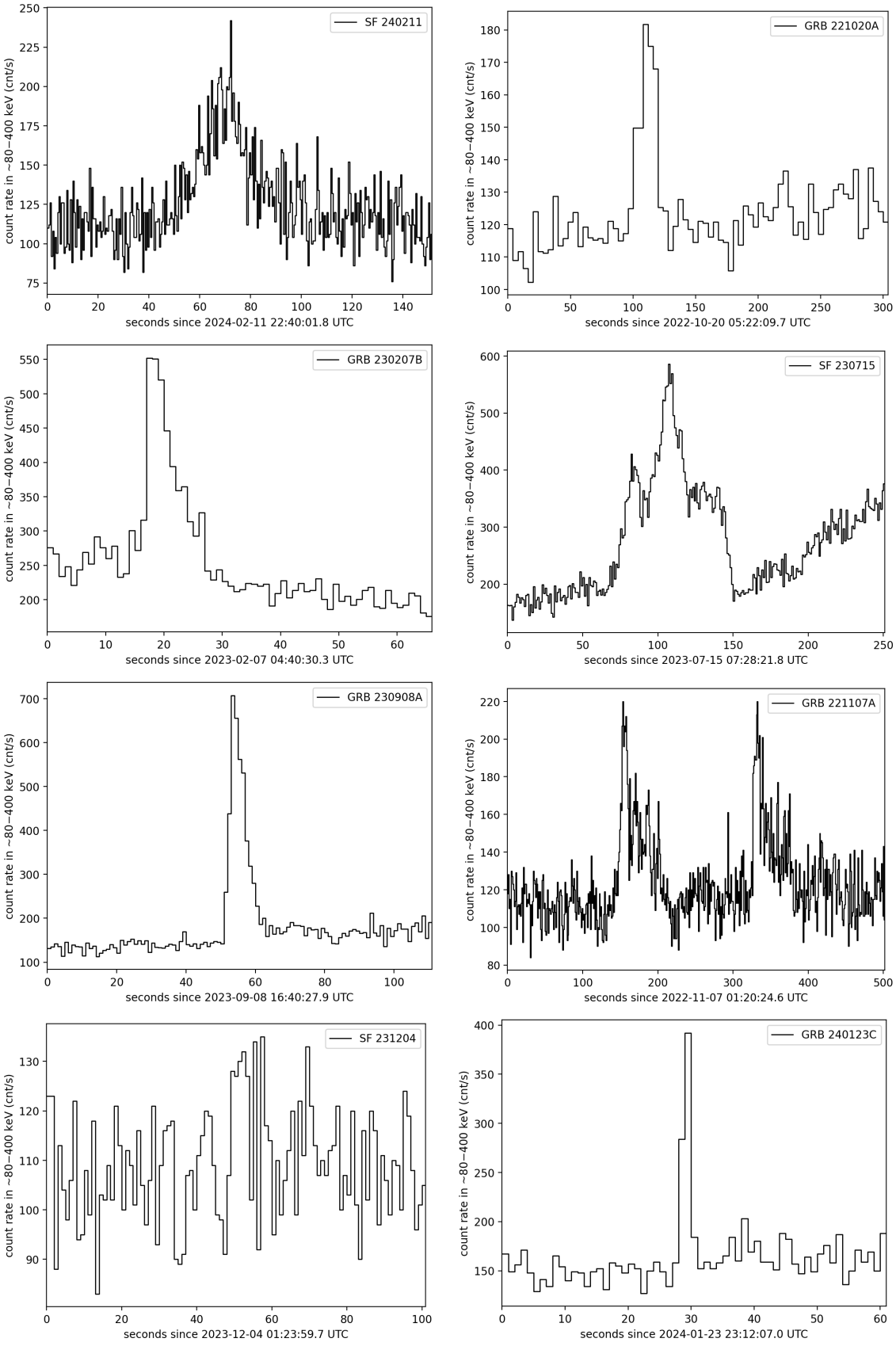

Figure 4.18: Light curves of transients detected by GRBAlpha.

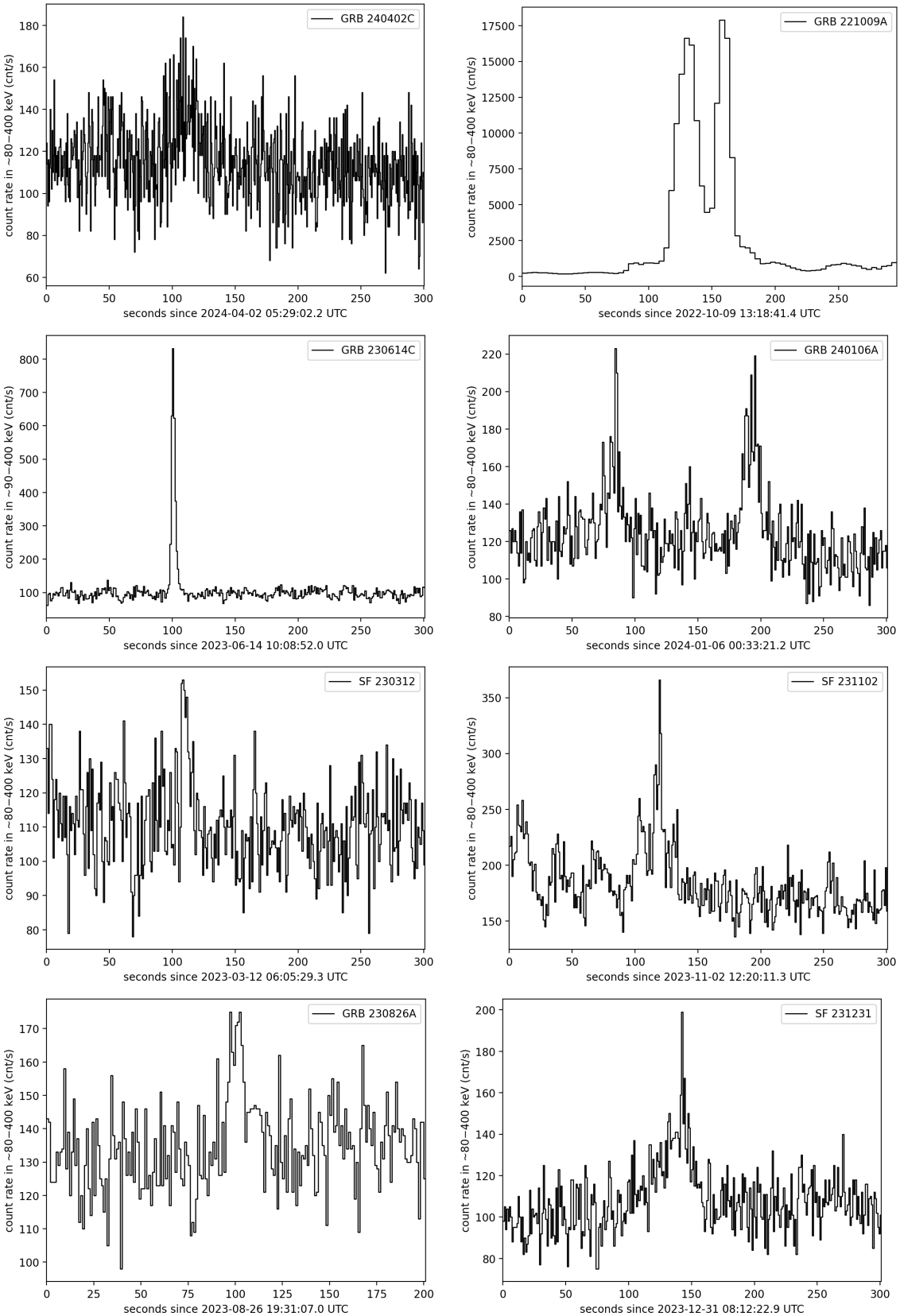

Figure 4.18: Light curves of transients detected by GRBAlpha.

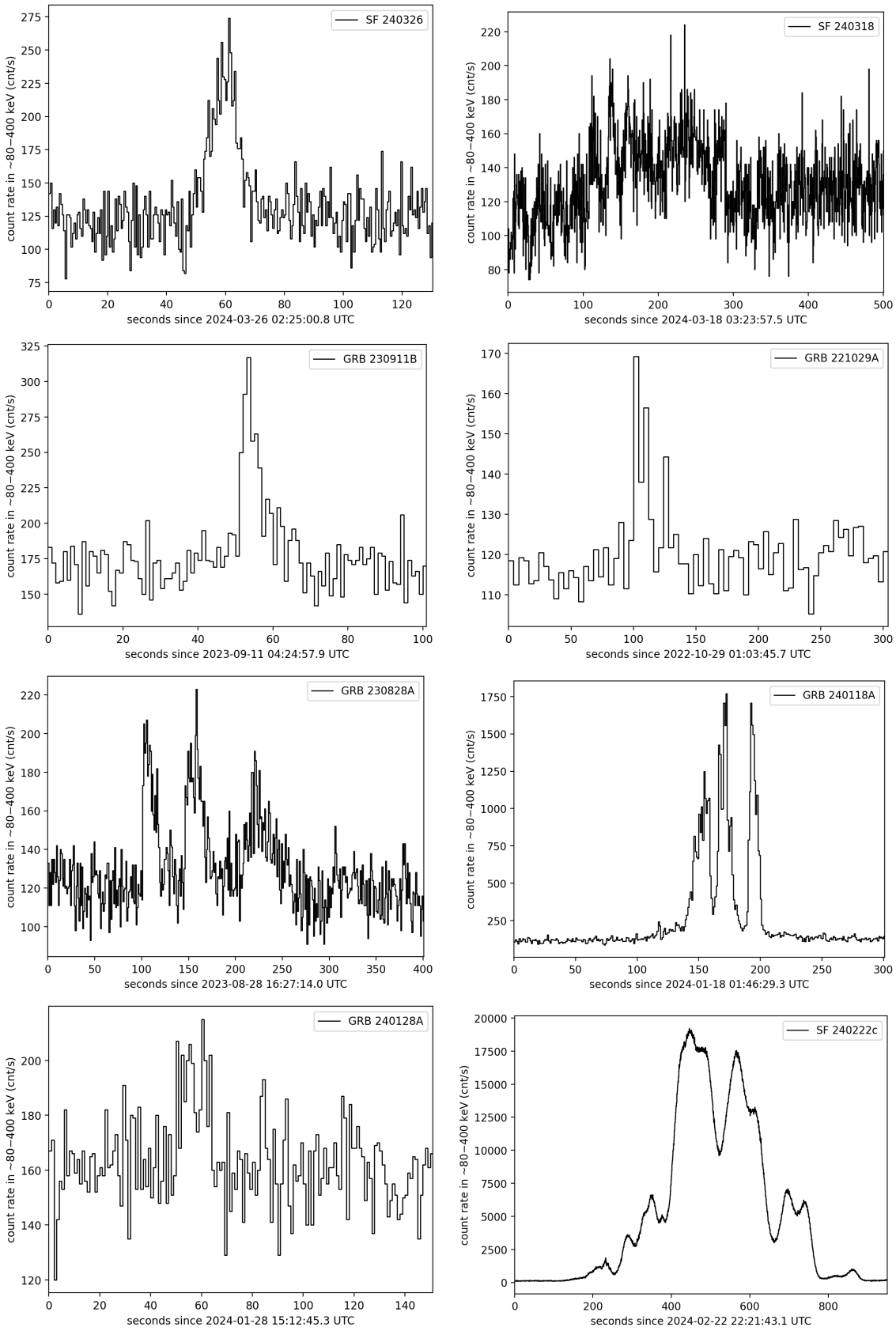

Figure 4.18: Light curves of transients detected by GRBAlpha.

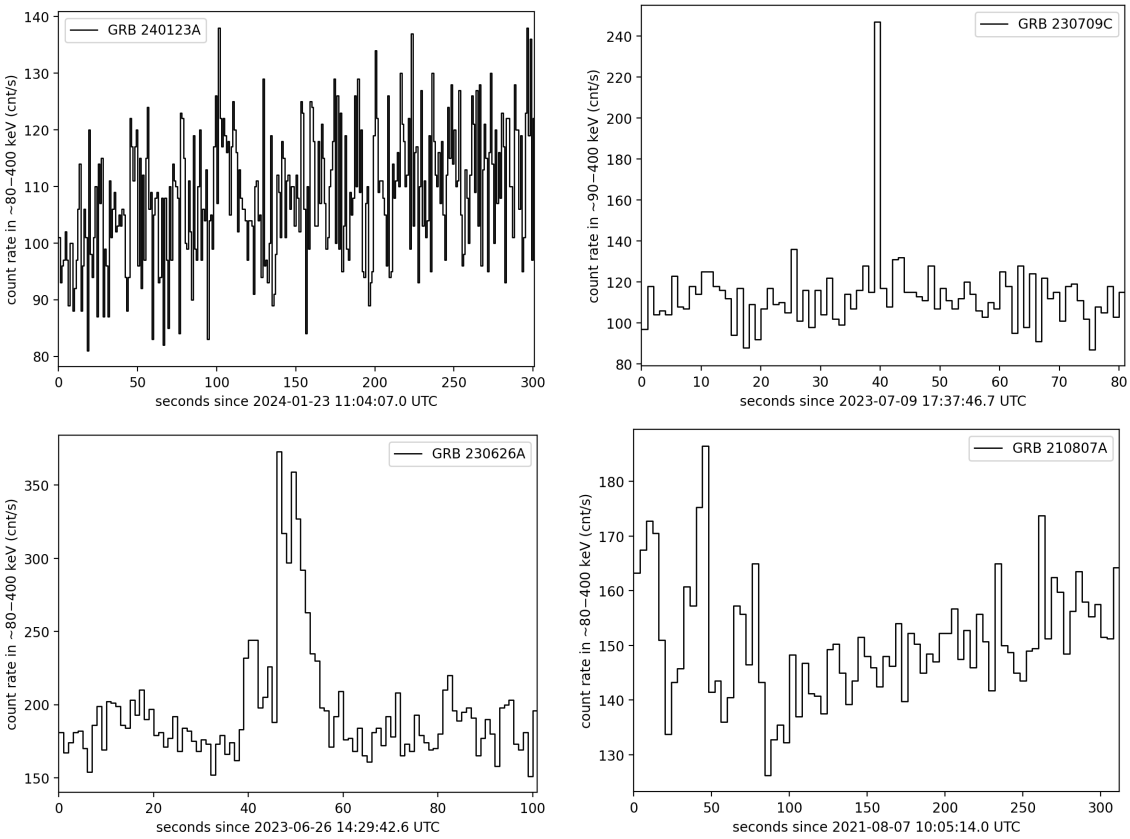

Figure 4.18: Light curves of transients detected by GRBAlpha.

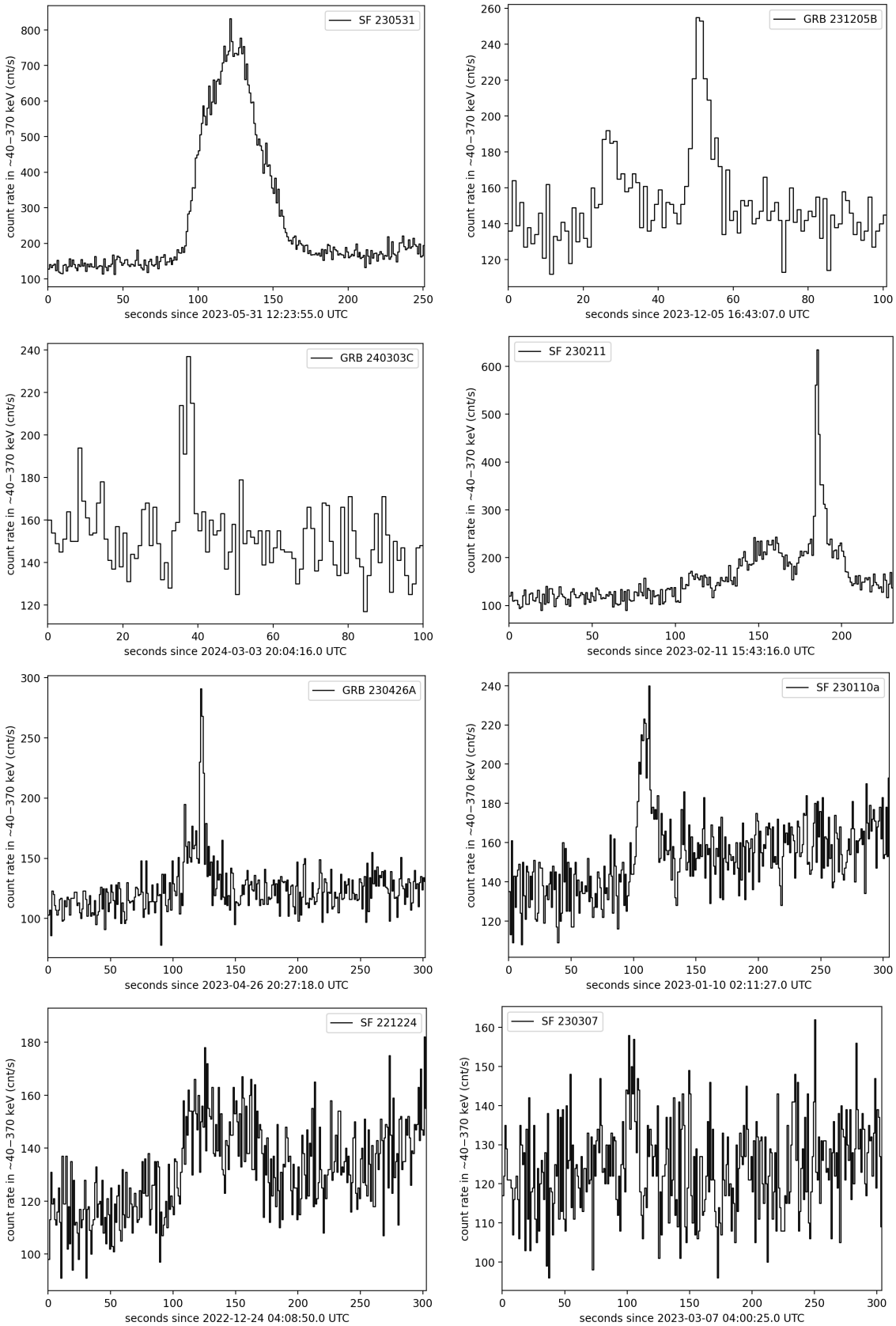

Figure 4.19: Light curves of transients detected by the detector unit 0 on-board VZLUSAT-2.

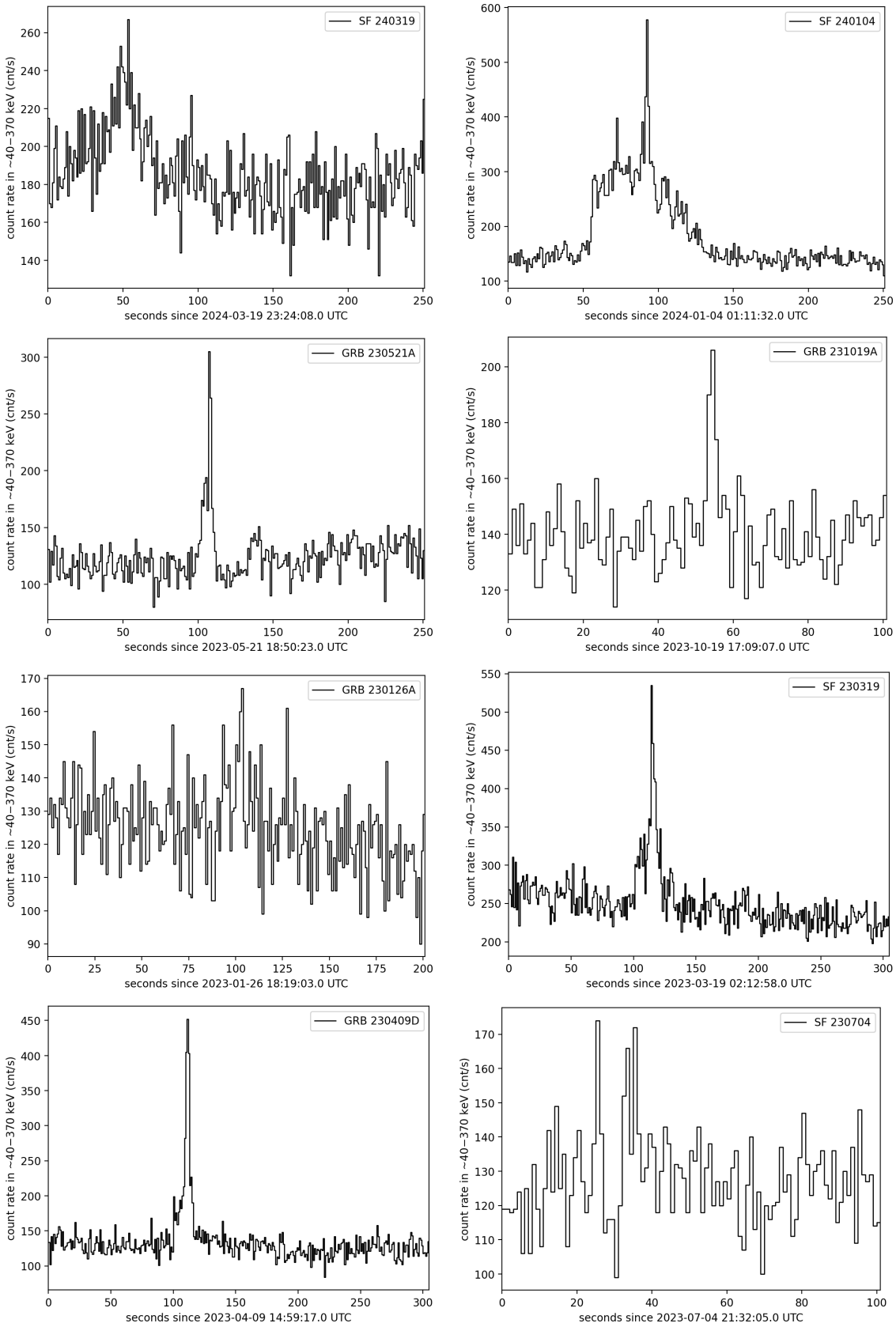

Figure 4.19: Light curves of transients detected by the detector unit 0 on-board VZLUSAT-2.

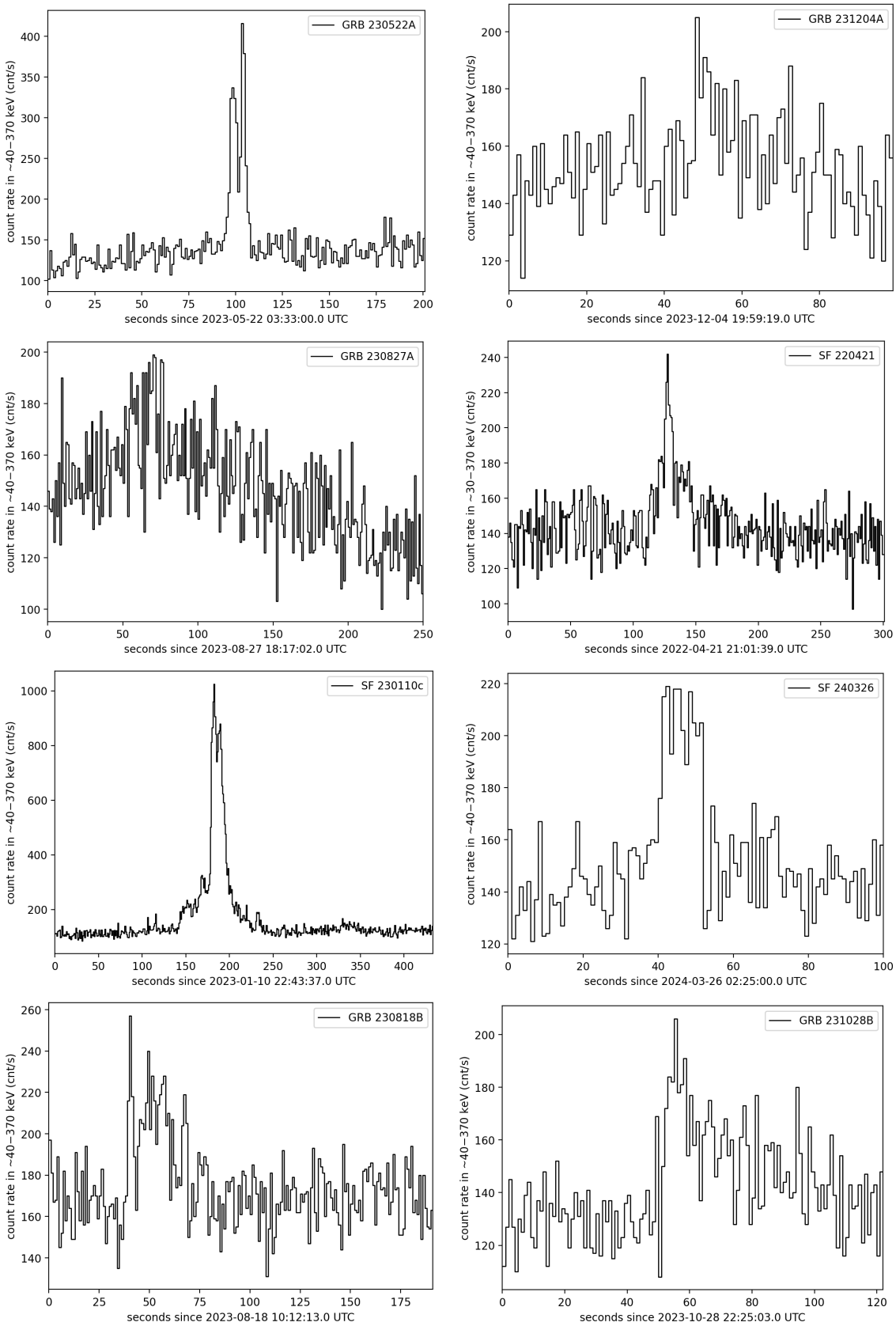

Figure 4.19: Light curves of transients detected by the detector unit 0 on-board VZLUSAT-2.

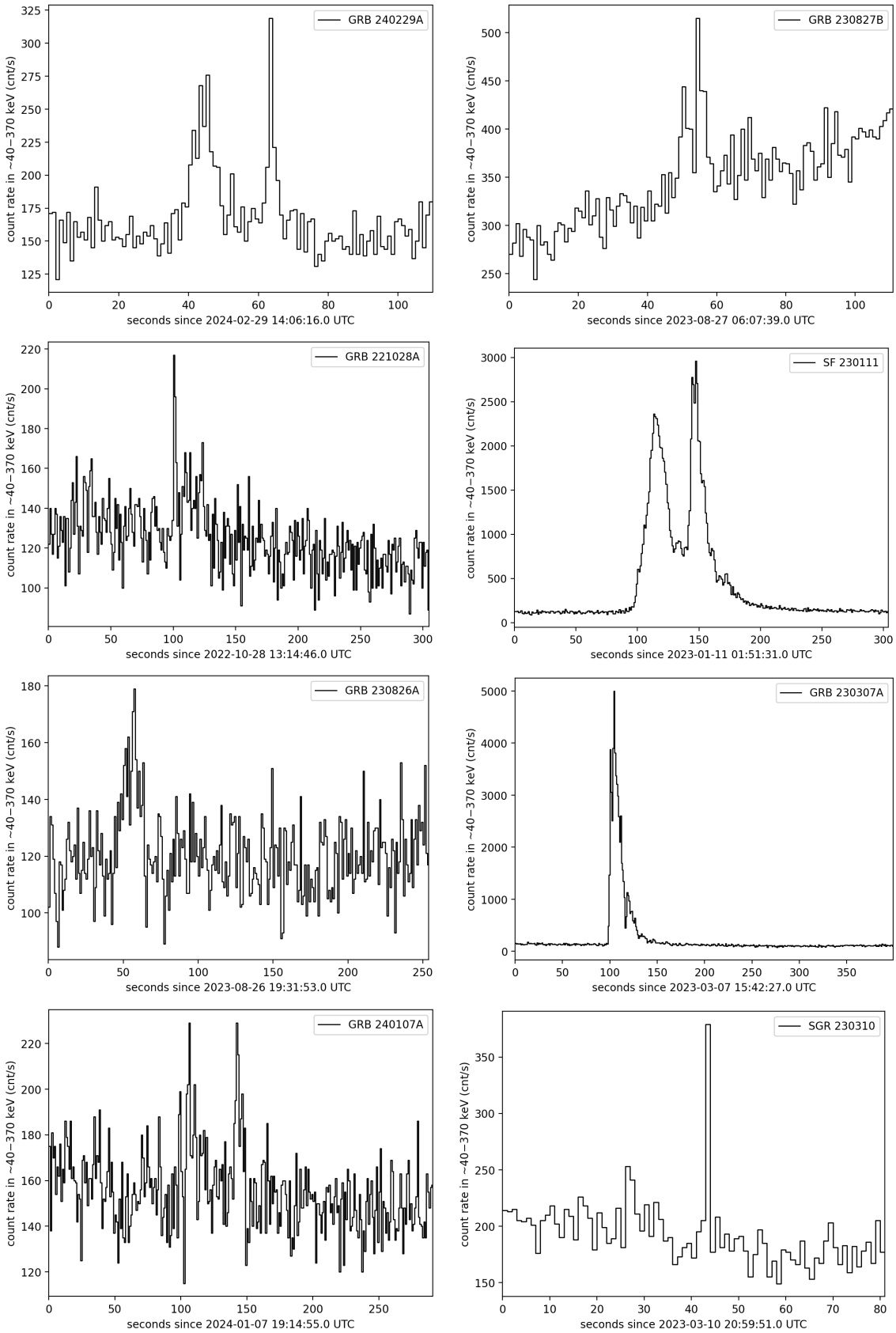

Figure 4.19: Light curves of transients detected by the detector unit 0 on-board VZLUSAT-2.

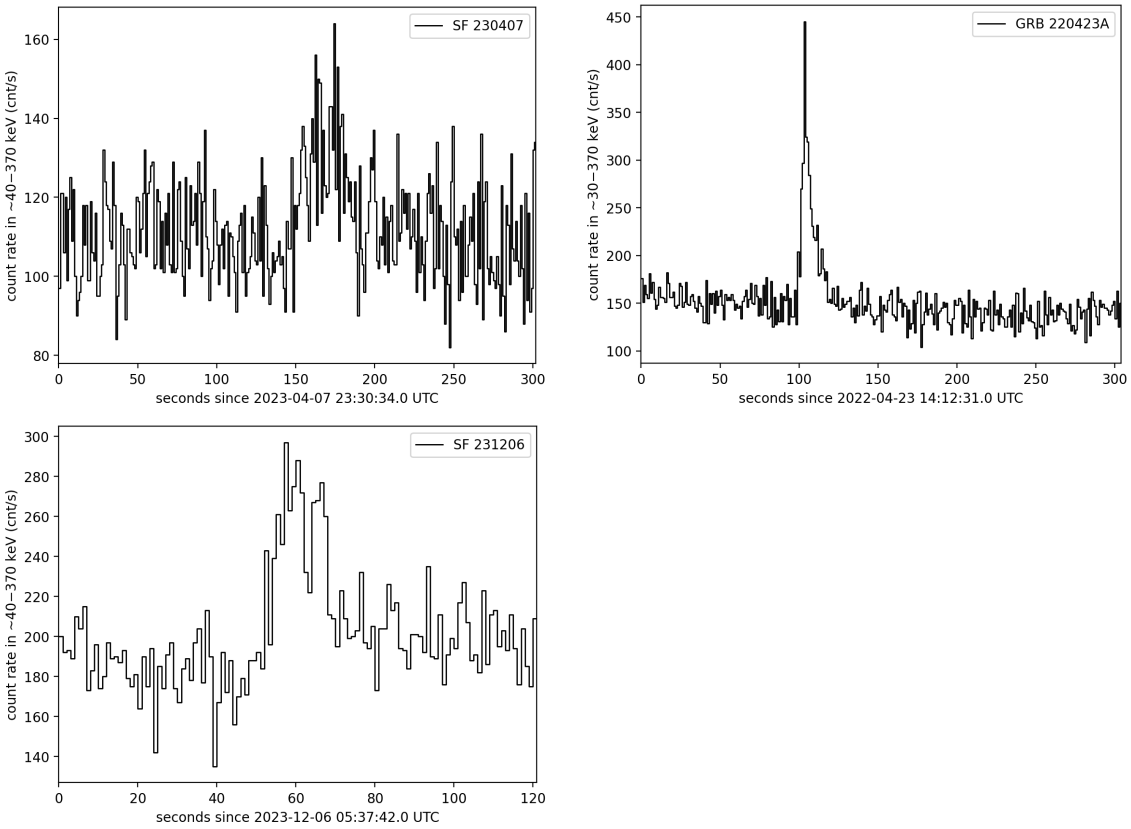

Figure 4.19: Light curves of transients detected by the detector unit 0 on-board VZLUSAT-2.

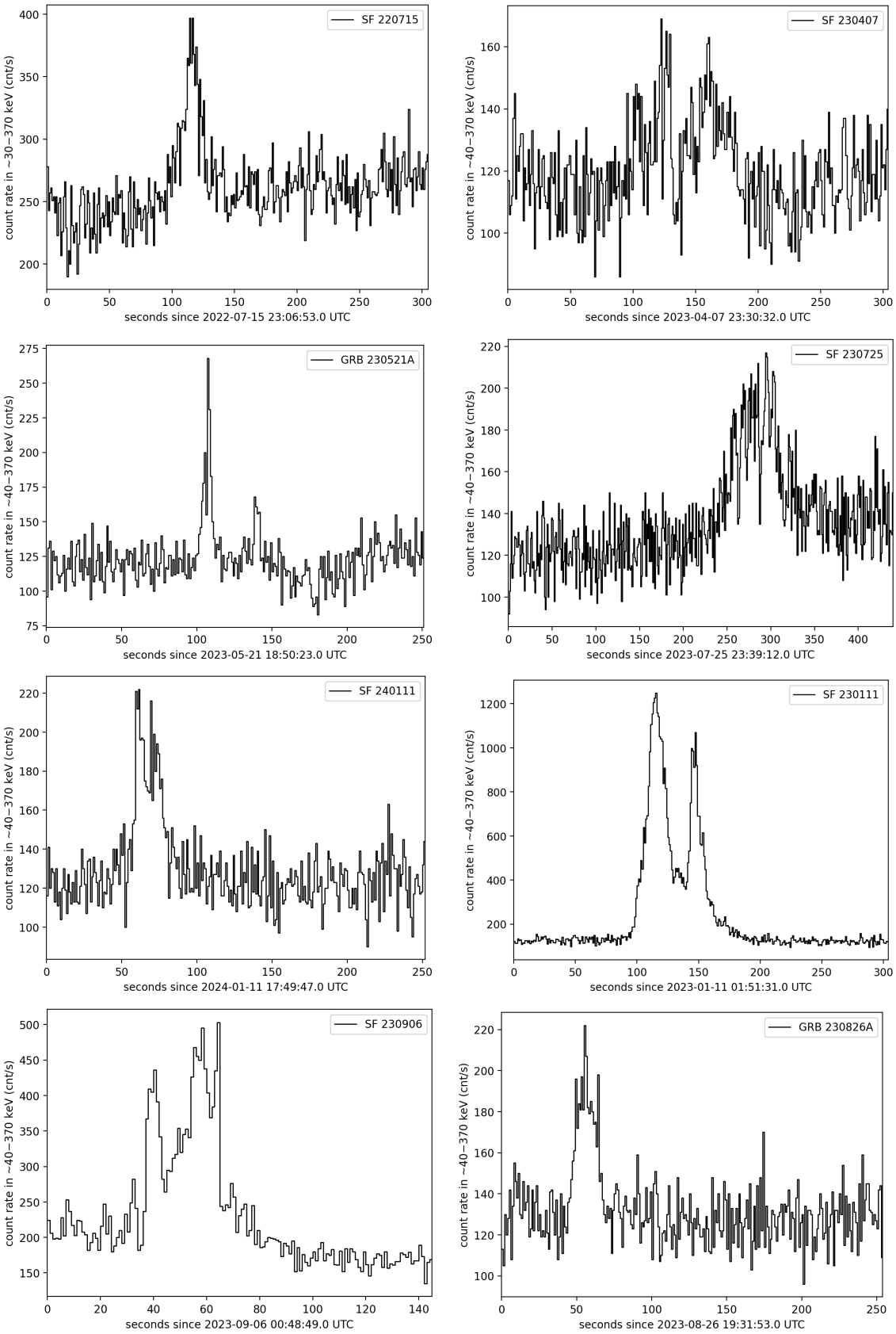

Figure 4.19: Light curves of transients detected by the detector unit 1 on-board VZLUSAT-2.

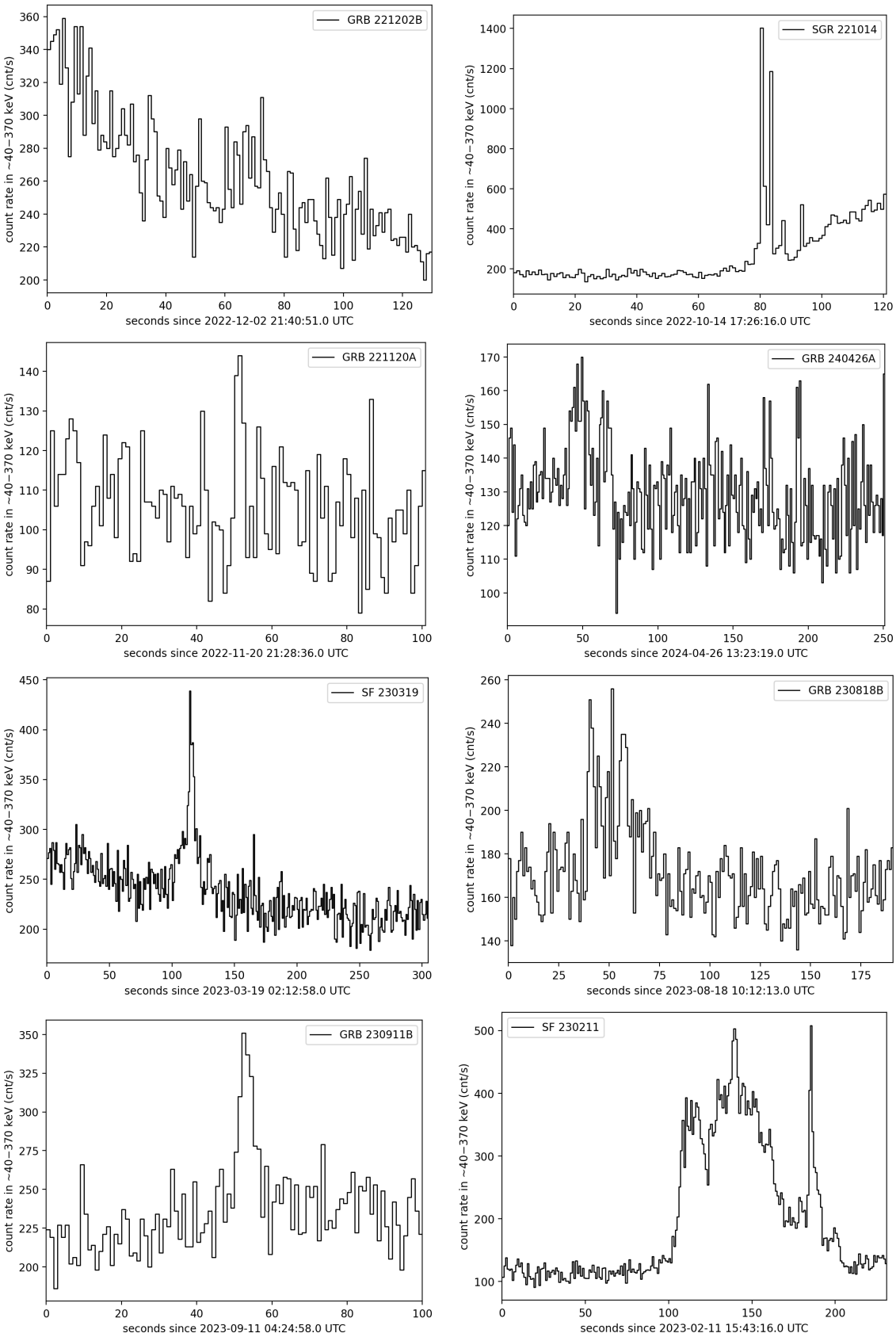

Figure 4.19: Light curves of transients detected by the detector unit 1 on-board VZLUSAT-2.

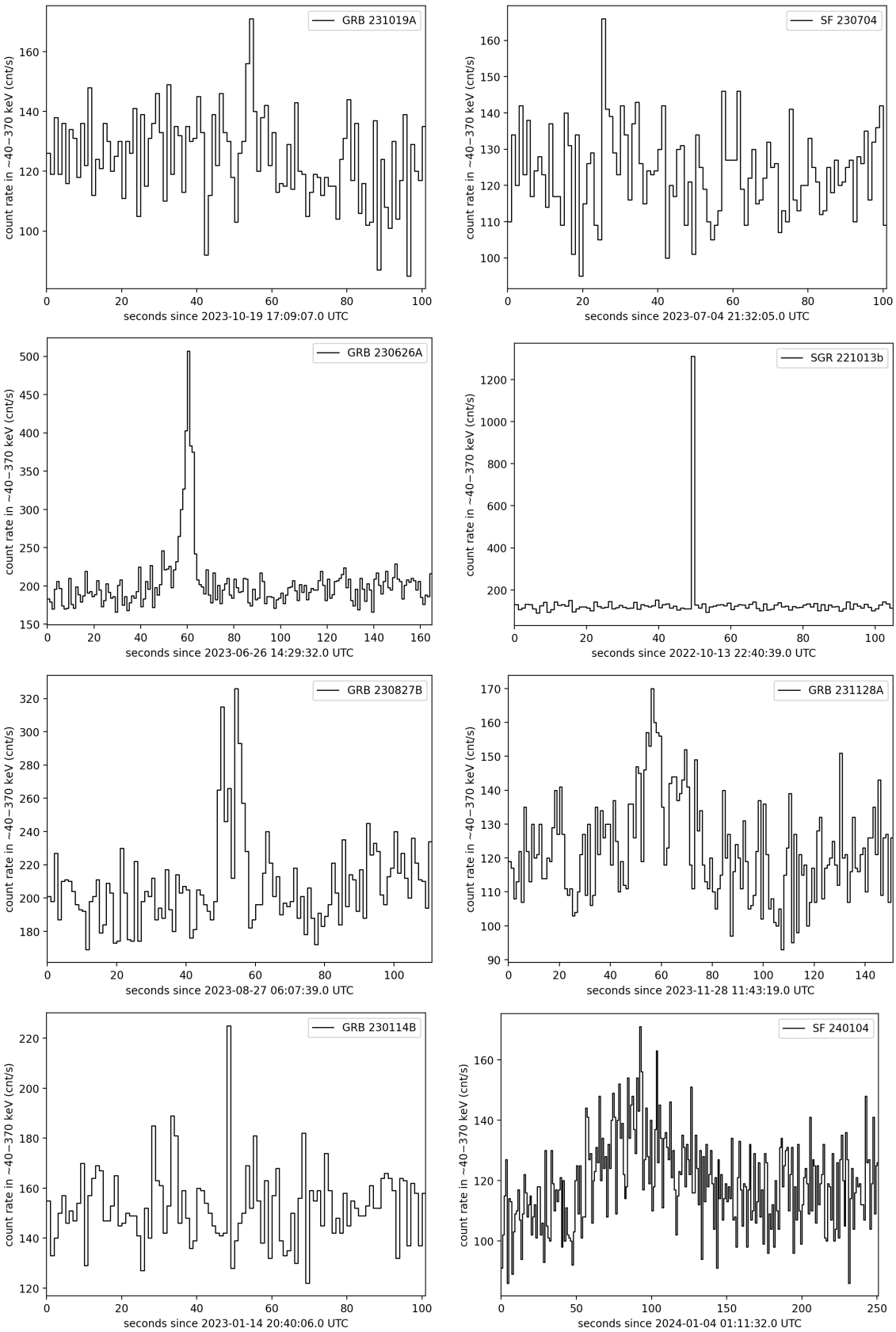

Figure 4.19: Light curves of transients detected by the detector unit 1 on-board VZLUSAT-2.

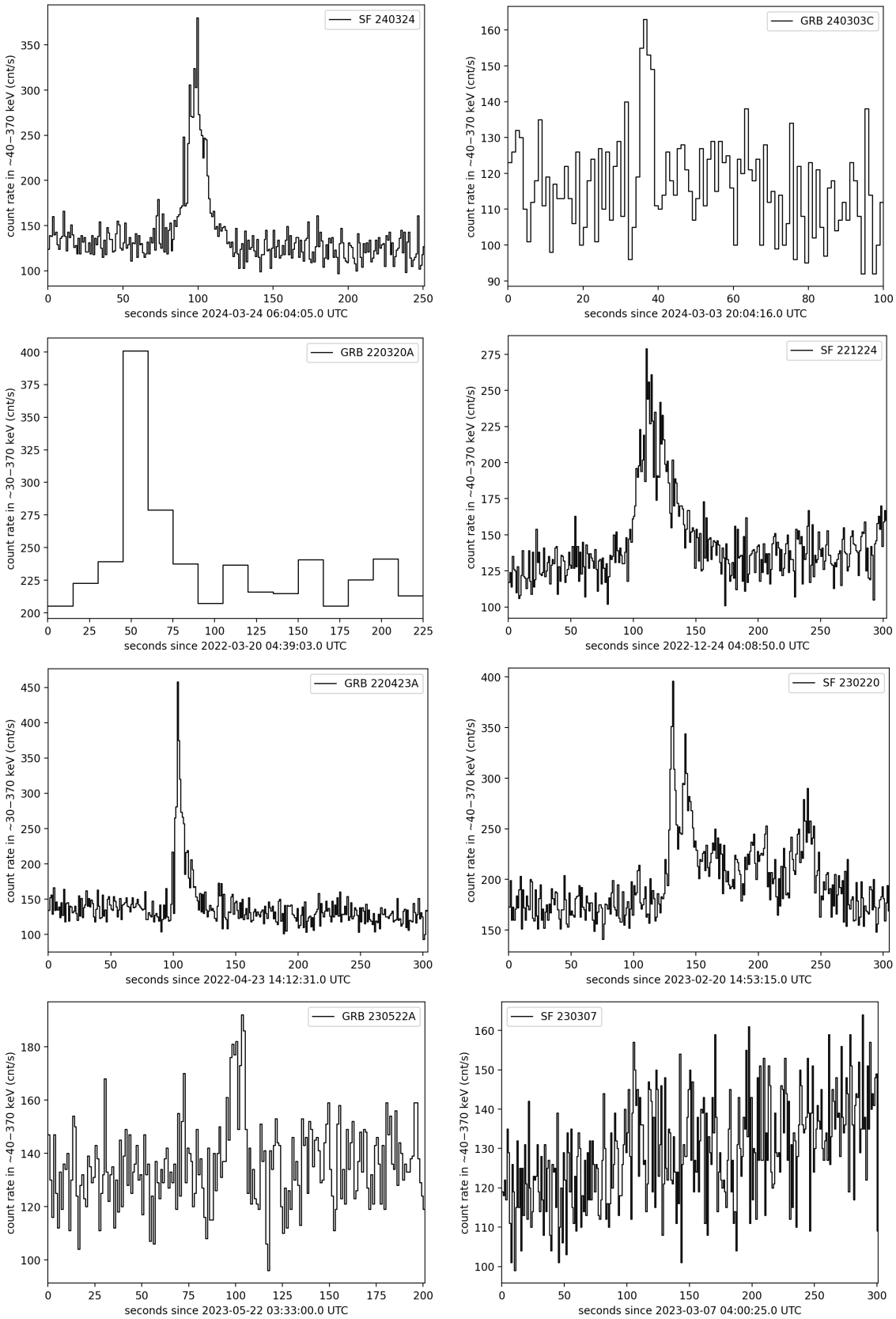

Figure 4.19: Light curves of transients detected by the detector unit 1 on-board VZLUSAT-2.

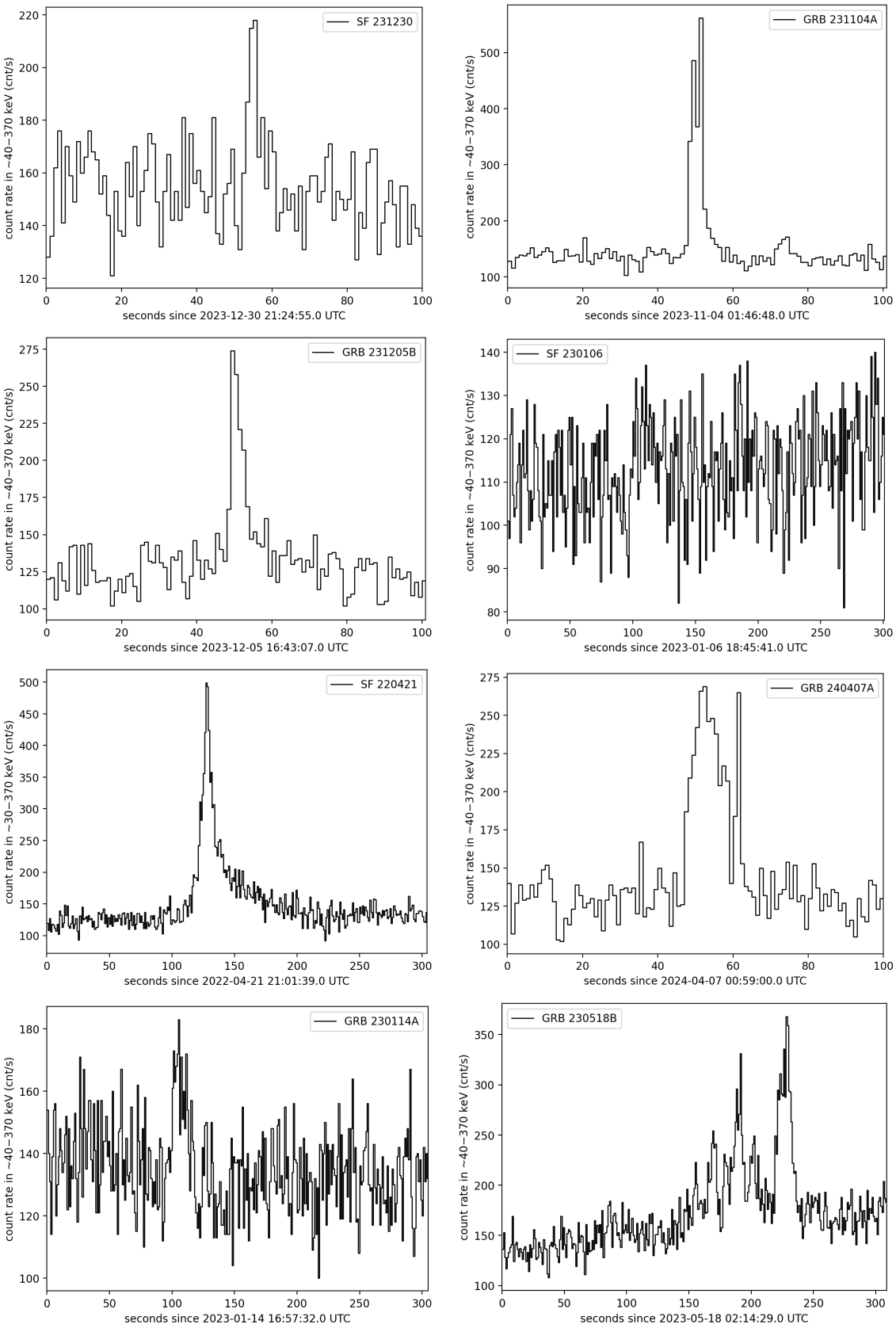

Figure 4.19: Light curves of transients detected by the detector unit 1 on-board VZLUSAT-2.

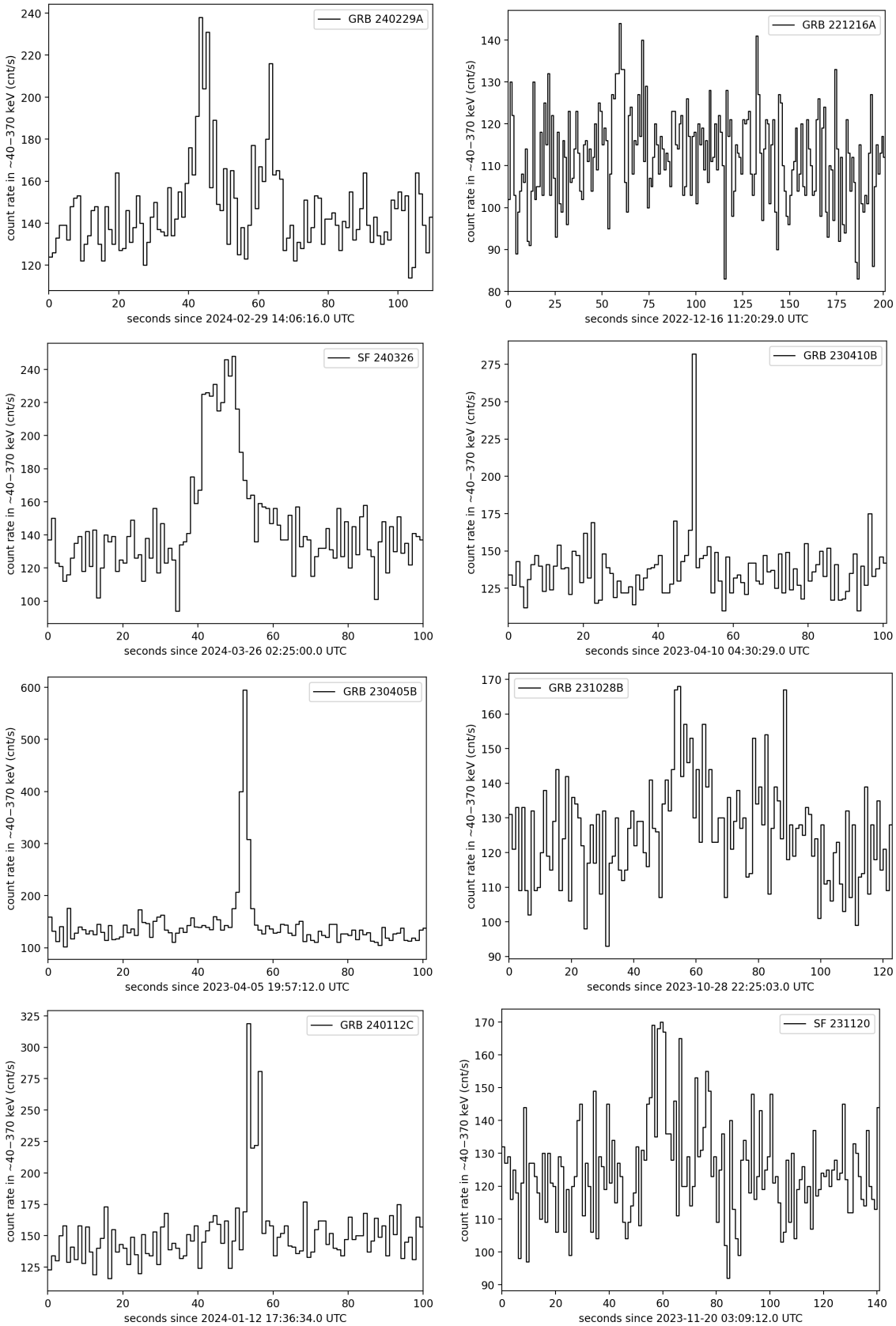

Figure 4.19: Light curves of transients detected by the detector unit 1 on-board VZLUSAT-2.

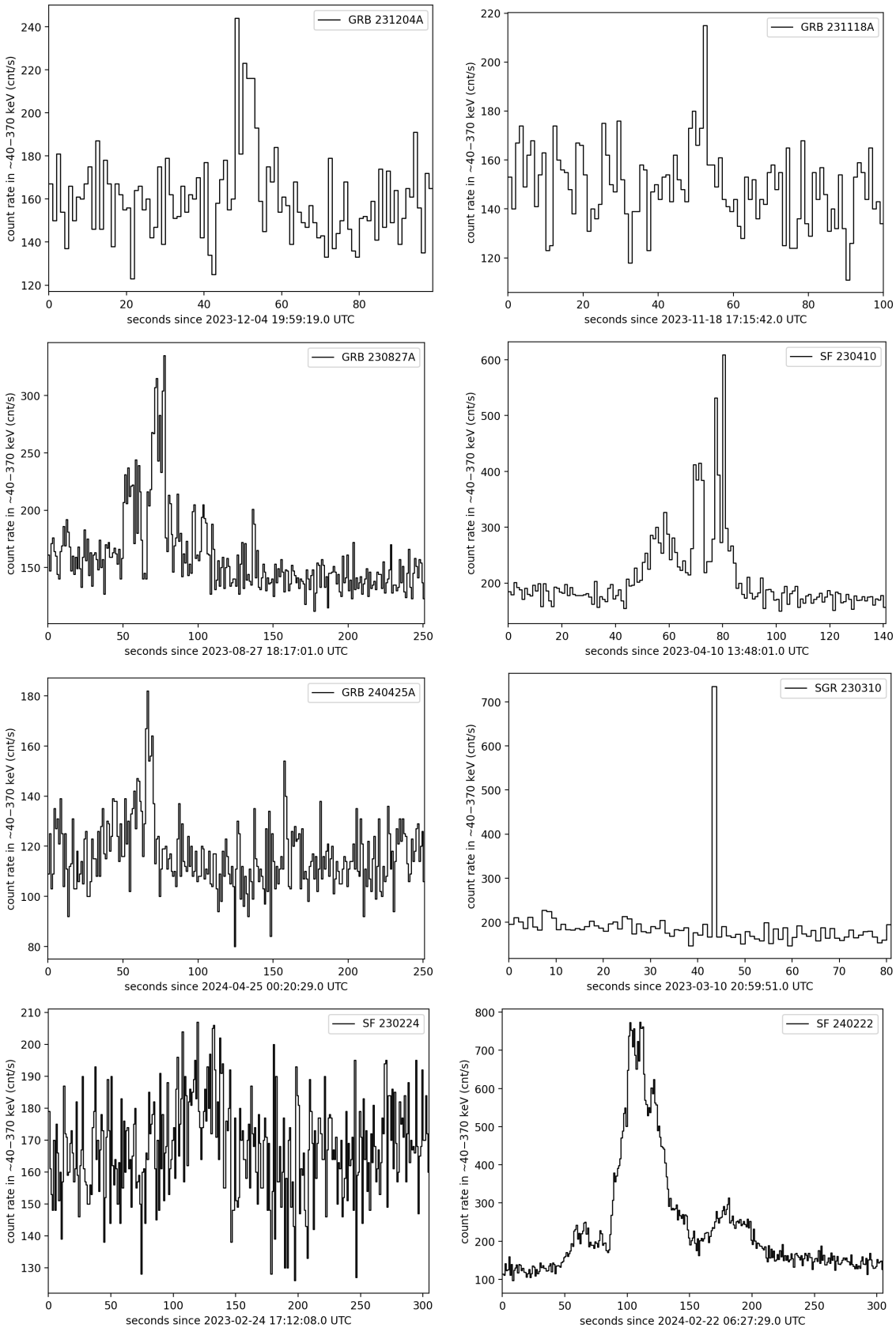

Figure 4.19: Light curves of transients detected by the detector unit 1 on-board VZLUSAT-2.

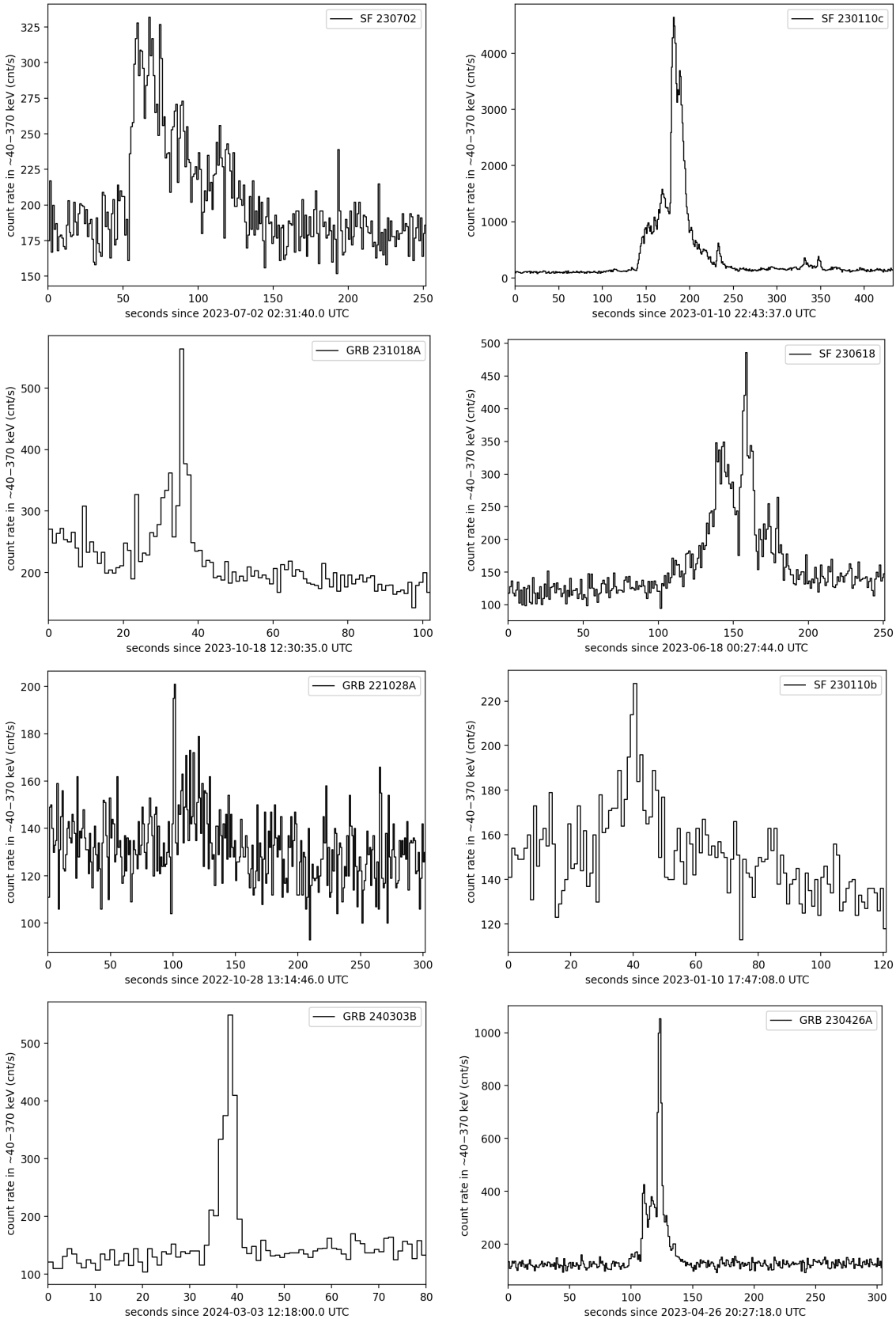

Figure 4.19: Light curves of transients detected by the detector unit 1 on-board VZLUSAT-2.

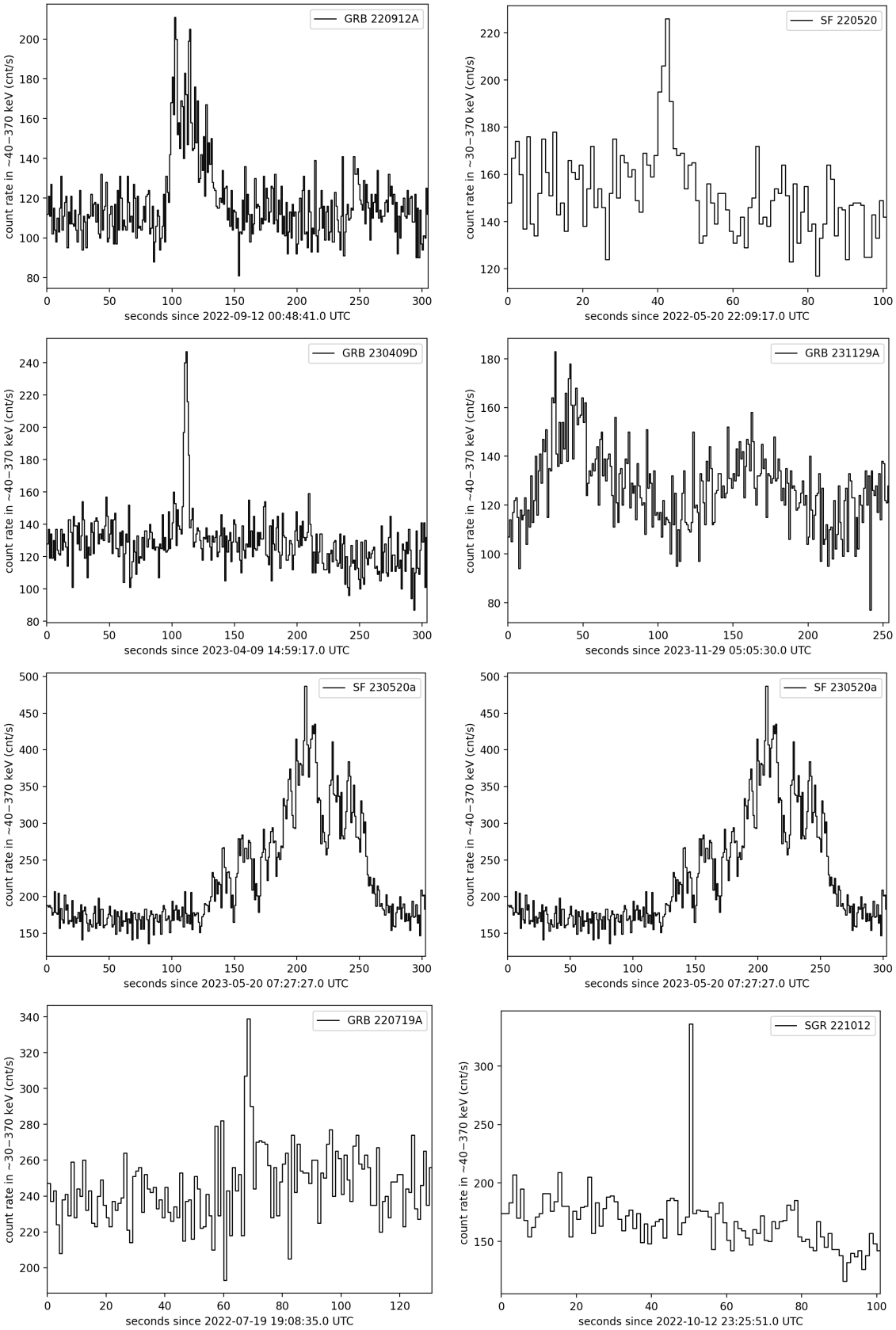

Figure 4.19: Light curves of transients detected by the detector unit 1 on-board VZLUSAT-2.

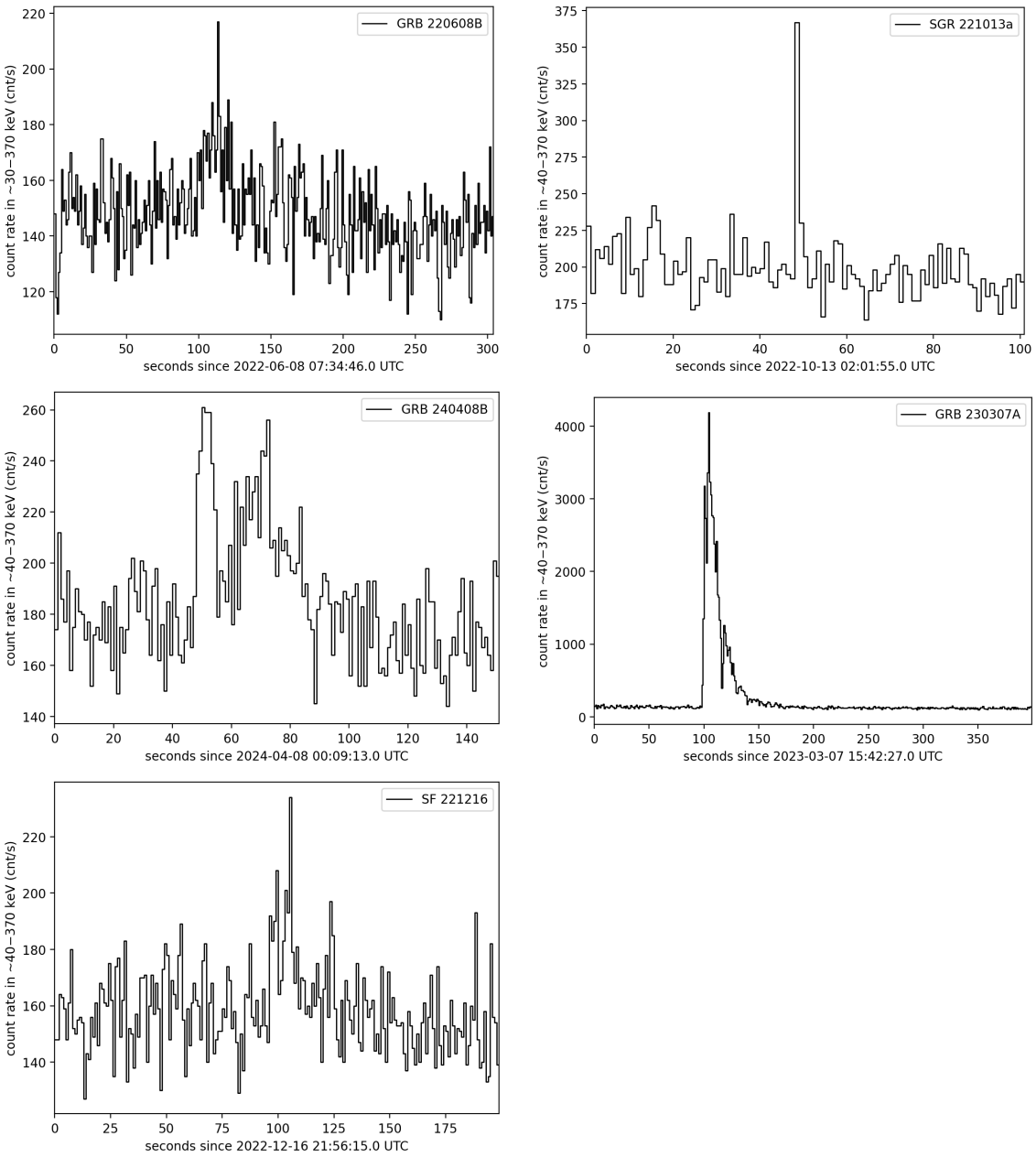

Figure 4.19: Light curves of transients detected by the detector unit 1 on-board VZLUSAT-2.

Appendix B

List of co-authored publications

PÁL, András, Masanori OHNO, László MÉSZÁROS, Norbert WERNER, Jakub ŘÍPA, Balázs CSÁK, **Marianna DAFČÍKOVÁ**, et al. GRBAlpha: The smallest astrophysical space observatory : I. Detector design, system description, and satellite operations. Astronomy & Astrophysics. EDP Sciences, 2023, vol. 677, September, p. 1-9. ISSN 0004-6361. Available from: https://dx.doi.org/10.1051/0004-6361/202346182.

ŘÍPA, Jakub, Hiromitsu TAKAHASHI, Yasushi FUKAZAWA, Norbert WERNER, Filip MÜNZ, András PÁL, Masanori OHNO, **Marianna DAFČÍKOVÁ**, et al. The peak flux of GRB 221009A measured with GRBAlpha. Astronomy & Astrophysics. EDP Sciences, 2023, vol. 677, September, p. 1-7. ISSN 0004-6361. Available from: https://dx.doi.org/10.1051/0004-6361/202346128.

ŘÍPA, Jakub, András PÁL, Masanori OHNO, Norbert WERNER, László MÉSZÁROS, Balázs CSÁK, **Marianna DAFČÍKOVÁ**, et al. Early results from GRBAlpha and VZLUSAT-2. Online. In Jan-Willem A. den Herder, Shouleh Nikzad, Kazuhiro Nakazawa. Proceedings of SPIE, Volume 12181: Space Telescopes and Instrumentation 2022: Ultraviolet to Gamma Ray. Washington: SPIE, 2022, p. 1-11. ISBN 978-1-5106-5343-6. Available from: https://dx.doi.org/10.1117/12.2629332.

List of GCN Circulars (available at https://gcn.nasa.gov/circulars):
32463, 32622, 32624, 32629, 32685, 32696, 32697, 32781, 32794, 32797, 32814, 32815, 32844, 32890, 32904, 32917, 32937, 32953, 32977, 32982, 32991, 33019, 33028, 33088, 33143, 33170, 33218, 33246, 33273, 33303, 33320, 33398, 33417, 33418, 33424, 33473, 33503, 33543, 33590, 33605, 33606, 33702, 33794, 33795, 33811, 33847, 33875, 33905, 33906, 33927, 33984, 34099, 34143, 34200, 34201, 34525, 34572, 34583, 34585, 34586, 34588, 34590, 34647, 34664, 34712, 34850, 34865, 34866, 34922, 34923, 34988, 35008, 35095, 35143, 35151, 35193, 35199, 35224, 35236, 35246, 35248, 35309, 35371, 35372, 35380, 35425, 35459, 35497, 35536, 35544, 35545, 35580, 35628, 35643, 35645, 35649, 35745, 35752, 35753, 35792, 35802, 35827, 35872, 35873, 35894, 35915, 35997, 36035, 36036, 36054, 36062, 36068, 36269, 36350, 36357, 36358, 36363, 36364, 36373, 36374

Bibliography

B. P. Abbott, R. Abbott, T. D. Abbott, F. Acernese, K. Ackley, and C. Adams et al. 2017. Gravitational Waves and Gamma-Rays from a Binary Neutron Star Merger: GW170817 and GRB 170817A. 848, 2, Article L13 (Oct. 2017), L13 pages. https://doi.org/10.3847/2041-8213/aa920c arXiv:1710.05834 [astro-ph.HE]

Alex Abramovici, William E. Althouse, Ronald W. P. Drever, Yekta Gursel, Seiji Kawamura, and Frederick J. Raab et al. 1992. LIGO: The Laser Interferometer Gravitational-Wave Observatory. *Science* 256, 5055 (April 1992), 325–333. https://doi.org/10.1126/science.256.5055.325

F. Acernese, M. Agathos, K. Agatsuma, D. Aisa, N. Allemandou, and A. Allocca et al. 2015. Advanced Virgo: a second-generation interferometric gravitational wave detector. *Classical and Quantum Gravity* 32, 2, Article 024001 (Jan. 2015), 024001 pages. https://doi.org/10.1088/0264-9381/32/2/024001 arXiv:1408.3978 [gr-qc]

Zheng-Hua An, S. Antier, Xing-Zi Bi, Qing-Cui Bu, Ce Cai, and Xue-Lei Cao et al. 2023. Insight-HXMT and GECAM-C observations of the brightest-of-all-time GRB 221009A. *arXiv e-prints*, Article arXiv:2303.01203 (March 2023), arXiv:2303.01203 pages. https://doi.org/10.48550/arXiv.2303.01203 arXiv:2303.01203 [astro-ph.HE]

R. L. Aptekar, D. D. Frederiks, S. V. Golenetskii, V. N. Ilynskii, E. P. Mazets, and V. N. Panov et al. 1995. Konus-W Gamma-Ray Burst Experiment for the GGS Wind Spacecraft. 71, 1-4 (Feb. 1995), 265–272. https://doi.org/10.1007/BF00751332

Yoichi Aso, Yuta Michimura, Kentaro Somiya, Masaki Ando, Osamu Miyakawa, and Takanori Sekiguchi et al. 2013. Interferometer design of the KAGRA gravitational wave detector. 88, 4, Article 043007 (Aug. 2013), 043007 pages. https://doi.org/10.1103/PhysRevD.88.043007 arXiv:1306.6747 [gr-qc]

W. B. Atwood, A. A. Abdo, M. Ackermann, W. Althouse, B. Anderson, and M. Axelsson et al. 2009. The Large Area Telescope on the Fermi Gamma-Ray Space Telescope Mission. 697, 2 (June 2009), 1071–1102. https://doi.org/10.1088/0004-637X/697/2/1071 arXiv:0902.1089 [astro-ph.IM]

S. Barthelmy, L. Barbier, J. Cummings, E. Fenimore, N. Gehrels, and D. Hullinger et al. 2005a. GRB 050509b: Swift-BAT refined analysis of the short hard burst. *GRB Coordinates Network* 3385 (Jan. 2005), 1.

Scott D. Barthelmy, Louis M. Barbier, Jay R. Cummings, Ed E. Fenimore, Neil Gehrels, and Derek Hullinger et al. 2005b. The Burst Alert Telescope (BAT) on the SWIFT Midex Mission. 120, 3-4 (Oct. 2005), 143–164. https://doi.org/10.1007/s11214-005-5096-3 arXiv:astro-ph/0507410 [astro-ph]

V. Bhalerao, D. Bhattacharya, A. Vibhute, P. Pawar, A. R. Rao, and M. K. Hingar et al. 2017. The Cadmium Zinc Telluride Imager on AstroSat. *Journal of Astrophysics and Astronomy* 38, 2, Article 31 (June 2017), 31 pages. https://doi.org/10.1007/s12036-017-9447-8 arXiv:1608.03408 [astro-ph.IM]

J. S. Bloom, S. G. Djorgovski, and S. R. Kulkarni. 2001. The Redshift and the Ordinary Host Galaxy of GRB 970228. 554, 2 (June 2001), 678–683. https://doi.org/10.1086/321398 arXiv:astro-ph/0007244 [astro-ph]

M. Bulla, A. E. Camisasca, C. Guidorzi, L. Amati, A. Rossi, G. Stratta, and P. Singh. 2023. GRB 230307A: good match with kilonova models. *GRB Coordinates Network* 33578 (April 2023), 1.

J. Michael Burgess, Ewan Cameron, Dmitry Svinkin, and Jochen Greiner. 2021. nazgul: A statistical approach to gamma-ray burst localization. Triangulation via non stationary time series models. 654, Article A26 (Oct. 2021), A26 pages. https://doi.org/10.1051/0004-6361/202039461 arXiv:2009.08350 [astro-ph.IM]

David N. Burrows, J. E. Hill, J. A. Nousek, J. A. Kennea, A. Wells, and J. P. Osborne et al. 2005. The Swift X-Ray Telescope. 120, 3-4 (Oct. 2005), 165–195. https://doi.org/10.1007/s11214-005-5097-2 arXiv:astro-ph/0508071 [astro-ph]

G. Cavallo and M. J. Rees. 1978. A qualitative study of cosmic fireballs and gamma -ray bursts. 183 (May 1978), 359–365. https://doi.org/10.1093/mnras/183.3.359

C. C. Cheung, M. Kerr, J. E. Grove, R. Woolf, A. Goldstein, C. A. Wilson-Hodge, and M. S. Briggs. 2023. GRB 231019A: Glowbug gamma-ray detection. *GRB Coordinates Network* 34888 (Oct. 2023), 1.

C. C. Cheung, R. Woolf, M. Kerr, J. E. Grove, A. Goldstein, and C. A. Wilson-Hodge et al. 2024. GRB 240216A: Glowbug gamma-ray detection. *GRB Coordinates Network* 35764 (Feb. 2024), 1.

E. Costa, M. Feroci, F. Frontera, G. Zavattini, L. Nicastro, and E. Palazzi et al. 1997a. GRB 970228. 6572 (March 1997), 1.

E. Costa, F. Frontera, J. Heise, M. Feroci, J. in't Zand, and F. Fiore et al. 1997b. Discovery of an X-ray afterglow associated with the γ-ray burst of 28 February 1997. 387, 6635 (June 1997), 783–785. https://doi.org/10.1038/42885 arXiv:astro-ph/9706065 [astro-ph]

M. Dafcikova, J. Ripa, A. Pal, N. Werner, M. Ohno, and H. Takahashi et al. 2023. GRB 230307A: Detection by GRBAlpha. *GRB Coordinates Network* 33418 (March 2023), 1.

Cui-Yuan Dai, Chen-Lei Guo, Hai-Ming Zhang, Ruo-Yu Liu, and Xiang-Yu Wang. 2024. Evidence for a Compact Stellar Merger Origin for GRB 230307A From Fermi-LAT and Multiwavelength Afterglow Observations. 962, 2, Article L37 (Feb. 2024), L37 pages. https://doi.org/10.3847/2041-8213/ad2680 arXiv:2312.01074 [astro-ph.HE]

V. Dániel, P. Svoboda, M. Junas, M. Sabol, J. CagáÅ, and M. Stejskal et al. 2020. Development of CubeSat with COTS camera enabling EO with high GSD. In *Sensors, Systems, and Next-Generation Satellites XXIV (Society of Photo-Optical Instrumentation Engineers (SPIE) Conference Series, Vol. 11530)*, Steven P. Neeck, Arnaud Hélière, and Toshiyoshi Kimura (Eds.). Article 115300Z, 115300Z pages. https://doi.org/10.1117/12.2575862

Evgeny Derishev and Tsvi Piran. 2024. The contemporaneous phase of GRB afterglows - application to GRB 221009A. 530, 1 (May 2024), 347–359. https://doi.org/10.1093/mnras/stae609 arXiv:2312.01447 [astro-ph.HE]

C. Fletcher and C. Meegan. 2023. GRB 230102A: Fermi GBM Observation. *GRB Coordinates Network* 33151 (Jan. 2023), 1.

L. Fletcher, B. R. Dennis, H. S. Hudson, S. Krucker, K. Phillips, and A. Veronig et al. 2011. An Observational Overview of Solar Flares. 159, 1-4 (Sept. 2011), 19–106. https://doi.org/10.1007/s11214-010-9701-8 arXiv:1109.5932 [astro-ph.SR]

D. A. Frail, S. R. Kulkarni, R. Sari, S. G. Djorgovski, J. S. Bloom, and T. J. Galama et al. 2001. Beaming in Gamma-Ray Bursts: Evidence for a Standard Energy Reservoir. 562, 1 (Nov. 2001), L55–L58. https://doi.org/10.1086/338119 arXiv:astro-ph/0102282 [astro-ph]

Gábor Galgóczi, Jakub Řípa, Riccardo Campana, Norbert Werner, András. Pál, and Masanori Ohno et al. 2021. Simulations of expected signal and background of gamma-ray sources by large field-of-view detectors aboard CubeSats. *Journal of Astronomical Telescopes, Instruments, and Systems* 7, Article 028004 (April 2021), 028004 pages. https://doi.org/10.1117/1.JATIS.7.2.028004 arXiv:2102.08104 [astro-ph.IM]

N. Gehrels, G. Chincarini, P. Giommi, K. O. Mason, J. A. Nousek, and A. A. Wells et al. 2004. The Swift Gamma-Ray Burst Mission. 611, 2 (Aug. 2004), 1005–1020. https://doi.org/10.1086/422091 arXiv:astro-ph/0405233 [astro-ph]

Ramandeep Gill and Jonathan Granot. 2023. GRB 221009A afterglow from a shallow angular structured jet. 524, 1 (Sept. 2023), L78–L83. https://doi.org/10.1093/mnrasl/slad075 arXiv:2304.14331 [astro-ph.HE]

A. Goldstein, P. Veres, E. Burns, M. S. Briggs, R. Hamburg, and D. Kocevski et al. 2017. An Ordinary Short Gamma-Ray Burst with Extraordinary Implications: Fermi-GBM Detection of GRB 170817A. 848, 2, Article L14 (Oct. 2017), L14 pages. https://doi.org/10.3847/2041-8213/aa8f41 arXiv:1710.05446 [astro-ph.HE]

Benjamin P. Gompertz, Maria Edvige Ravasio, Matt Nicholl, Andrew J. Levan, Brian D. Metzger, and Samantha R. Oates et al. 2023. The case for a minute-long merger-driven gamma-ray burst from fast-cooling synchrotron emission. *Nature Astronomy* 7 (Jan. 2023), 67–79. https://doi.org/10.1038/s41550-022-01819-4 arXiv:2205.05008 [astro-ph.HE]

Kevin Hurley. 2011. Soft gamma repeaters. *Advances in Space Research* 47, 8 (April 2011), 1326–1331. https://doi.org/10.1016/j.asr.2010.03.001

Robert Hynes. 2010. Multiwavelength Observations of Accretion in Low-Mass X-ray Binary Systems. *Accretion Processes In Astrophysics: XXI Canary Islands Winter School Of Astrophysics* (10 2010). https://doi.org/10.1017/CBO9781139343268.005

Ray W. Klebesadel, Ian B. Strong, and Roy A. Olson. 1973. Observations of Gamma-Ray Bursts of Cosmic Origin. 182 (June 1973), L85. https://doi.org/10.1086/181225

Glenn F. Knoll. 2000. *Radiation detection and measurement*.

C. Kouveliotou, S. Dieters, T. Strohmayer, J. van Paradijs, G. J. Fishman, and C. A. Meegan et al. 1998. An X-ray pulsar with a superstrong magnetic field in the soft γ-ray repeater SGR1806 - 20. 393, 6682 (May 1998), 235–237. https://doi.org/10.1038/30410

Chryssa Kouveliotou, Charles A. Meegan, Gerald J. Fishman, Narayana P. Bhat, Michael S. Briggs, and Thomas M. Koshut et al. 1993. Identification of Two Classes of Gamma-Ray Bursts. 413 (Aug. 1993), L101. https://doi.org/10.1086/186969

H. A. Krimm, S. D. Barthelmy, P. D'Avanzo, S. Laha, A. Y. Lien, and C. B. Markwardt et al. 2024. GRB 240222A: Swift-BAT refined analysis. *GRB Coordinates Network* 35781 (Feb. 2024), 1.

A. J. Levan. 2015. Swift discoveries of new populations of extremely long duration high energy transient. *Journal of High Energy Astrophysics* 7 (Sept. 2015), 44–55. https://doi.org/10.1016/j.jheap.2015.05.004 arXiv:1506.03960 [astro-ph.HE]

A. J. Levan, B. P. Gompertz, D. B. Malesani, N. R. Tanvir, E. Burns, and R. Salvaterra et al. 2023. GRB 230307A: JWST observations consistent with the presence of a kilonova. *GRB Coordinates Network* 33569 (April 2023), 1.

Yanguo Li, Xiangyang Wen, Xilei Sun, Xiaojing Liu, Xiaohua Liang, and Dongya Guo et al. 2020. The GECAM and its payload. *Scientia Sinica Physica, Mechanica & Astronomica* 50, 12 (Jan. 2020), 129508. https://doi.org/10.1360/SSPMA-2019-0417

Masaru Matsuoka, Kazuyoshi Kawasaki, Shiro Ueno, Hiroshi Tomida, Mitsuhiro Kohama, and Motoko Suzuki et al. 2009. The MAXI Mission on the ISS: Science and Instruments for Monitoring All-Sky X-Ray Images. 61 (Oct. 2009), 999. https://doi.org/10.1093/pasj/61.5.999 arXiv:0906.0631 [astro-ph.IM]

Charles Meegan, Giselher Lichti, P. N. Bhat, Elisabetta Bissaldi, Michael S. Briggs, and Valerie Connaughton et al. 2009. The Fermi Gamma-ray Burst Monitor. 702, 1 (Sept. 2009), 791–804. https://doi.org/10.1088/0004-637X/702/1/791 arXiv:0908.0450 [astro-ph.IM]

Sandro Mereghetti. 2008. The strongest cosmic magnets: soft gamma-ray repeaters and anomalous X-ray pulsars. 15, 4 (July 2008), 225–287. https://doi.org/10.1007/s00159-008-0011-z arXiv:0804.0250 [astro-ph]

P. Mészáros. 2006. Gamma-ray bursts. *Reports on Progress in Physics* 69, 8 (Aug. 2006), 2259–2321. https://doi.org/10.1088/0034-4885/69/8/R01 arXiv:astro-ph/0605208 [astro-ph]

Ignacio Negueruela. 1998. On the nature of Be/X-ray binaries. 338 (Oct. 1998), 505–510. https://doi.org/10.48550/arXiv.astro-ph/9807158 arXiv:astro-ph/9807158 [astro-ph]

Masanori Ohno. 2022. Basic of the radiation detector and application for the GRBAlpha. (2022). Masaryk University, Brno.

Masanori Ohno, Norbert Werner, András. Pál, Jakub Řípa, Gabór Galgóczi, and Norbert Tarcai et al. 2018. CAMELOT: design and performance verification of the detector concept and localization capability. In *Space Telescopes and Instrumentation 2018: Ultraviolet to Gamma Ray (Society of Photo-Optical Instrumentation Engineers (SPIE) Conference Series, Vol. 10699)*, Jan-Willem A. den Herder, Shouleh Nikzad, and Kazuhiro Nakazawa (Eds.). Article 1069964, 1069964 pages. https://doi.org/10.1117/12.2313228 arXiv:1806.03686 [astro-ph.IM]

S. A. Olausen and V. M. Kaspi. 2014. The McGill Magnetar Catalog. 212, 1, Article 6 (May 2014), 6 pages. https://doi.org/10.1088/0067-0049/212/1/6 arXiv:1309.4167 [astro-ph.HE]

András. Pál, Masanori Ohno, László Mészáros, Norbert Werner, Jakub Ripa, and Marcel Frajt et al. 2020. GRBAlpha: a 1U CubeSat mission for validating timing-based gamma-ray burst localization. In *Society of Photo-Optical Instrumentation Engineers (SPIE) Conference Series (Society of Photo-Optical Instrumentation Engineers (SPIE) Conference Series, Vol. 11444)*. Article 114444V, 114444V pages. https://doi.org/10.1117/12.2561351 arXiv:2012.01298 [astro-ph.IM]

András Pál, Masanori Ohno, László Mészáros, Norbert Werner, Jakub Řípa, and Balázs Csák et al. 2023. GRBAlpha: the smallest astrophysical space observatory – Part 1: Detector design, system description and satellite operations. *arXiv e-prints*, Article arXiv:2302.10048 (Feb. 2023), arXiv:2302.10048 pages. https://doi.org/10.48550/arXiv.2302.10048 arXiv:2302.10048 [astro-ph.IM]

T. Piran. 1999. Gamma-ray bursts and the fireball model. 314, 6 (June 1999), 575–667. https://doi.org/10.1016/S0370-1573(98)00127-6 arXiv:astro-ph/9810256 [astro-ph]

Tsvi Piran. 2004. The physics of gamma-ray bursts. *Reviews of Modern Physics* 76, 4 (Oct. 2004), 1143–1210. https://doi.org/10.1103/RevModPhys.76.1143 arXiv:astro-ph/0405503 [astro-ph]

S. Poolakkil, R. Preece, C. Fletcher, A. Goldstein, P. N. Bhat, and E. Bissaldi et al. 2021. The Fermi-GBM Gamma-Ray Burst Spectral Catalog: 10 yr of Data. 913, 1, Article 60 (May 2021), 60 pages. https://doi.org/10.3847/1538-4357/abf24d arXiv:2103.13528 [astro-ph.HE]

Tuija Pulkkinen. 2007. Space Weather: Terrestrial Perspective. *Living Reviews in Solar Physics* 4, 1, Article 1 (May 2007). https://doi.org/10.12942/lrsp-2007-1

Pablo Reig. 2011. Be/X-ray binaries. 332, 1 (March 2011), 1–29. https://doi.org/10.1007/s10509-010-0575-8 arXiv:1101.5036 [astro-ph.HE]

J. Ripa, A. Pal, N. Werner, M. Ohno, H. Takahashi, and L. Meszaros et al. 2022. GRB 221009A: Detection by GRBAlpha. *GRB Coordinates Network* 32685 (Oct. 2022), 1.

Peter W. A. Roming, Thomas E. Kennedy, Keith O. Mason, John A. Nousek, Lindy Ahr, and Richard E. Bingham et al. 2005. The Swift Ultra-Violet/Optical Telescope. 120, 3-4 (Oct. 2005), 95–142. https://doi.org/10.1007/s11214-005-5095-4 arXiv:astro-ph/0507413 [astro-ph]

Kailash C. Sahu, Mario Livio, Larry Petro, F. Duccio Macchetto, Jan van Paradijs, and Chryssa Kouveliotou et al. 1997. The optical counterpart to γ-ray burst GRB970228 observed using the Hubble Space Telescope. 387, 6632 (May 1997), 476–478. https://doi.org/10.1038/387476a0 arXiv:astro-ph/9705184 [astro-ph]

Kulinder Pal Singh, S. N. Tandon, P. C. Agrawal, H. M. Antia, R. K. Manchanda, and J. S. Yadav et al. 2014. ASTROSAT mission. In *Space Telescopes and Instrumentation 2014: Ultraviolet to Gamma Ray (Society of Photo-Optical Instrumentation Engineers (SPIE) Conference Series, Vol. 9144)*, Tadayuki Takahashi, Jan-Willem A. den Herder, and Mark Bautz (Eds.). Article 91441S, 91441S pages. https://doi.org/10.1117/12.2062667

K. Z. Stanek, T. Matheson, P. M. Garnavich, P. Martini, P. Berlind, and N. Caldwell et al. 2003. Spectroscopic Discovery of the Supernova 2003dh Associated with GRB 030329. 591, 1 (July 2003), L17–L20. https://doi.org/10.1086/376976 arXiv:astro-ph/0304173 [astro-ph]

M. Tavani, A. Addis, A. Argan, L. A. Antonelli, N. Auricchio, and G. Barbiellini et al. 2024. The AGILE satellite ceased operations and re-entered today into the atmosphere. *GRB Coordinates Network* 35726 (Feb. 2024), 1.

M. Tavani, G. Barbiellini, A. Argan, F. Boffelli, A. Bulgarelli, and P. Caraveo et al. 2009. The AGILE Mission. 502, 3 (Aug. 2009), 995–1013. https://doi.org/10.1051/0004-6361/200810527 arXiv:0807.4254 [astro-ph]

C. C. Thoene, A. de Ugarte Postigo, J. F. Agui Fernandez, L. Izzo, J. P. U. Fynbo, and N. R. Tanvir et al. 2023. GRB 231215A: Redshift from OSIRIS+ / GTC. *GRB Coordinates Network* 35373 (Dec. 2023), 1.

Aaron Tohuvavohu, Jamie A. Kennea, James DeLaunay, David M. Palmer, S. Bradley Cenko, and Scott Barthelmy. 2020. Gamma-Ray Urgent Archiver for Novel Opportunities (GUANO): Swift/BAT Event Data Dumps on Demand to Enable Sensitive Subthreshold GRB Searches. 900, 1, Article 35 (Sept. 2020), 35 pages. https://doi.org/10.3847/1538-4357/aba94f arXiv:2005.01751 [astro-ph.HE]

Kento Torigoe, Yasushi Fukazawa, Gabór Galgóczi, Tsunefumi Mizuno, Kazuhiro Nakazawa, and Masanori Ohno et al. 2019. Performance study of a large CsI(Tl) scintillator with an MPPC readout for nanosatellites used to localize gamma-ray bursts. *Nuclear Instruments and Methods in Physics Research A* 924 (April 2019), 316–320. https://doi.org/10.1016/j.nima.2018.08.039

Shoji Torii, Pier Simone Marrocchesi, and Calet Collaboration. 2019. The CALorimetric Electron Telescope (CALET) on the International Space Station. *Advances in Space Research* 64, 12 (Dec. 2019), 2531–2537. https://doi.org/10.1016/j.asr.2019.04.013

E. Troja, C. L. Fryer, B. O'Connor, G. Ryan, S. Dichiara, and A. Kumar et al. 2022. A nearby long gamma-ray burst from a merger of compact objects. 612, 7939 (Dec. 2022), 228–231. https://doi.org/10.1038/s41586-022-05327-3 arXiv:2209.03363 [astro-ph.HE]

A. Ursi, N. Parmiggiani, M. Messerotti, A. Pellizzoni, C. Pittori, and F. Longo et al. 2023. The First AGILE Solar Flare Catalog. 267, 1, Article 9 (July 2023), 9 pages. https://doi.org/10.3847/1538-4365/acd4b6 arXiv:2305.14957 [astro-ph.SR]

J. D. Valentine, W. W. Moses, S. E. Derenzo, D. K. Wehe, and G. F. Knoll. 1993. Temperature Dependence of CsI(Tl) Gamma-ray Excited Scintillation Characteristics. *Nuclear Instruments and Methods in Physics Research* A325 (1993), 147–157.

J. van Paradijs, P. J. Groot, T. Galama, C. Kouveliotou, R. G. Strom, and J. Telting et al. 1997. Transient optical emission from the error box of the γ-ray burst of 28 February 1997. 386, 6626 (April 1997), 686–689. https://doi.org/10.1038/386686a0

Jakub Řípa, Hiromitsu Takahashi, Yasushi Fukazawa, Norbert Werner, Filip Münz, and András Pál et al. 2023. The peak flux of GRB 221009A measured with GRBAlpha. 677, Article L2 (Sept. 2023), L2 pages. https://doi.org/10.1051/0004-6361/202346128 arXiv:2302.10047 [astro-ph.HE]

Norbert Werner, Jakub Řípa, András Pál, Masanori Ohno, Norbert Tarcai, and Kento Torigoe et al. 2018. CAMELOT: Cubesats Applied for MEasuring and LOcalising Transients mission overview. In *Space Telescopes and Instrumentation 2018: Ultraviolet to Gamma Ray (Society of Photo-Optical Instrumentation Engineers (SPIE) Conference Series, Vol. 10699)*, Jan-Willem A. den Herder, Shouleh Nikzad, and Kazuhiro

Nakazawa (Eds.). Article 106992P, 106992P pages. https://doi.org/10.1117/12.2313764 arXiv:1806.03681 [astro-ph.IM]

C. Winkler, T. J. L. Courvoisier, G. Di Cocco, N. Gehrels, A. Giménez, and S. Grebenev et al. 2003. The INTEGRAL mission. 411 (Nov. 2003), L1–L6. https://doi.org/10.1051/0004-6361:20031288

Kazutaka Yamaoka, Atsumasa Yoshida, Takanori Sakamoto, Ichiro Takahashi, Takumi Hara, and Tatsuma Yamamoto et al. 2013. CALET Gamma-ray Burst Monitor (CGBM). In *International Cosmic Ray Conference (International Cosmic Ray Conference, Vol. 33)*. 2948. https://doi.org/10.48550/arXiv.1311.4084 arXiv:1311.4084 [astro-ph.IM]

Bing Zhang, Xiang-Yu Wang, and Jian-He Zheng. 2024. The BOAT GRB 221009A: A Poynting-flux-dominated narrow jet surrounded by a matter-dominated structured jet wing. *Journal of High Energy Astrophysics* 41 (March 2024), 42–53. https://doi.org/10.1016/j.jheap.2024.01.002 arXiv:2311.14180 [astro-ph.HE]

Jin-Ping Zhu, Xiangyu Ivy Wang, Hui Sun, Yuan-Pei Yang, Zhuo Li, and Rui-Chong Hu et al. 2022. Long-duration Gamma-Ray Burst and Associated Kilonova Emission from Fast-spinning Black Hole-Neutron Star Mergers. 936, 1, Article L10 (Sept. 2022), L10 pages. https://doi.org/10.3847/2041-8213/ac85ad arXiv:2207.10470 [astro-ph.HE]